

UNIVERSITY OF OKLAHOMA  
GRADUATE COLLEGE

SPECTRAL ANALYSES OF THE DUAL POLARIZATION  
DOPPLER WEATHER RADAR DATA

A DISSERTATION  
SUBMITTED TO THE GRADUATE FACULTY  
in partial fulfillment of the requirements for the  
degree of  
Doctor of Philosophy

By  
SVETLANA MONAKHOVA BACHMANN  
Norman, Oklahoma  
2007

SPECTRAL ANALYSES OF THE DUAL POLARIZATION  
DOPPLER WEATHER RADAR DATA

A DISSERTATION APPROVED FOR THE  
DEPARTMENT OF ENGINEERING

BY



Dr. Victor DeBrunner



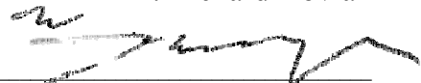
Dr. Tim-You Yu



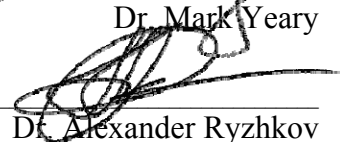
Dr. Dusan Zrnić



Dr. Richard Doviak



Dr. Mark Yeary



Dr. Alexander Ryzhkov



Dr. Michael Biggerstaff



## **Acknowledgments**

The funding for this work was provided by the Office of Oceanic and Atmospheric Research under NOAA – University of Oklahoma Cooperative Agreement #NA17RJ1227, U.S. Department of Commerce. I am grateful to the administration and staff of Cooperative Institute for Mesoscale Meteorological Studies of The University of Oklahoma, and OAR National Severe Storm Laboratory for providing remarkable research environment and opportunities. I acknowledge my committee chairs Victor DeBrunner and Tian-You Yu, and committee members Dusan Zrnić, Richard Doviak, Mark Yeary, Alexander Ryzhkov and Michael Biggerstaff for advising. Especially I recognize Dusan Zrnić for guidance and invaluable suggestions for this work.

I acknowledge my colleagues from the National Severe Storm Laboratory. Allen Zahrai led the engineering team that performed modifications on the research WDR-88D radar to allow versatile control. Mike Schmidt and Richard Wahkinney maintained the radar and Sebastian Torres, Igor Ivic, and Chris Curtis contributed to the time-series collection capability on the KOUN radar. Part of this work was supported by the National Weather Service, the Federal Aviation Administration, and the Air Force Weather Service through the NEXRAD Product Improvement Program. I also acknowledge my daughter Kristina Monakhova for her patience and help in my work on the degree and the dissertation.

## Table of Contents

<b>1. Introduction.....</b>	<b>1</b>
1.1. Scope of dissertation.....	10
1.2. Problems .....	11
1.3. Proposed Solutions .....	11
<b>2. Background .....</b>	<b>14</b>
2.1. Doppler weather radar.....	14
2.2. Time-series data.....	16
2.3. Dual polarization Doppler radar .....	18
2.4. Moments and Polarimetric Variables.....	18
2.4.1. Signal Power and Reflectivity Estimation .....	20
2.4.2. Doppler Velocity Estimation .....	20
2.4.3. Differential Reflectivity .....	21
2.4.4. Differential Phase shift .....	22
2.4.5. Copolar correlation coefficient .....	23
2.5. Ground Clutter .....	23
2.6. Parametric Spectral Processing.....	24
<b>3. Literature Survey.....</b>	<b>27</b>
3.1. Precipitation-free radar observation.....	27
3.2. Attempts to improve wind velocity estimates.....	28
3.3. Radar observation of bird migration.....	31
3.4. Polarimetric radar observation.....	33
3.5. Variety of Nocturnal Migrants in the Great Plains .....	35
3.5.1. Birds.....	35
3.5.2. Insects .....	40
<b>4. Data analyses .....</b>	<b>44</b>
4.1. Radar set up.....	44
4.2. Data collection .....	45
4.3. Weather conditions .....	46
4.4. Data analyses from PPI.....	48
<b>5. Spectral Analyses .....</b>	<b>53</b>
5.1. Spectral Processing.....	53
5.2. Low Signal to Noise Ratio.....	55
5.3. Spectral Field .....	57
5.4. Spectral peak power to noise level ratio .....	58
5.5. Dual Polarization Spectral Field .....	59
5.6. Choice of spectral coefficients.....	60
<b>6. Spectral Polarimetric Analyses.....</b>	<b>63</b>
6.1. Spectral densities of polarimetric variables .....	63
6.2. Example of the spectral densities of polarimetric variables .....	66
6.3. Two-dimensional histogram .....	68
6.4. Spectral VAD.....	70

6.5.	Number of ranges to average for the SVAD.....	71
6.6.	VAD from SVAD .....	73
6.7.	Speculations about censoring with $\rho_{hv}$ .....	75
6.8.	Preferable parameters for scatterer discrimination .....	76
<b>7.</b>	<b>Intrinsic polarimetric values of biological scatterers .....</b>	<b>78</b>
7.1.	Polarimetric spectral densities in one radial .....	79
7.2.	Histograms of spectral densities .....	82
7.3.	Histograms in discrete radials.....	83
7.4.	Velocity Azimuth Polarimetry Display .....	85
7.4.1.	2D histogram of $\delta SD$ for a sector in range and azimuth.....	85
7.4.2.	3D histogram of $\delta SD$ .....	86
7.5.	Example of 3DASH for evaluation of contributing scatterers.....	88
7.5.1.	Clear Air Traced by Passive Insects .....	89
7.5.2.	Precipitation-free Air filled with Ascending Birds and Insects .....	89
7.5.3.	Insects in Precipitation-free Air and at Night .....	90
7.5.4.	Summed up 3DASH .....	92
7.6.	Insects' intrinsic polarimetric values .....	94
7.7.	Conclusion .....	96
<b>8.</b>	<b>Parametric spectral estimation techniques.....</b>	<b>98</b>
8.1.	Composite spectrum – speculations.....	98
8.2.	Examples of spectra estimated using different methods.....	99
8.3.	Processing technique.....	101
<b>9.</b>	<b>Conclusion .....</b>	<b>103</b>
	<b>References.....</b>	<b>107</b>
	<b>Appendices</b>	
	Appendix A. Differential reflectivity calibration	
	Appendix B. System phase computation	
	Appendix C. Cross spectrum density vs. copolar correlation spectral density	
	Appendix D. Change in PPIs over time	
	Appendix E. Changes in PPI over time (zoomed)	
	Appendix F. List of Abbreviations	

## **Abstract**

Echoes in clear air from biological scatterers mixed within the resolution volumes over a large region are presented. These echoes were observed with the polarimetric prototype of the forthcoming WSR-88D weather radar. The study case occurred in the evening of September 7, 2004, at the beginning of the bird migrating season. Novel polarimetric spectral analyses are used for distinguishing signatures of birds and insects in multimodal spectra. These biological scatterers were present at the same time in the radar resolution volumes over a large area. Spectral techniques for (1) data censoring, (2) wind retrieval and (3) estimation of intrinsic values/functions of polarimetric variables for different types of scatterers are presented. The technique for data censoring in the frequency domain allows detection of weak signals. Censoring is performed on the level of spectral densities, allowing exposure of contributions to the spectrum from multiple types of scatterers. The spectral techniques for wind retrieval allow simultaneous estimation of wind from the data that are severely contaminated by migrating birds, and assessment of bird migration parameters. The intrinsic polarimetric signatures associated with the variety of scatterers can be evaluated using presented methodology. Algorithms for echo classification can be built on these. The possibilities of spectral processing using parametric estimation techniques are explored for resolving contributions to the Doppler spectrum from the three types of scatterers: passive wind tracers, actively flying insects and birds. A combination of parametric and non-parametric polarimetric spectral analyses is used to estimate the small bias introduced to the wind velocity by actively flying insects.

## 1. Introduction

The lowest part of the troposphere, where the earth's surface has a great influence on the atmosphere is called the planetary boundary layer (PBL). The weather radar scans the PBL by sending bursts of energy concentrated in a narrow beam and detecting the returns. Often the backscattered signal is a composite of the weather signal and other unwanted clutter signals originating in the scanned portion of the PBL. The weather signals are the echoes from precipitation and *clear air*. *Clear air* refers to the condition in which the atmosphere is free of clouds and precipitation, and is generally assumed to be caused by echoes from the refractive index perturbations. The *precipitation-free air* refers to atmosphere with insects and other objects or substances that might trace or enhance the echoes from clear air.

In weather radar applications, all signals except the weather echoes are considered to be unwanted clutter. There are many types of clutter caused by reflections from ground and airborne objects. Reflections from terrain and surface structures such as buildings and towers are examples of ground clutter. Many signal processing approaches have been developed to successfully suppress ground clutter contamination (Skolnik 1987, Sirmans 1992; Doviak and Zrnić 1993; Accu-Weather 1995; Torres and Zrnić 1999); exceptions are cases where the clutter exceeds the weather signal, saturates the receiver, and cases with non-stationary ground clutter from wind turbines (Butler and Johnson 2003) or road traffic. Examples of airborne clutter are passive or active displacement of birds and airborne insects, airplanes, balloons, and helicopters, and interference from radio frequency (RF) equipment or

the sun. Clutter alters the signal with weather in many ways, from introducing small biases in estimated parameters to completely destroying constructive components of the signal. Clutter refers to the echoes from unwanted objects. Airborne objects introduce errors in the wind velocity measurements. Meteorologists have to use independent information to validate the radar data and often discard portions of these data as unreliable.

Engineers and scientists are continually working on further development of Doppler weather radar and its application to make the radar products more reliable and to accomplish tasks that seemed impossible just a few decades ago (Doviak and Zrnić 1993, Zahrai and Zrnić 1993, Galati 1993, Angevine 1997, Saffle and Johnson 1997, Zrnić and Ryzhkov 1999; Martner and Moran 2001, Brandes 2000, and many others.). One of the recent achievements in weather radar meteorology is the development of dual polarization radar. Dual polarization radar transmits and receives not only a horizontally polarized wave as conventional weather radar, but also an additional vertically polarized wave. This permits assessment of the geometric properties of the scatterers, providing a new perspective about their physical properties. Computing capabilities continuously increase. Faster signal processors make spectral processing possible (the National Weather Service finished deployment of the RVP8<sup>TM</sup> digital receiver and signal processor on the WRS-88D network in December 2006). Spectral analyses can provide another more detailed view on scatterers' radial motion.

A signal can be observed in time-domain. The frequency-domain representation of a signal is called the spectrum. Because the frequency-domain is a mathematical concept, the true spectrum is not known although it can be estimated using different methods. The most documented and widely accepted (for the weather radar) signal processing spectral estimation technique uses Fourier Transformation (Doviak and Zrnić 1993, Zrnić 1975). Other spectral estimation techniques based on harmonic decomposition can be beneficial if additional statistical information about the signal is available. For example, the Multiple Signal Classification method (MUSIC) (Hayes 1996) is applicable if the signal can be modeled by an autoregressive process so that it consists of complex exponentials, and the number of composite exponentials is known.

In non-technical terms, a power spectrum shows distribution of power in frequency, which for weather radar applications can be translated to the corresponding radial velocity. Thus the power spectrum is commonly referred to as the Doppler spectrum. Such distribution exposes signal content, depicting clutter and artifacts as well as the constructive components of the weather signal. In general, the spectrum of weather signals has a Gaussian shaped hump which is superposed on the noise floor (Zrnić 1975, Zrnić and Doviak 1978). The location of the Gaussian peak indicates the mean radial velocity of the detected scatterers. Presence of non-weather scatterers results in additional peak(s) in the spectrum. For example, echoes from ground clutter appear in the spectrum at zero velocity. When a peak in the spectrum

from weather is at non-zero velocity then a peak from ground clutter can be easily filtered.

Several parameters and variables used in weather radar applications and algorithms are derived from the three moments of the Doppler spectrum: mean power, mean velocity, and velocity dispersion. These moments can be computed in either time-domain or frequency-domain (Doviak and Zrnić 1993). The time-domain computations are simple and fast. Only a sequential operation on consecutive pairs of pulses is required for the Doppler velocity computations. The frequency-domain techniques are computationally intensive and require operations on a large sequence of pulses (64 or more). But, with careful spectral analyses the frequency-domain techniques result in signal enhancement, clutter suppression, and allow signal exploration and consequent discrimination of different scatterer types within a single resolution volume, which can not be achieved in the time-domain. Nonetheless, real time processing requirement at this time (year 2006) are primarily met with the time-domain processing techniques. Conversely, there is a major drawback to the time-domain computations. Time-domain weather radar signal processing is sometimes based on the Gaussian shape of the Doppler Spectrum (Doviak and Zrnić 1993) or spectral symmetry. A Gaussian shape is completely described by its mean and variance. Therefore the weather spectral moments (mean power, mean velocity and velocity dispersion) fully describe the mathematical model of the Doppler spectrum of weather. However, there are cases when two or more types of scatterers are mixed in the resolution volume. If neither type is dominant the resulting distribution of

powers is intricate and can be envisaged as a composite formed from two or more overlapped Gaussian spectra. Such a multi-modal spectrum cannot be characterized by its mean and variance alone. Therefore the weather radar moments and polarimetric variables computed with standard techniques (Doviak and Zrnić 1993) produce biased and unreliable moments when two or more types of scatterers are present in the radar resolution volume. One important contribution of this research is the finding that such situations can occur during bird migration periods. Censoring contaminated data has been the previous approach for dealing with such situations.

The National Weather Service maintains a network of Weather Surveillance Doppler Radars (WSR-88D) for observing weather and making quantitative measurements of precipitation and wind. Currently, data with low signal-to-noise ratio (SNR) on the WSR-88D network is discarded (censored) as unreliable (NEXRAD technical manual 1998). The value of noise is estimated at the highest elevation of volume scan and scaled for the appropriate elevation using a scalar from predetermined table.

The quality of the weather radar data is important for any meteorological algorithm or application. Censoring sometimes results in a very sparsely filled radar display. However, there is no guarantee that the presumably “good” data which passed the censorship is not contaminated as well. Clear air cases pose a problem for the radar applications during bird migration in spring and fall. The following scrutiny uncovers the reason for the problem. First, clear air data generally have low SNR and therefore a portion of clear air returns gets censored. Second, migrating birds’

presence increases signal power and therefore a portion of returns from birds does not get censored. The worst outcome occurs when the contaminated data is not censored. The retrieval of wind velocity and clear air reflectivity from such messed-up data is questionable. Moreover, there is no way to determine if the moments on a PPI are trustworthy by just looking at it. To become aware of contamination, meteorologists have to possess experience and pattern recognition skills. The resulting values of biased moments propagate errors into the corresponding radar products and classification algorithms. Therefore, current censoring schemes can waste resources by discarding large sections of data and fail to guarantee the meteorological integrity of the uncensored data. This motivated me to set aside the conventional moment estimating techniques, to eliminate thresholds, and to seek out a way for observing multiple movements ongoing in the resolution volumes. I ascertain a spectral approach to investigate and utilize the information from the data with low SNR and large spectral width. In this dissertation I present techniques for retrieving winds from the contaminated data and a methodology for assessment of the degree of contamination on a radar display.

*Vertical profiles of wind* are a routine product from the WSR-88D. The winds are obtained in *clear air* using analysis of the velocity azimuth display (VAD) data (Lhermitte and Atlas 1961; Rabin and Zrnić 1980) and are available whenever backscattering is sufficient to produce detectable signals. Throughout much of the US and during warm seasons such backscattering is provided by insects present in the PBL. *Insects* in this dissertation refers to a collection of small organisms, including

arachnid and insects that float, drift, or fly in great numbers in the air, analogous to plankton in water. Microinsects are weak flyers, their deliberate or inadvertent motion is primarily wind driven. Thus insects often behave as quasi passive wind tracers. It is this property that makes them suitable for wind measurements with Doppler radars. Insects ascend to altitudes of several hundred meters above the ground where they ride the airstreams crossing many kilometers in a single flight (Chapman et al. 2004). Other passive wind tracers such as perturbations in refractive index or smoke plumes are also detected, often together with insects. Insects take advantage of the wind to travel faster and further than they would using their wing power alone. Insects traveling both with and against the wind can lead to radar echoes that may introduce a small bias into the wind velocity estimation. Typically, the airspeed values for small insects (spider, plant lice, fruit fly) are below  $2 \text{ m s}^{-1}$  (Chapman et al. 2004, Pedgley et al. 1982) although the values for large insects (grasshoppers) can be as high as  $8.3 \text{ m s}^{-1}$  (Riley 1999). Because most insects are small, they are very hard to photograph or observe in the sky with a naked eye. Aerial netting is required to evaluate the insect-sample content. I do not have means to capture the insect-sample and, therefore, no direct way to determine if the insects are passive or active. Nonetheless, radar detects insects. Regardless of the fact that the insects may fly or drift, they are good scatterers and thus provide backscattering to weather radar in clear air conditions. In this dissertation I present methods to measure the speed of the insects carried by the wind, as well as a method to possibly estimate the velocities of wind and active insects.

There are also larger active flyers including birds and bats that are seen by the radar and that move at speeds quite different than the wind and thus contaminate the radar products. I refer to all such scatterers as *birds*. Typically birds are larger than insects and, therefore, their activities in the lower PBL can be observed. Obvious among these are nocturnal migrating songbirds (passerines) which lift just after sunset, migrate until dawn, and rest during day hours to avoid predators. Most of the migratory bird movements occur at altitudes below 3 km with the bulk of action under 900 meters (npwrc.usgs.gov 2005). Bird flight velocities range from 8 to 22 m s<sup>-1</sup> (Gill 1994), and are comparable to or stronger than typical clear air wind velocities. Nonetheless, the wind velocity estimate is minimally affected by bird echoes as long as the birds' concentration is small. However, during bird migration the level of the airborne clutter can become so significant that the radar displays "bloom" due to bird echoes. If birds ride with the wind, the total speed of flight is the sum of the wind and bird velocities. The radar wind velocity estimate in such cases is wrong and represents neither bird nor wind velocity. The task of estimating the bias due to bird echoes becomes unfeasible with current technology if different birds travel at different speeds and/or directions. During the bird migration season in spring and fall, standard estimates of Doppler shifts are contaminated by contributions from bird speeds and therefore are not suitable for meteorological interpretation. Nonetheless, spectral analyses of such data can be used to retrieve both weather and birds signals. Lofted insects enhance echoes needed for wind profiling, whereas migrating and wandering birds bias Doppler wind measurements (Achtmeier 1991,

Wilczak et al. 1995, Zrnić and Ryzhkov 1998, Zhang et al. 2005). Spectral analyses can identify peaks contributed by different types of scatterers. Spectral polarimetric analyses identify the types contributing to a particular spectral peak as being birds or insects. Both ornithologist and meteorologist who use Doppler radars to observe either birds or weather can benefit from this. I present the spectral velocity azimuth technique for extracting both dynamics of the wind and of birds.

Traditional spectral analyses assume manipulations on power spectra in the frequency domain to enhance the quality of the signal. There are two channels in the dual polarization radar and four pertinent polarimetric variables (power, differential reflectivity, copolar correlation coefficient and differential phase). The two power spectra are derived from complex spectral amplitudes; one for each channel. Spectral density of differential reflectivity is computed directly from the spectral coefficients of the two power spectra. Spectral density of copolar correlation and differential phase are derived from the complex amplitudes of spectral coefficients of the two channels. The spectral densities of polarimetric variables are novel quantities. They can be viewed as distributions of polarimetric variables in the Doppler velocity space. Definition and computations of these are addressed herein. Scatterers with different polarimetric properties can be recognized from simultaneous analysis of power spectra and polarimetric spectral densities. The distribution of polarimetric variables in velocity provides a unique way for observing multiple processes in each resolution volume and understanding the values of the resulting polarimetric averages.

## **1.1. Scope of dissertation**

I examine a precipitation-free case with at least two types of biological scatterers mixed within each resolution volume and over a large region. The case was observed with the KOUN S-band dual polarization radar in Norman, OK. The data was collected in the evening at unevenly spaced time intervals between 6 pm and 11 pm on September 7 2004 during the beginning of fall migration season (Section 5). The case covers a time interval during which the PBL occupants gradually change from diurnal insects to nocturnal migrating birds. These data capture the evolution of the transition process between diurnal and nocturnal scatterers. The early evening data contain a mixture of at least two diurnal types of scatterers, whereas the late evening data encompass a mixture of at least two nocturnal types of scatterers.

I believe that this is the first documentation of widespread echoes caused by simultaneous presence of birds and nocturnal insects in the resolution volume of weather surveillance radar. Because there was nothing unusual or special on that evening I suspect that simultaneous presence of insects and migrating birds is rather ubiquitous. However, there could be seasonal differences. Insects might be less numerous and less mature in early spring during the beginning of bird migration period than in the summer and fall; hence their contribution to radar return would be smaller.

## **1.2. Problems**

The clear air wind estimates from radar can be misleading or incorrect. Several questions arise from this. First, is there a way to tell if the radar velocity represents wind and not something else, such as a mix of wind with insects and/or birds? Second, is there a way to extract the true wind velocity from a mixed echo? Third, can the other contributors be recognized and can their dynamics be assessed? And last, what causes unusual values of the polarimetric variables which often appear on the radar displays in clear air?

## **1.3. Proposed Solutions**

I hypothesize that spectral analyses can expose presence of multiple scatterer types in a radar resolution volume if the types possess different radial velocities and produce detectable backscattered signal. I propose to use novel spectral polarimetric densities instead of former mean values. For example, for each former single value of the polarimetric variable there is a novel distribution (spectral density) of this polarimetric variable in Doppler velocity space. I speculate that such distributions will expose polarimetric properties for scatterers with different radial velocities in a resolution volume. Because the returns from one resolution volume are not statistically reliable, range averaging of polarimetric densities can be used.

Novel spectral velocity azimuth displays can be constructed so that polarimetric variables are displayed as functions of radial velocity and azimuth. Such display will provide insight on mean motions, their intensities and polarimetric properties, and

therefore, provide information for data quality assessment (Bachmann and Zrnic 2007).

The data contaminated by birds can be corrected by eliminating bird-caused peaks and tracks in the spectra in many cases if there are differences in birds' and insects' radial velocities (Section 5.6). If only single polarization data are available, the general idea is to process a segment of the data such that the wind spectral signatures can be recognized and rules for separation can be devised.

The dual polarization time-series data offer a better way of distinguishing between bird and insect spectral signatures, minimizing or even eliminating the necessity for segmentation. Judicious spectral analysis can identify and discriminate echoes from the two scatterer types; examples presented in this work explore this possibility (Section 6.1). For the first time spectral densities of three polarimetric variables are investigated and spectral azimuth displays (spectral VAD) are constructed (Section 6.4). The spectra presented in the VAD format facilitate visual separation of insect contributions from bird contributions. To explain the peculiar shapes and unrealistic values of the polarimetric variables which often occur on the radar displays, the evolution of spectral polarimetric densities from the early to late evening is investigated (Section 7). The polarimetric properties of scatterers contributing to clear air returns are examined in azimuth and in time from an ensemble of two-dimensional (2D) histograms. The echo types are recognized and a novel approach for VAD analysis from histograms (Section 7) is presented. The mean flows of different scatterer types are deduced from the clusters with large occurrences

and similar polarimetric properties in the histograms of polarimetric density and velocity. The degree of contamination on a radar display can be assessed from such VAD. A novel display called 3DASH (three dimensional azimuthal spectral histogram) is presented for visualization of the 2D histograms. The intrinsic polarimetric value for different scatterer types and the dynamic range of these values in azimuth can be assessed and used in echo classification algorithms. A potential of parametric spectral analyses to discriminate true wind from mixed active and passive insects' returns is explored in Section 8.

## **2. Background**

This section introduces the Doppler weather radar and its data acquisition. Two conventional methods (Time-Domain and Frequency-Domain) for computing Doppler moments and polarimetric variables from the acquired data are discussed. The discussion is followed by a review of conventional computation of Doppler moments and polarimetric variables from the Doppler spectrum (Frequency-Domain). A spectral ground clutter mitigation techniques is described. The section concludes with a summary of alternative spectral estimation techniques.

### **2.1. Doppler weather radar**

Radar transmits a beam of RF energy and detects the returned echoes. A beam of RF energy is transmitted in discrete pulses which propagate away from the radar antenna at the speed of light  $c$ . Pulsed transmission is used to obtain range and motion information of the scatterers. Typical weather radar transmits megawatts of peak power. The power within the beam is not uniform. The beam has a main lobe and weaker side lobes. Maximum power in the main beam lies along the beam centerline (Figure 2.1). The half-power circle is the locus of points where the power of transmitted energy has decreased to one-half of the maximum power. The collection of such circles for all ranges defines a core, which is considered to effectively contain the radar beam. A core of the beam roughly resembles a cone, as shown in Figure 2.1. The 3 dB beam-width is defined as the angular width of the radar beam subtended by this half-power core. Each pulse of electromagnetic energy (EM) is mainly contained

within the beam half-power core. Radar pulse volume is defined by the wavelength of the transmitted energy, the shape and size of the radar antenna, and the transmitted pulse width. The radar pulse volume increases with range, as indicated in Figure 2.1, although all of the shown transmitted pulses have the same duration. Radar detects echoes that return from the scatterers illuminated by the radar beam. The electromagnetic energy of the transmitted beam on the propagation way to the scatterers is absorbed, diffracted, refracted, and reflected. The energy reflected from scatterers experiences additional absorption, refraction, and reflection on the return trip back to the receive antenna. Thus, only a fraction of the transmitted power is incident on the receiving antenna. Attenuation is caused by atmospheric gases, particles, and precipitation. The radar resolution volume determines the region in space that contributes most energy to the returned signal. The amount of energy backscattered to the radar depends on the material of the scatterer, its position in the resolution volume, size, and orientation. The radar receiver is very sensitive and is capable of detecting powers as small as  $10^{-14}$  W. The received signals are mixed with a reference signal of the intermediate frequency (57.6 MHz) and amplified. The echo voltage  $V$  which is proportional to the electric field reflected from a point scatterer has a phase  $\psi_e$  with respect to the transmitted pulse. The phase  $\psi_e$  from a stationary scatterer is time independent. If the distance between radar and scatterer changes, the phase also changes, creating a phase shift called the Doppler shift. Therefore, scatterer echoes from two pulses transmitted at different time instances can be used to estimate Doppler shift and, essentially, radial velocity of the scatterer. Conceptually,

positive Doppler shift, corresponding to a negative radial velocity, indicates motion toward radar. Negative Doppler shift, related to positive velocity, shows motion of scatterers away from the radar.

## 2.2. Time-series data

The Doppler radar receiver has two synchronous detectors which detect in-phase I and quadrature-phase Q components of the echo signal  $V$ . According to Euler's relation the echo voltage can be represented by a two-dimensional phasor diagram in a complex plane (Figure 2.2). The successive values of I-Q samples, measured at equally spaced time intervals, constitute a time-series sequence. For example, data collection of one radial undergoes the following procedure. The radar sends a pulse of energy and switches to the listening mode. Portions of energy backscatter to the radar while pulse keeps propagating away from the radar. Backscattered energy produces a continuous signal stream, dashed curve following Pulse 1 in Figure 2.3a. The stream signal is sampled in the receiver and I-Q components are recorded. The radar sends next pulse and all procedure repeats  $M$  times. Consequently a series of pulses are sent in the same or approximately the same direction and the time-series sequence of a radial is collected. A large number of samples ( $M$ ) for each resolution volume is necessary to provide accuracy of the estimators. Single sample estimates would produce large errors. The dimensions of a radial of time-series data are  $M \times N$ , where  $N$  is the number of range locations determined by the sampling rate  $\tau$  and the pulse

repetition time (PRT,  $T_s$ ). The PRT determines the unambiguous range  $R_a$  and velocity  $v_a$

$$R_a = cT_s / 2, \quad (2.1)$$

$$v_a = \lambda / 4T_s, \quad (2.2)$$

where  $\lambda$  is the wavelength. These two are coupled through the range velocity ambiguity relation: radar can either observe a large range and a small unambiguous velocity interval, or a short range and larger velocities (Doviak and Zrnić 1993, Stimson 1998). The sampling rate is on the order of microseconds (e.g., 1.6  $\mu$ s); and the PRT is near a millisecond (e.g., 780  $\mu$ s). Many ( $M$ ), I-Q samples from the same range location are processed to generate spectral moments, as shown in Figure 2.3b and 2.3c: a solid parallelogram surrounds samples contributing to an estimate at one range location as indicated. Collection of spectral moments from consecutive range locations makes a radial of processed data. A radial of time-series data is defined as equally spaced I-Q samples along range. A cut is defined as a scan at a fixed elevation. Cut consists of many radials. Cut displayed in a polar coordinate system as a plane position indicator (PPI). Radar on a PPI is located in the center; range rings represent distance. Azimuth on the PPI is increasing in clockwise direction from North – top most point on the circle. Distant ranges on the PPI are higher in the atmosphere than close ranges due to elevation of the radar beam and Earth's curvature. Radar data usually include many cuts. Cuts can be scanned with different or constant settings. When nothing in the radar settings is changed from cut to cut the

scan is continuous. A volume coverage pattern (VCP) is a collection of cuts designed to cover a volume for a specific data collection.

### **2.3. Dual polarization Doppler radar**

Dual polarization radar can transmit/receive two linear orthogonally polarized waves of EM energy. Polarization refers to the orientation of the electric field in the plane perpendicular to the direction of propagation. One of the linear polarizations is referred as horizontal (H) and the other, perpendicular to it, as vertical (V). The backscattered power depends on the backscattering cross section, which in turn depends on the size, shape, orientation, and dielectric constant of the scatterer (Achtmeier 1991). If the scatterers are not spherical, the horizontally and vertically polarized return powers are not the same. The two polarizations enable obtaining scatterers' spatial characteristics (irregularity in shape, spatial orientation, and dimension). The polarimetric variables are related to the integral properties of contributing scatterers (Zrnić and Ryzhkov 1998).

### **2.4. Moments and Polarimetric Variables**

Time-series data are processed to extract desired information: spectral moments and polarimetric variables that can be later processed by the meteorological or other application algorithms. Three spectral moments are commonly obtained: (zeroth moment) mean power is used to estimate the water content of the atmosphere; (first moment) mean motion shows the radial velocities and direction of the air toward or away from the radar; and (second moment) velocity dispersion estimates shear and

turbulence. There are several polarimetric variables, and among those relevant to this work are: differential reflectivity, differential phase, and copolar correlation coefficient. Moments can be estimated from two processing domains: time domain or frequency domain. Time processing domain uses autocorrelation function, is computationally simple, and is sometimes based on Gaussian model or spectral symmetry. Frequency domain processing uses power spectral density, is more computationally intensive, but allows direct estimation of parameters from spectral coefficients and easier identification of artifacts. Power spectral density, or Doppler spectrum, can be viewed as histogram that distributes power over the velocities of scatterers, with a span from negative unambiguous to positive unambiguous velocity. Consequently, the Doppler spectrum discloses activities ongoing in a resolution volume if the scatterers backscatter sufficient powers. Traditionally, the Doppler spectrum is characterized by its spectral moments (the mean reflectivity, the mean velocity, and the peak width (Russchenberg et al., 1990)). In the case of mixed scatterers with different power and velocity characteristics, the mean values are not representative. However, the Doppler spectrum itself is a very perceptive tool.

The frequency domain estimators used in this work are summarized next. Transformation from the time domain to the frequency domain is accomplished by Fast Fourier Transformations of the time-series complex voltage  $V(m)$

$$Z(k) = \frac{1}{M} \sum_{m=0}^{M-1} [w(m)V(m)] \exp(-j2\pi mk / M), \quad (2.3)$$

where  $k$  is spectral coefficient number,  $Z(k)$  are spectral coefficients,  $w(m)$  is the data window (Equation 5.1),  $m = 0, 1, \dots, M - 1$ . Power spectral density (spectrum) is estimated from magnitude squared Fourier Transform of time-series data

$$\widehat{S}(k) = |Z(k)|^2, \quad (2.4)$$

where  $k = 0, 1, \dots, M - 1$ . The spectral coefficients are rearranged to center the sequence at a zero frequency component. This creates positive and negative frequencies, or Doppler velocities, representing direction toward or away from radar.

#### 2.4.1. *Signal Power and Reflectivity Estimation*

The total received power  $P$  is the summation of the magnitude squared of spectral coefficients. Noise power  $N$  can be measured or estimated from spectra and subtracted to obtain signal power (Section 5)

$$\widehat{S} = \widehat{P} - N = \sum_{k=0}^{M-1} \widehat{S}(k) - N. \quad (2.5)$$

The reflectivity factor is related to the signal power by

$$\widehat{Z}(dBZ) = 10 \log_{10}(K\widehat{S}), \quad (2.6)$$

where  $K$  is the radar calibration constant (Zrnić et al. 2005).

#### 2.4.2. *Doppler Velocity Estimation*

Generally mean radial Doppler velocity can be found according to (Doviak and Zrnić, 1984)

$$\widehat{v} = \sum_{k=0}^{M-1} v S_n(v) = \sum_{k=0}^{M-1} (v_a - \frac{2kv_a}{M}) \frac{\widehat{S}(k)}{\widehat{P}} = v_a - \frac{2v_a}{M\widehat{P}} \sum_{k=0}^{M-1} k\widehat{S}(k). \quad (2.7)$$

A clarifying example of a spectrum is given in Figure 2.4. The spectral coefficient axis can be replaced with a frequency axis or a velocity axis, as shown.

The spectral peak, indicated with a bold arrow, is located at  $k_m$  and corresponds to the

mean Doppler velocity. The estimator equation (2.7) is biased in presence of aliasing.

Correction for aliasing is achieved by centering summation on the spectral peak

$$\hat{v} = v_a - \frac{2v_a}{MP} \sum_{k=k_m-M/2}^{k_m+M/2-1} k \hat{S}[\text{mod}_M(k)], \quad (2.8)$$

where  $\text{mod}_M(k)$  is the reminder of dividing  $k$  by  $M$ .

In case of bimodal or multimodal spectrum (Figure 2.5), where only one peak represents the wind, the velocity estimate computed using the described approach will produce a result biased toward the peak of contaminant. A possible solution is to estimate velocity within the narrow window of spectral coefficients, shown with a dotted rectangle. The window parameters (location and width) for each spectrum can be deduced from synthesis of moments, polarimetric variables, and neighborhood association of related portions of data. The procedure is described in the section 5.1.

### 2.4.3. *Differential Reflectivity*

The ratio of reflected power at horizontal-vertical polarization is called differential reflectivity  $Z_{DR}$ , and is given by (Doviak and Zrníć, 1984)

$$Z_{DR} = 10 \log_{10} \frac{\langle |S_{hh}|^2 \rangle}{\langle |S_{vv}|^2 \rangle}, \quad (2.9)$$

where the subscripts of the backscatter coefficients  $S_{vv}$  and  $S_{hh}$  indicate the polarization of the received and transmitted fields; brackets denote expected value. To obtain correct differential reflectivity values requires a good match between channels. If the channels are unbalanced the differential reflectivity needs to be calibrated. Appendix A describes the calibrating procedure performed in this work.

#### 2.4.4. *Differential Phase shift*

In general, the differential phase shift  $\Phi_{DP}$  between horizontally and vertically polarized radar returns from an ensemble of discrete scatterers is a sum of two components

$$\Phi_{DP} = \delta + 2 \int K_{dp}(r) dr, \quad (2.10)$$

where  $\delta$  is the backscatter differential phase and the second term is a propagation component, due to the difference in forward scattering amplitudes at orthogonal polarizations. The backscatter differential phase  $\delta$  is related to the scatterers in the resolution volume via (Doviak and Zrnić, 1984)

$$\delta = \arg \langle S_{vv} S_{hh}^* \rangle, \quad (2.11)$$

where \* stands for conjugate and brackets denote expected value. In the atmosphere with precipitation, horizontally polarized waves experience larger phase shifts and propagate slower than the vertically polarized waves due to the oblate shape of raindrops and their orientation.

The values of polarimetric variables depend on the radar wavelength compared to the size of scattering particles. For example, spherical particles with diameters less than  $0.1\lambda$  are classified as Rayleigh (backscattering cross section is proportional to the diameter-to-the-sixth); particles with diameters between  $0.1\lambda$  and  $\lambda$  are in the Mie or resonance region (Rinehart 1997). Backscatter differential phase indicates well if the particle is small relative to the wavelength or not.

#### 2.4.5. Copolar correlation coefficient

Correlation coefficient between copolar horizontally and vertically polarized echo signals  $\rho_{hv}$  is defined by Zrnić et al. (1994) its relation to the cross spectrum is explained in the appendix C.

$$\rho_{hv}(0) = \frac{\langle S_{vv} S_{hh}^* \rangle}{\langle |S_{vv}|^2 \rangle^{1/2} \langle |S_{hh}|^2 \rangle^{1/2}}. \quad (2.12)$$

Each subscript in  $\rho_{hv}$  indicates the horizontal and vertical polarization. The copolar correlation coefficient is generally complex  $|\rho_{hv}|e^{j\delta}$ . Therefore, often the absolute value of the copolar correlation coefficient  $|\rho_{hv}|$  is referred as the copolar correlation coefficient. This convention is followed from here on, and to shorten notation, the magnitude sign is dropped.

### 2.5. Ground Clutter

Ground clutter are the echoes from objects on the ground. The contribution from ground scatterers are usually very large with respect to other echoes, and therefore can be easily recognized (Accu-Weather 1995). Ground-based obstacles may be immediately in the line of site of the main radar beam, for instance hills, tall buildings, or towers. Alternatively, the returns may be from objects, which although not directly within the field of view of the main radar beam, are present within one of the side-lobes of the radar beam. In this case, even though the side-lobe power is much lower than that of the main beam, the return may still be large due to the closeness of the obstacle, and/or its large cross section (Stimson 1998).

Mitigation of clutter can improve the radar parameter estimators. One of the ground clutter suppression techniques “notch and interpolate” is briefly described next. Spectrum is examined at zero Doppler velocity on the high power content. An example in Figure 2.6 shows spectrum with indicated signal peak and ground clutter peak. The high power at zero velocity is notched and the “hole” is interpolated to the level of neighboring spectral coefficients, dashed line in Figure 2.6. The width of the notch is flexible and can occupy several spectral coefficients.

## **2.6. Parametric Spectral Processing**

The Fourier transform of the data from a sample realization (eq.2.3) does not provide statistically reliable estimate of the underlying spectrum (Hayes 1996). The estimation of power spectrum can be facilitated if something is known about the process in addition to the signal values. If a process can be modeled, than this model can be used to estimate the spectrum. A random process can be modeled by filtering unit variance white noise with a causal linear shift invariant filter which is mathematically represented by a ratio of two polynomials (Hayes 1996). Such signal can be categorized as AR (autoregressive), MA (moving average), or ARMA (autoregressive moving average) processes. The AR( $p$ ) process is described by a constant in numerator and a polynomial of order  $p$  in denominator. The MA( $q$ ) process is described by only numerator of order  $q$  and a unit in denominator. The ARMA( $q,p$ ) process requires both denominator and numerator.

A practical signal can be approximated by any one AR, MA, or ARMA models. The type of model with the smallest order (for fastest computation) which captures the essence of the signal (and avoids biases by noise) is generally chosen as the best approximation. The model order is estimated using different criteria, e.g., *Akaike Information Criteria* or *Minimum Description Length* (Hayes 1996). Sometimes the model order is assessed by examining the whiteness of the residual of the original signal passed through the inverse filter. At other times the model order is known.

There are several methods to estimate the spectrum: the autocorrelation method, the covariance method, the modified covariance method, the Burg algorithm, Multiple Signal Classification method MUSIC, and other (Hayes 1996). These are called parametric spectral estimation techniques. The signal received by the weather radar can be approximated by any of these models. Thus the obtained parameters of the received signal will describe the underlying physical process(es) responsible for the signal.

Parametric techniques are based on harmonic decomposition and can be beneficial if additional statistical information about the signal is available. If a signal can be modeled by an autoregressive process so that it consists of complex exponentials and the number of the composite exponentials is known, then its spectrum can be estimated with MUSIC. MUSIC estimates the frequencies of complex sinusoids in noise (Hayes 1996). In MUSIC the Eigen values of the autocorrelation matrix are arranged in decreasing order. Then, the corresponding eigenvectors can be divided into two groups: the signal eigenvectors and the noise

eigenvectors. The frequencies of complex exponentials can be estimated from the signal group of Eigenvectors (Hayes 1996). The frequency can be translated to the radial velocity. Therefore the method can pinpoint the velocities of contributing scatterers. The signal power in parametric methods is not preserved. The parametric methods will model any specified number of composite complex exponentials and therefore need to be used carefully with a prior knowledge and a sufficient understanding of the commotion in a modeled signal. In the case of clear air contaminated by biological scatterers, if the signal is modeled correctly it will pinpoint the mean radial velocity of echoes within the resolution volume from (1) motion of air masses enhanced by wind-blown insects; (2) motion of active insects; (3) bird motion. Therefore, the parametric modeling with model order 2 can be useful to determine the birds and insects mean velocities. Potentially, the parametric model order 3 might be able to isolate the bird-, wind-blown-insect- and active-insect-velocities (Section 8).

### **3. Literature Survey**

This section provides available facts and reported findings on topics relevant to this dissertation. The material is arranged in subsections such that each addresses a separate topic. First, the reports on clear air radar observation are recapped. These are followed by a review of attempts to improve velocity estimation in clear air conditions. The radar observations of bird migration and polarimetric radar observation are surveyed next. And last, two subsections (Birds and Insects) provide summed up facts helpful for understanding behavior and activities of biological scatterers over the Great Plains of Oklahoma.

#### **3.1. Precipitation-free radar observation**

Boundary layer clear air radar echoes are a common occurrence over land areas from spring through fall (Gossard 1990, Wilson et al. 1994). Vaughn (1985) attributes these echoes to the birds and insects, which from spring through fall are generally abundant in the atmosphere up to an altitude of 2 km over most land areas of the world. Available data on the insect densities and radar cross sections generally agrees with observed clear air reflectivity factors that typically range between 5 and 10 dBZ with maxima as high as 20-35 dBZ within convergence lines (Wilson et al. 1994). Wilson et al. (1994) attribute the clear air echoes to the refractive index perturbations (Bragg scattering), insects, and birds (particulate scattering). They suspect that insects are the primary contributor to the widespread nature of the echo while birds are more responsible for sporadic points of intense reflectivity.

Schuur et al. (2003) point out that the biological scatterers represent the overwhelming majority of clear air scatterers (along with small-scale non uniformities of refractive index caused by turbulence) and include bats in the biological scatterers' category. Zrnić and Ryzhkov (1998) state that at centimeter wavelengths, echoes in the PBL during warm seasons are primarily caused by insects, however, a substantial portion of nocturnal echoes in spring and fall is caused by migrating songbirds. In the clear air PBL the scatterers may be gradients of the refractive index or biological scatterers or a combination of both (Achtmeier 1991).

It is now well established that, at least in the convective boundary layer over land, the echoes from optically clear atmosphere are largely due to scattering by insects rather than to refractive index perturbations (Russell and Wilson 1997; Riley 1999; Geerts and Miao 2005). The presence of biological scatterers introduces uncertainty in explanation of velocity fields obtained with the weather radar. The radar velocities may be affected by insect motion (Achtmeier 1991; Wilson et al. 1994; Dean and Drake 2002) and certainly are affected by bird motion. Wind estimates from the Doppler velocities in the PBL, contaminated by migrating birds and insects, are suspect.

### **3.2. Attempts to improve wind velocity estimates**

Rabin and Zrnić (1979) applied the VAD technique to unevenly spaced data obtained with two nearby Doppler weather radars in the optically clear atmosphere. They suggest the possibility of mapping the divergence and vertical motion at various

heights in the PBL as a continuous function of time. Wilson et al. (1994) investigate clear air echoes from insects and the accuracy of the derived winds. They observe good agreement between balloon-sounding winds and those from VAD technique. Other investigators (Mueller and Larkin 1985, Achtemeier 1991) on the contrary report errors in the wind estimates due to the insects.

Wilczak et al. (1995) state that winds measured with wind profiler frequently have nonrandom errors as large as  $15 \text{ m s}^{-1}$  when compared to simultaneously measured rawinsonde winds. Wind profilers are extremely sensitive to migrating birds; for the 404-MHz profiler, only 22 birds per cubic kilometer will contaminate the profiler winds at 3 km, in case of calm background wind (Wilczak et al. 1995). Wilczak et al. (1995) base their technique on the difference in the power distributions for turbulence (exponentially distributed) and point scatterers (non-exponentially distributed). They suggest collecting a number (34) of spectra at each range. Then they sort powers at each velocity bin; perform exponential fit and discard coefficients having non-exponential distribution. They find the mean from the remaining values and use resulting averaged spectrum with partially removed bird echoes for usual moment calculation.

Gauthreaux et al. (1998) quantifies the patterns of bird movements and studies bias of the wind estimates caused by birds. Jungbluth et al. (1995) also shows that Doppler velocities measured by the radar are different from the wind velocities in the presence of migrating birds.

Griesser and Richner (1998) develop an algorithm for the wind profiler to separate atmospheric signal when it is obscured or dominated by other sources. The multiple peak processing algorithm is based on simultaneous identification and characterization of several peaks in a Doppler spectrum using a spatial, modal, and temporal continuity scheme. For a boundary layer wind profiler, bird signals most often dominate the clear air echoes. Significant changes in the types of insects and birds occupying the atmosphere are well correlated with sunset and sunrise. Rising/descending birds cause increase/drop in signal to noise ratio of 20 to 40 dB. Griesser and Richner (1998) exclude bird contaminated data by manually flagging suspect clusters between sunset and sunrise. Further, they report that during the migrating periods, often false wind was calculated from the radar data.

Holleman et al. (2005) describe how standard deviation of the radial velocity can be used to separate the profile data from the Doppler weather radar into the true wind vectors and bird movement vectors.

Cornman et al. (1998) presents NCAR Improved Moments Algorithm NIMA – a spectral level quality algorithm that uses fuzzy logic approach for improved moment estimation. Morse et al. (2002) advance NIMA for improved moment estimation from Doppler spectra that uses mathematical analyses, fuzzy logic synthesis, and global image processing algorithms to mimic human experts' ability to identify atmospheric signal in presence of contaminants from a variety of sources (aircraft, bird, ground clutter, etc.). At several steps in the analysis the spectra are 2D median filtered. They report improved velocity estimates but the birds they encounter are

wandering not migrating, because the echoes from these birds are sparse and exhibit different velocities and directions.

Winston et al. (2003) assess the improved spectral moment selection algorithms on an operational clear air Doppler wind profiler and report increased overall data recovery, significant improvement in the wind measurement during precipitation, and in a presence of strong ground clutter. Winston et al. (2003) also reported that in some conditions current algorithm does not select the correct atmospheric signal for some interval. The conditions were not described and therefore may be attributed to the contamination by birds.

I established that the migrating birds badly contaminate wind fields and that an effective decontamination technique has not been developed yet.

### **3.3. Radar observation of bird migration**

Northern Prairie Biological Resources ([npwrc.usgs.gov](http://npwrc.usgs.gov)) assert that radar observations have shown that nocturnal migration begins about an hour after sundown, reaches a maximum shortly before midnight, and then gradually declines until daybreak. Bird echoes during peak migration periods may cover a radar screen. During both spring and fall migrations, radar studies have demonstrated that weather has a defining role in determining the beginning of migration. The primary stimulus for departure is a following wind; in the spring this is a wind from the south, in the fall it is a wind from the north (Gill 1994). Clear skies, presumably providing for

celestial orientation cues, are of secondary importance, since major flights will occur under overcast if adequate tail winds are blowing (npwrc.usgs.gov).

When winds aloft are nearly calm and variable in direction, the data in the VAD wind profile and base velocity products may pertain almost exclusively to migrating birds (Gauthreaux et al. 1998).

Recognition of birds in the Doppler spectra of surveillance radars should be possible from the beat frequency of flapping wings (npwrc.usgs.gov). The wing beat frequencies of birds typically range from 2 to 5 Hz and should appear in spectrum as side peaks with modulation shift of 0.1 to 0.25 m s<sup>-1</sup>. However, the beating of the wings cannot be observed in the regular spectra due to limited resolution – e.g., for unambiguous velocity interval between –35 m s<sup>-1</sup> to 35 m s<sup>-1</sup>, there should be at least 280 samples in order to detect 0.25 m s<sup>-1</sup> peak. Furthermore, not all birds flap their wings. Many birds with large wings appear hanging in the air effortlessly or climbing up with barely a twitch of a wing, gliding or soaring. A class of methods that offers possibilities to detect biological scatterers and distinguish between insects and birds relies on radar polarimetry. Combined use of polarimetric and Doppler variables should lead to the recognition of situations where the biological scatterers are tracers of large scale winds (Mueller and Larkin 1985). Further, polarimetry might lead to an estimation of sizes and thus, species of some birds or insects could be inferred.

### 3.4. Polarimetric radar observation

Dependency of the radar returns from insects and birds on polarization have been confirmed by many investigators (Riley 1985; Mueller and Larkin 1985; Zrnić and Ryzhkov 1998, Zhang et al. 2004). The polarimetric signatures of insects and birds are different due to the difference in shape, size, and orientation of the scatterers.

Mueller and Larkin (1985) used dual-polarization Doppler radar during a clear air night when a large number of insects are aloft. The authors exploited a low power X-band (3 cm) tracker to obtain the distribution and altitude information and a high power S-band (10 cm) dual-polarization Doppler radar for differential reflectivity observation. They conclude that the observed echoes are caused by insects that produce significant differential reflectivity compared to zero  $Z_{DR}$  of refractive index fluctuations, and report errors of several meters per second in the wind speed due to the additional insect speed. They measure  $Z_{DR}$  of up to 7 dB in the direction perpendicular to the wind and assume that insects are nocturnal moths.

Achtemeier (1991) observes the interaction between a gust flow and a deep cloud of insects using dual-polarization radar. He shows that the insects (grasshoppers) are not valid tracers of air motion. He measures  $Z_{DR}$  between 8 and 9 dB.

Zrnić and Ryzhkov (1998) report significant differences in polarimetric properties of small Rayleigh scatterers like insects and big non-Rayleigh scatterers like birds and show that birds have larger differential phase upon scattering and lower differential reflectivity than insects. They attribute echoes between 20 and 40 km in range with  $Z_{DR}$  between 2 and 9 dB and  $\Phi_{DP}$  of less than  $40^\circ$  to insects; and echoes

with  $Z_{DR}$  between  $-1$  and  $3$  dB with considerably larger differential phase (sometimes over  $100^\circ$ ) to birds. They also report that the cross-correlation coefficient is similar for both types of scatterers and is between  $0.3$  and  $0.5$ .

Schuur et al. (2003) classify polarimetric radar echoes, using membership functions, into three classes (1) meteorological scatterers, (2) biological scatterers, and (3) ground clutter / anomalous propagation. Their classification algorithm does not make a distinction between insects and birds combining both into the “biological scatterers” class. Schuur et al. (2003) report strong azimuthal dependence and state that at certain azimuths (usually close to the main wind direction) the differential reflectivity and phase for birds and insects are very similar.

Zhang et al. (2004) observed the transition between birds and insects echoes and report that birds have higher differential phase and lower differential reflectivity than insects. Rapid changes in polarimetric variables at sunset and sunrise Zhang et al. (2004) attribute to the shift of the occupancy of the PBL between birds and insects. They also report gradual increase of differential reflectivity during the day and asymmetry of the azimuthal profiles with respect to the direction of bird migration. Lung et al. (2004) observed day-time clear air dumbbell-shaped echoes with S-band polarimetric radar and suspect that the echoes are caused by insects lofted to near the top of the convective boundary layer.

### **3.5. Variety of Nocturnal Migrants in the Great Plains**

#### **3.5.1. *Birds***

This section contains some helpful ornithological facts necessary to understand the migratory bird behavior and activities, to evaluate the quantity of birds uncovered on the radar displays, their flight velocities, and body sizes.

Every fall about 5 billion land birds of over 200 species migrate south from North America (Gill 1994) and every spring these billions travel back. Seasonal cycles of climate or insect abundance attract corresponding cycles of breeding, flocking, and migratory relocations. Molt and preparations for migration are triggered by changes in day length (Gill 1994). In spring, major northward movements in the US coincide with a depression (lowering of a barometric pressure) toward the southwest, followed by a strong flow of warm southern winds from the Gulf of Mexico toward the northeast.

Fall departure migrations are also stimulated by favorable weather conditions. How migrating birds forecast is a mystery, but they are sensitive to changes in barometric pressure and feed more intensively as storms approach and barometer falls. Gill (1994) specifies October as the peak month of fall migration. Wilczak et al. (1995) select May and September as the months of the peak migrations in the central United States. 716 species of birds are nesting in the USA (Gill 1994) and over 200 species migrate. The Central Flyway out of the four major North American flyways stretches above the Great Plains. I examined seasonal breeding and migration information available on the Cornell University Ornithology website

(birds.cornell.edu 2005) and estimated that more than 70 species of birds that do not breed in Oklahoma do migrate over Oklahoma. From those about 25 species have conservation status ranked as abundant and common (NatureServe 2005). The birds' average sizes vary from 11 cm to 150 cm. Gill (1994) emphasizes that the seasonal residents form a major component of most bird communities. Rich assemblages of species form foraging flocks, to search for food and look out for predators. Flocks are not limited to members of the same species. Temperate flocks average 10 to 15 birds of 6 to 7 species. Flock composition changes regularly as the flock moves along, a result of new individuals joining and others leaving (Gill 1994).

Each species has a characteristic size, shape, color, behavior, ecological niche, and geographical range. The number of bird species in the area – called species richness or diversity – increases from the Arctic to the Tropics. Observations made with telescopes focused on the full moon have shown processions of birds, and one observer estimated their passage over his area at the rate of 9,000 per hour (npwrc.usgs.gov 2005). This gives some indication of the numbers of birds in the air at night during migratory peaks.

Birds migrate by day, by night, and at both times. Migrants fly at times of the day and heights where travel is least costly, safest, and most rapid (Gill 1994). Small birds are typical nocturnal migrants. Some larger birds, like ducks and geese, also migrate at night. Nocturnal migration begins shortly after sunset, reaches a maximum before midnight, weakens by 2 AM (Gill 1994), and diminishes at daybreak. More stable night atmospheres with weaker horizontal winds and less turbulent vertical motion

create favorable flight conditions. Also, cooler and more humid night air favors heat loss and water consumption. Passerines fly in a dispersed manner rather than in a tight flock with densities often reaching  $10^{-6}$  birds per cubic meter (Wilczak et al. 1995).

The day migrants include, in addition to some of the ducks and geese, loons, cranes, gulls, pelicans, hawks, swallows, nighthawks, and swifts. Soaring birds, including Broad-winged Hawks, storks, and vultures, can only migrate during the day because their mode of flight makes them dependent on updrafts created either by thermal convection or the deflection of wind by topographic features like hills and mountain ridges (Gill 1994, npwrc.usgs.gov 2005). Swifts and swallows feed entirely on diurnal flying insects as they travel gradually southward. Similarly, large flocks of Franklin's Gulls in the Great Plains feed on insects caught in thermals, using these updrafts as a source of food as well as the means permitting soaring flight that carries them on their journey with minimal expenditure of muscle power (npwrc.usgs.gov 2005).

Diurnal and nocturnal flights offer different advantages. Hawks migrate during daylight hours when they can take advantage of warm rising air current (Gill 1994). Many sources indicate that most of the migratory activities occur below 3000 m with the bulk of the movements below 900 meters (Gill 1994, npwrc.usgs.gov 2005). For most small birds the favored altitude appears to be between 150 and 300 meters (npwrc.usgs.gov 2005). Nocturnal passerines usually migrate at altitudes below 700 meters, although they climb over 3000 meters, to escape turbulent air in the boundary

layer near Earth's surface or to ride good tailwinds (Kerlinger and Moore 1989, cited in Gill 1994). All migrants tend to fly lower into the opposing wind (Gill 1994). Bird velocities relative to ground are affected by the wind: faster for the birds going with the wind and slower for the birds opposing the wind. In general, flight velocity of birds ranges from 20 to 50 miles per hour (8 to 22 m s<sup>-1</sup>) (Gill 1994, npwrc.usgs.gov 2005). For a nonstop flight, larger birds typically fly faster than smaller birds. Probably the fastest flight over a long distance - a young little male duck traveled 3,800 miles from the delta of the Athabaska River, northern Alberta, Canada to Maracaibo, Venezuela in exactly one month. This flight was at an average speed of 125 miles per day (npwrc.usgs.gov 2005).

Most birds fly in a straight line, flapping in a constant rhythm, but certain bird groups have characteristic flight patterns: some exhibit a steep, roller-coaster flight, whereas others fly in a pattern of moderate rises and falls; some make several wing flaps followed by a glide, when others soar.

The highly developed color vision of birds reaches into the near-ultraviolet range of spectrum. The broad hearing range of birds encompasses sounds at very low frequencies – infrasound. Birds orient by Sun, Constellations; and use magnetic compass that responds to the pole-ward and equator-ward angles of inclination with fields 10<sup>-7</sup> 10<sup>-9</sup> gauss (corresponding to natural fluctuation in the Earth's magnetic field caused by sunspots and hills of iron ore). When the Sun or Constellations are not visible, birds can navigate by means of pattern of the Earth's magnetism and can orient themselves in flight “automatically” because of their extreme sensitivity to

minuscule shifts in gravity and barometric pressure. Bird navigational abilities depend on its experience. The process of migration is typically divided into periods of refueling and flights between consecutive stopovers. Migrant North American land birds from 16 million square km of breeding range are compressed into 2 million square km of winter range in northern Central America and the West Indies.

Human activities are responsible for roughly 270 million bird deaths every year in the continental USA (2% of the birds that inhabit the US). The conflict between aircraft and birds is a real and growing problem - about 60,000 bird strikes to U.S. aircraft were reported to the FAA from 1990 to 2003, and perhaps four times that many went unreported (Cole, 2005). A 12-pound Canada goose struck by a 150-mph aircraft generates the force of a 1,000-pound weight dropped from a height of 10 feet (Bird Strike Committee USA). Damage to aircraft is estimated at \$400 million per year, and up to 400 (human) deaths have been blamed on collisions with birds (Cole, 2005).

Diehl and Larkin (2004) introduce WSR-88D for ornithological research and point that because birds and insects often migrate together, analyses of bird migrations almost invariable include some insects. Diehl and Larkin (2004) suggest several ways to minimize contribution of the insects: to use only strongest migrations that produce echo strengths generally not attainable by insects; to consider the velocities of birds and insects with respect to the winds (Gauthreaux and Belser 1998); and to use spectrum width as a criteria for separation (Larkin and Diehl 2003).

### 3.5.2. *Insects*

Insects are considered to be the most successful animals on earth in terms of number of individuals, number of species, and range of habitat (Grantham and Arnold 2005). They are the most diverse group of organisms. There are probably several million different kinds, or species, many of which have yet to be discovered. The smallest insects are too small to see. The largest flying insect is the goliath beetle of the African rain forest that can weigh over 100 grams (ornithopter.org 2005).

Most insects have four wings, but their size and arrangement varies. The wings can flap out-of-phase: front wings rise as back wings fall. Many insects, though, flap their wings in unison. In butterflies and wasps, the larger front wings overlap the hind wings, and at first glance, it appears there are only two wings. Flies have no hind wings at all, just tiny vibrating clubs that help them sense direction. A beetle's front wings form protective wing covers called elytra. In flight these provide some lift, but they don't flap much. The wings can be several times larger than the elytra but fold neatly underneath (ornithopter.org 2005). Dragonfly has four wings of about the same size.

A typical speed for insects is in the range  $1.4 - 8.3 \text{ m s}^{-1}$  (Riley 1999). Achtemeier (1991) observed large insects (grasshoppers) over North Dakota in summer 1987 with a dual-polarization radar, specifically insects response to a gust flow interacted with a dense cloud. Achtemeier (1991) claims that under certain environmental conditions the insects are not valid tracers of air motion because they respond collectively to an environmental change and may cause  $3 \text{ m s}^{-1}$  error between

a balloon measured and Doppler-deduced wind field. The airspeed of large insects such as grasshopper can range from 3 to 6 m s<sup>-1</sup> (Zarnack and Wartmann 1989 cited in Achtemeier 1991).

Chapman et al. (2004) performed aerial netting at the height 200 m above ground during summers 1999, 2000, and 2002 at Cardington, Bedfordshire, UK, to sample the windborne arthropods (insects and spiders). The study shows that some families are mainly day-flying and some show maximum aerial density at the dusk. The mean aerial density champion in all categories (day, dusk, night) of the Chapman et al. (2004) study is a small soft-bodied plant lice. However, during the dusk the density of fruit flies approaches the density of the champions. Later Chapman et al. (2005) present results from high-altitude aerial trapping and from novel insect-monitoring radar located in south-eastern Britain, and encounter aerial densities indicating that many millions of small 5 mm bronze ground diurnal beetle are on the move at high-altitude in the mid-summer. Chapman et al. (2004) state that in the USA high altitude sampling was performed by Isard et al. in 1990, and Greenstone et al. in 1991, but the taxonomic composition of high-flying nocturnal migrants has never been documented.

Microinsects have been referred to as aerial plankton (Drake and Gatehouse 1995; Russell and Wilson 1997, Geerts and Miao 2005). Geerts and Miao (2005) study the characteristics of the optically clear convective boundary layer (CBL) by means of airborne millimeter-wave Doppler radar and attribute the well-defined plumes of higher reflectivity occupying most of the depth of the clear air CBL to

small insects. Most millimeter-wave radar scatterers in the clear CBL are believed to be microinsects (Russell and Wilson 1997, Geerts and Miao 2005). The equivalent reflectivity values, computed by Geerts and Miao (2005) with an assumption that the scatterers are spherical water droplets, which is not the case, range between  $-35$  and  $-5$  dBZ in the CBL. The presence of microinsects above the surface layer appears to be a daytime phenomenon (Isard et al. 1990).

Many actively flying, large insects migrate at night (Richter et al. 1973, Schaefer 1976, cited in Geerts and Miao 2005). Geerts and Miao (2005) declare that WCR (weather cloud radar) measurements before and shortly after dawn indicate that scatterers are virtually absent in the stable boundary layer, at least in the Oklahoma Panhandle. This observation might not apply universally throughout the USA.

The CBL echoes are mostly small insects, as has been suggested by Vaughn (1985), Russell and Wilson (1997), and Riley (1999). Not only these biotic scatterers try to return to the earth surface; hydrometeors or other non flying particles, such as dust, plant material, etc., also subside. The insects documented by Geerts do not fall at a terminal velocity; they ride weak downdrafts and fly up against stronger ones. And when microinsects encounter an updraft, they actively oppose it at a rate proportional to the updraft strength. The insects lose their ability to fly in air colder than some threshold,  $18^{\circ}\text{C}$  for most insects. Achtemeier (1991) suggests that the scatterers only oppose updrafts where they encounter temperatures too low to maintain a wing beat sufficient for lift.

Feng et al. (2003) use radar, search-light trap and ground trap to observe the autumn beetle migration in China. These authors claim that only relatively large species ( $> 50$  mg) were detected with the radar. The insects traveling at  $6.9 \text{ m s}^{-1}$  are assumed to be moths and were detected up to 1.5 km in height, most were concentrated below 500 m. These insects tended to form a dense layer at altitude 200 m with the maximum volume density greater than 600 insects per cubic km (Feng et al. 2003).

## 4. Data analyses

This section contains description of data collection including radar set up and general environmental conditions, which are followed by analyses of fields of Doppler moments and polarimetric variables.

### 4.1. Radar set up

KOUN (Figure 4.1) is the NOAA/NSSL research S-band (2705 MHz) weather surveillance Doppler radar that is maintained and operated by National Severe Storm Laboratory in Norman, Oklahoma. The KOUN parabolic antenna of 8.54 m in diameter is covered by fiber glass radome and is situated on a tower about 20 meters above the ground. The antenna main-lobe one-way 3 dB beamwidth is about  $0.95^\circ$ , and a first side-lobe is 27 dB below the main-lobe. The 10-cm wavelength klystron transmitter with a nominal peak power of 750 kW can transmit in simultaneous horizontal/vertical (dual) polarization mode.

The radar was in dual polarization mode simultaneously transmitting and receiving waves of horizontal and vertical polarizations. The volume coverage pattern (VCP) was constructed in a way that the antenna scanned  $360^\circ$  sectors at elevations of  $0.5^\circ$ ,  $1.5^\circ$ ,  $2.5^\circ$ ,  $4^\circ$  and  $6^\circ$  with a pulse repetition time (PRT) of 780  $\mu\text{s}$ . The unambiguous range  $R_a$  and velocity  $v_a$  were 117 km and  $35 \text{ m s}^{-1}$ . Samples are spaced 250 m in range, and the depth of the range weighting function (Doviak and Zrnić 1993) is about 300 m. Herein the number of samples ( $M$ ) for spectral analysis is 128. National network of radars currently uses 17 and 64 samples for the reflectivity and

velocity computations respectively. Smaller  $M$  affects the spectral shape by increasing spectral width. Larger  $M$  allows better recognition of peaks closely spaced in the velocity space. The radix 2 value is generally chosen for the Fast Fourier Transformation. Obviously 128 samples provides better resolution than 64 samples ( $\sim 0.5 \text{ m s}^{-1}$  vs.  $1 \text{ m s}^{-1}$ ) but it also requires longer acquisition time. Longer time might not be acceptable for a real time application, however, it is definitely advantageous in the research application (e.g., for computing the magnitude of the cross correlation coefficient over closely spaced spectrum coefficients, section 6.1).

Due to the curvature of the radar beam its actual height  $h$  can be estimated from range  $r$  (Doviak and Zrníc 1993)

$$h = [r^2 + (k_e a)^2 + 2rk_e a \sin \theta_e]^{1/2} - k_e a, \quad (4.1)$$

where  $\theta_e$  is the elevation angle,  $a$  is the earth's radius 6372 km, and the effective radius of earth  $k_e a = \sim 4a/3$ . Figure 4.2a shows the estimated heights of the center of the radar beams at different ranges for the elevations of the presented VCP.

## 4.2. Data collection

Time-series data were collected with the KOUN on September 7, 2004 between 6 pm and 11 pm local time (23 UT on September 7, 2004 and 4 UT September 8, 2004). Each collection consists of one VCP. The intervals between collections are unsystematic. The collection times are summarized in Table 4.1. I use local time notation because it allows a natural association of the progression of the evening with the observed changes. Spectral moments were obtained and observed in real-time on

the plan-position indicator (PPI) displays while time-series data were recorded. For the PPI of polarimetric variables, the computations used the standard processing technique (Doviak and Zrnić 1993) with no censoring whatsoever. Chosen PPIs are presented for specific examples in the text. The thumbnails of all PPIs for each parameter are collected in tables to expose evolution of each parameter (Doppler moments and polarimetric variables). The collection of such tables is given in Appendices D and E. The presented parameters are reflectivity in H channel, reflectivity in V channel, velocity in H channel, copolar correlation coefficient, differential reflectivity, and backscatter differential phase. Appendix D shows PPIs with range extended to 117 km. Appendix E shows zoomed up portion of the PPIs so that the maximum range is only 33 km. First column in each table specifies the parameter, indicates the color scale and states the maximum shown range. Second and third columns show experiment number and local time for reference (Table 4.1). The rest five columns show thumbnails of PPIs at elevations indicated at the top row of each of the tables.

### **4.3. Weather conditions**

On this day fair weather prevailed over the radar coverage area. The atmospheric sounding indicates that at time 0 UT and 200 m above ground, a North-North-East wind was blowing at  $7 \text{ m s}^{-1}$  from  $25^\circ$ ; at 800 m it increased to about  $11 \text{ m s}^{-1}$  and reached a peak of  $20 \text{ m s}^{-1}$  at the top of the boundary layer (Figure 4.2b and 4.2c). However, the velocities registered on the plan position indicator are much larger,

reaching values up to  $30 \text{ m s}^{-1}$  for the late evening cases (Figure 4.5b). The speckled appearance of such fields clearly suggests presence of strong point scatterers. Radar meteorologists recognize this inconsistency and attribute it to “contamination by biological scatterers”; further they consider such velocities worthless for meteorological interpretation. I demonstrate in this work that spectral analysis and polarimetry can be used to retrieve both the winds and the bird speeds in this and similar situations.

The daily weather map ([www.hpc.ncep.noaa.gov](http://www.hpc.ncep.noaa.gov)) confirms the precipitation free conditions during the data collection times. The 24 hour precipitation map (Figure 4.3) shows no precipitation over Oklahoma during the experiment.

Table 4.1: Data collection times:

In text	Experiment	UTC	September 7, 2004													
			Local Time		18:10	18:20	19:42	19:51	20:02	20:07	20:22	20:30	20:40	21:00	21:15	22:20
6 pm	01	23:10	09-7-04		September 8, 2004											
	02	23:20	00:42	00:51	01:02	01:07	01:22	01:30	01:40	02:00	02:15	03:20	04:01			
7pm	04	00:42														
8 pm	06	00:51														
	08	01:02														
	09	01:07														
	12	01:22														
	13	01:30														
	15	01:40														
9 pm	17	02:00														
	18	02:15														
10 pm	20	03:20														
11 pm	21	04:01														

#### 4.4. Data analyses from PPI

The example of the PPI of reflectivity in H channel shown in Figure 4.4a depicts strong reflectivity around the radar and weak reflectivity elsewhere. The reflectivity is shown in logarithmic scale. Two range rings 50 km and 100 km are shown for reference. In this precipitation-free case, the majority of echoes with reflectivity  $Z_h$  above 20 dB are returns from ground clutter. These can be suppressed with a simple “notch and interpolate” spectral filter as discussed in Section 2.5. Filtered ground clutter and different color scale reveal weaker echoes in Figure 4.4b. These echoes are of main interest in this work and are contributed by the mixed biological scatterers such as *birds* and *insects*.

A PPI of Doppler velocity in clear air is expected to show wind velocity which generally ranges from 5 to 10 m s<sup>-1</sup>. Two examples of clear air velocity PPIs at 8 pm and 11 pm are presented in Figure 4.5a and 4.5b respectively. The majority of the resolution volumes in Figure 4.5a display values below 10 m s<sup>-1</sup>, although there is some contamination at farther ranges with values exceeding 15 m s<sup>-1</sup>. A worse case is depicted in Figure 4.5b with velocities exceeding 20 m s<sup>-1</sup>. Both these PPIs are contaminated although the degree of contamination is different.

Examination of all PPI displays (Appendices D, E) revealed that diurnal insects contributed to the early return and disappeared at sunset. These were followed by nocturnal birds which ascended rapidly from the ground. Nocturnal insects showed up later possibly because their ascent is slow and/or they might have taken off at a later time. Significant return power is observed in the horizontal and vertical channels

through the boundary layer up to about 2 km in height, above which noise dominates. Reflectivity values are relatively low, less than 5 dBZ.

The changes in clear air returns are easier to monitor in the PPIs of differential reflectivity  $Z_{DR}$  than in the PPIs of reflectivity of horizontal  $Z_h$  and vertical  $Z_v$  channels simultaneously. The  $Z_{DR}$  silhouette gradually changes as the evening progresses. Several characteristic examples with the vivid changes in  $Z_{DR}$  are presented in Figures 4.6 and 4.7 for elevations  $0.5^\circ$  and  $6.0^\circ$  respectively.

The  $Z_{DR}$  pattern at elevation  $0.5^\circ$  and at 6 pm extends to 80 km in range, and has a symmetric feature shaped like a bow-tie with values exceeding 10 dB. At 8 pm the pattern covers only 60 km in range; the bright bow-tie feature loses its intensity as indicated by lower  $Z_{DR}$  values, and exhibits asymmetry with lesser values to the east from the radar. After 9 pm the pattern broadens to 100 km in range. Several irregular in shape features exhibit values exceeding 10 dB and appear to the east from the radar. By 11 pm the PPI looks lighter due to lower  $Z_{DR}$  values. The pattern extends to 117 km and has patchy features with stronger and weaker than the background  $Z_{DR}$  values.

The  $Z_{DR}$  pattern at elevation  $6^\circ$  and 6 pm shows the same bow shaped feature extending to 20 km in range and additional rings with  $Z_{DR}$  values of approximately 5 dB, indicating layers of scatterers. By 8 pm both the ranges of the rings and the intensity of the bow-feature decrease. The rings merge creating asymmetric bottom layer and symmetric top layer at 9 pm. The symmetry in the top layer has different

orientation compared to 6 pm case. At 11 pm pattern is asymmetric with visible uneven layering at different azimuthal locations.

The change in area covered by the significant returns can be observed from the PPIs of copolar correlation coefficient (Appendix D). The  $\rho_{hv}$  indicates that for elevation  $0.5^\circ$  significant echoes with high correlation coefficient cover about 90 km in range at 6 pm, 60 km at 8 pm, and all 117 km after 9 pm. This information together with the differential reflectivity suggests the following interpretation. As evening progresses, the day time scatterers come down and get gradually replaced by the night time scatterers. The night time scatterers appear to backscatter more power and have different polarimetric signatures. Accordingly, the subsequent observations are drawn from analysis of all PPIs presented in Appendices D and E.

At 6 pm and below 1.5 km the scatterers appearing on PPIs have: symmetric  $Z_{DR}$  pattern with values exceeding 15 dB; about  $-30^\circ$  differential phase in a narrow sector at azimuths between  $125^\circ$  and  $200^\circ$ , and a  $30^\circ$  phase in the rest of the PPI; velocity values increasing with altitude from  $5\text{-}10\text{ m s}^{-1}$  to  $15\text{-}20\text{ m s}^{-1}$  (this is apparent from original PPI images of sufficient size, which were used to make the provided thumbnails). The zoomed thumbnails of  $\rho_{hv}$  (Appendix E) expose three more layers of scatterers at altitudes of approximately 1.5 km, 2 km and 3.5 km. The scatterers in these layers do not produce sufficient reflectivity returns, and are recognized by large values of copolar correlation coefficient. The layer at 1.5 km shows velocities exceeding  $20\text{ m s}^{-1}$ , low  $Z_{DR}$  values, and asymmetric  $\delta$  pattern with  $30^\circ$  in the west half and  $-30^\circ$  in the east half of the PPI. The polarimetric properties are similar for the

scatterers in layers above 1.5 km. The scatterers in the surface layer display different properties. The patterns at lower altitudes can be attributed to insect and the patterns at higher altitudes might be small birds.

Overall pattern changes by 8 pm. The  $Z_{DR}$  drops below 15 dB, the mirror like  $\delta$  pattern with  $30^\circ$  at west half and  $-30^\circ$  at the east half of the PPI extends to the ground, the 3.5 km altitude layer disappears. The  $\rho_{hv}$ 's zoomed thumbnails (Appendix E) indicate that the scatterers in all layers descend to form two layers: below 600 m and at 2 km altitude. The layers have different mean  $Z_{DR}$  with higher values in the lower layer. The sudden change in backscatter differential phase transforms the pattern of  $\delta$  to mimic the  $\delta$  above 1.5 km layers. The power reduces dramatically. These conditions indicate the descent of the scatterers.

Between 8 pm and 8:30 pm the bottom layer scatterers ascend and the top layer scatterers descend forming one surface layer with the  $Z_{DR}$  pattern that has more scatterers to the west from the radar. The overall pattern shows smaller  $Z_{DR}$  values. The feature to the west of the radar exposes  $Z_{DR}$  values reaching to 15 dB. The backscattered power increases and the values of  $\delta$  increase in the south east sector.

At 9 pm scatterers are distributed in the volume below 1.5 km with an evident layer at 1.5 km. The  $Z_{DR}$  in the layer show values below 5 dB. The differential phase pattern becomes more erratic with noisy patches and streaks to the west and south from the radar. The high  $Z_{DR}$  and different phase pattern suggest that another kind of insects is in the air and rising. After 9 pm the irregularities in pattern prevail. At higher elevations a well formed feature appears at about 20 km south south-west from

the radar. The feature can be characterized by smaller than the background  $Z_{DR}$  values and extremely noisy  $\delta$ . This feature is most likely birds. At 11 pm the overall differential reflectivity drops, the overall differential phase pattern changes in a way that negative phases diminish. Consequently, at 6 pm insects are dominant scatterers in the scan region. By 8 pm the principal occupants of the observed area descend and yield their place to a diverse group of insects. Around 9 pm migrating birds start rising mixing in with insects in the same resolution volume. By 11 pm migrating birds become dominant scatterers cloaking the insect returns.

Precipitation-free air returns are contaminated by the returns of biological scatterers of (1) different types and (2) unevenly mixed throughout the scanned region. The population of the biological content of the data changes over the observation time. The phenomena can be explained as a progression of the biological scatterers schedule throughout the evening – ascending, migrating, feeding, descending, etc. Different activities of the biological scatterers impose particular change in radar echoes.

## **5. Spectral Analyses**

This section provides a short review and demonstrates benefits of traditional nonparametric spectral analyses. The section describes how to estimate spectrum. Examples of individual spectra are presented next, and the differences between spectral densities corresponding to the two species are pointed out. These are followed by a discussion of the signal-to-noise ratio and its alternative, spectral-peak-power-to-noise-level ratio. Spectral field as a useful visual tool is presented. An example of spectral fields with two distinguishable scatterer types is used to evaluate the polarimetric properties of scatterers from a chosen section of spectral coefficients and to recover wind velocity. Examples of this section are presented on the 11 pm case at azimuth  $180^\circ$  (Section 4.2).

### **5.1. Spectral Processing**

A complex voltage from scatterers in a resolution volume consists of 128 of I-Q samples (Section 4.1). The mean, or DC component, is computed for I and Q portions of the sequence. The corrected voltage is obtained by subtracting the DC component from the corresponding sequence. An example of a corrected in-phase portion of a received signal is shown in Figure 5.1. The original and corrected for DC sequences are shown with dashed and solid lines, respectively. The corrected for DC sequence is weighted by a non-rectangular window function to reduce coupling of strong spectral components into adjacent weaker ones. A raised cosine, or Von Hann (Hanning) window is given by (Doviak and Zrnić 1993)

$$w(m) = 0.5 + 0.5 \cos \left[ \left( m - \frac{M-1}{2} \right) \frac{2\pi}{M} \right], \quad (5.1)$$

where  $M$  is the size of the window. Power spectral density is computed using Fourier transformation on the time-series data weighted with the Von Hann window (Section 2.4, equation 2.3).

In general, if scatterers are moving at a certain speed, the power spectral density (PSD) has a peak centered at the corresponding Doppler velocity. Examples presented in Figure 5.2a and 5.2b show PSD for a resolution volume in horizontal and vertical channels respectively. These spectra are from a resolution volume at 30 km range,  $180^\circ$  azimuth and  $0.5^\circ$  elevation ( $SNR_h = 42$  dB;  $SNR_v = 35$  dB). Spectra in both channels show two peaks caused by scatterer types mixed in the resolution volume and moving with different radial velocities. Examples demonstrate strong peak at about  $10 \text{ m s}^{-1}$  evident in both the H and V channels. The additional hump at about  $20 \text{ m s}^{-1}$  in the horizontally polarized return is better defined. The peaks at lower velocities ( $\sim 10 \text{ m s}^{-1}$ ) are due to weak flying insects and the ones at higher velocities are from migrating birds. We deduced this from analyses of atmospheric sounding and continuity of spectral peaks in range. The atmospheric sounding indicates calm winds at low elevation (Figure 4.2b). The continuity of spectral peaks in range is discussed in Section 5.3.

The Doppler velocity location of the spectral peak varies depending on the radar beam position. The Doppler velocity peak is at zero velocity when the radar beam is

perpendicular to the scatterers' direction. Consequently, for a uniform wind, the radial velocity as a function of azimuth resembles a sinusoid.

Often the Doppler spectrum has a peak at zero velocity, even if the radar beam is not pointing perpendicular to the scatterers' direction. This peak can be caused by the ground clutter returns from buildings, trees, hills due to topographical features of the area. Filtering of the ground clutter returns is accomplished by notching and interpolating the corresponding spectral coefficients (Section 2.5). An example of such filtering is shown in Figure 5.3. Dashed line shows spectrum with a maximum at zero velocity corresponding to ground clutter return. Solid line shows performed correction. The effect of clutter correction on PPI (Figure 4.4) is significant.

## **5.2. Low Signal to Noise Ratio**

Clear air echoes are generally weak. Examples of the echo power along a radial in the evening (8 pm) and at night (11 pm) are presented in Figure 5.4a and Figure 5.4b, respectively. Both examples show echo power along the radial at azimuth  $180^\circ$  for elevation angles  $0.5^\circ$  and  $6^\circ$ . Dashed line shows signals power at elevation  $0.5^\circ$ . The echo powers at elevation  $0.5^\circ$  in both examples demonstrate similarities in shape for ranges below 30 km. The reason for such resemblance is the ground clutter residuals. For example, the especially large peak (about 50 dB above noise and about 30 dB above clear air signal) at 27 km is caused by the elevated grass land between Canadian River and Walnut Creek. A sketch (Figure 5.5) provides constructive information helpful for evaluation of the clutter height and insight on why this clutter

is not filtered. The KOUN radar is located at 357 m above sea level (ASL). The Canadian river ground level is about 20 meters lower and the Walnut Creek ground level is about 30 meters lower than the radar level, schematically shown with a dashed line in Figure 5.5. The open grass, range land situated between the rivers has small hills up to 40 meters above the radar ground level. Presumably there are both insects and birds above these hills. The echoes from the “occupied” hills are superposed to form large return appearing as a wide peak in Figure 5.4 at the 27 km range. The returns from such extended, however insignificant in height, ground clutter completely overwhelm the weak clear air echoes. The same might be true for the returns at ranges less than 30 km. On the other hand, at ranges beyond 30 km clutter does not obstruct the weak signal due to elevation of the radar beam. At ranges beyond 30 km and at elevation  $0.5^\circ$  the 8 pm example (Figure 5.4a) demonstrates a weak clear air signal. The 11 pm example (Figure 5.4b) shows stronger signal power. The signal at 8 pm is very weak because of the decrease of scatterers in the atmosphere due to a transition from day to night occurring at the sunset. Actually, the transition is the period of time when the diurnal insects have already descended but nocturnal have not raised yet. The signal at 11 pm is stronger and can be attributed to birds and insects mixed in the precipitation-free atmosphere. At higher elevation and at far ranges the power curves converge to -58 dB. This marks the noise level. The SNR can be easily estimated as difference of the signal power and -58 dB. The SNR at ranges beyond 30 km is less than 15 dB for the 8 pm example, and is less than 30 dB for the 11 pm case. Overall, the SNR values are rather small.

### 5.3. Spectral Field

Define *spectral field* as an image that is constructed from consecutive Doppler spectra along a radial so that one axis represents range, another axis represents Doppler velocity, and color scale characterizes signal power. In other words, spectral field displays Doppler spectra of a radial stacked in range. With the help of spectral fields the number of dominant motions in a resolution volume can be identified; the velocities can be tracked along the radial and the origin of the velocities can be envisaged. The spectral field format promotes easier visual interpretation. Hypothetically, spectral field of clear air should show a continuous band of velocities corresponding to the wind velocity. Additional bands or blobs when present exemplify contaminants, e.g., insects, birds, airplanes, etc.

Examples of the Doppler spectral fields are presented in Figure 5.6. Color scale shows the power in logarithmic units. Vertical axis shows negative and positive velocities which represent the motion of the scatterers toward and away from the radar respectively. The  $S_h$  spectral fields at 11 pm in azimuth  $180^\circ$  pm for two elevation angles  $2.5^\circ$  and  $0.5^\circ$  are shown in Figure 5.6a and 5.6b respectively. Figure 5.6c presents  $S_h$  spectral fields at elevation  $0.5^\circ$  in the additional V channel (Section 5.5). I observe 2 broad though distinctive bands in the spectral fields with powers 30 dB more than background and approximate velocities  $-10 \text{ m s}^{-1}$  and  $-20 \text{ m s}^{-1}$ . One band is continuous; appears brighter; starts from the radar and dissipates at far ranges. Another band is sporadic and blotchy; it starts at some distance from the radar and follows the silhouette of the first band. The continuous band centered at about  $v_a/3 =$

$10 \text{ m s}^{-1}$  is present at all five elevations of the scan. This band corresponds to the radial velocity of the weak flying insects carried by the wind. The sporadic band breaks up on segments and blobs at higher elevations and is due to migrating birds. Each blob is either a single large bird or a cluster of a few birds migrating in a flock. The blobs with birds are separated by the regions void of birds.

#### **5.4. Spectral peak power to noise level ratio**

The spectral peak power to noise level ratio can be estimated from the spectral field. The spectral field image can be partitioned on signal and noise sections. Consequently, for the spectral fields of Figure 5.6b, part of the image with negative velocities contains noise and part of the image with positive velocities mostly contains signal. Further, velocities with absolute values below  $2 \text{ m s}^{-1}$  are not considered for the presented radial because of possible ground clutter contamination due to interpolation in clutter filtering. The maximum of the signal part is the peak power; and the mean of the noise part is the noise level. Figure 5.7 shows the peak power and noise level for the radial, presented in Figure 5.6b. The noise floor, shown with a dashed line, is approximately constant at -41 dB. The peak power, shown with a solid line, is decreasing linearly with range. The peak power to noise level ratio, indicated by a solid line with a dot marker, is above 20 dB for the ranges up to 80 km. At ranges from 5 km to 30 km the SNR values are between 20 and 60 dB and the signal powers are not saturated by clutter. Even at the range of 27 km, where the combined contribution from several hills between the 2 rivers severely contaminates

the radar returns, the SNR is 20 dB. The spectral peak power to noise level ratio is an excellent estimator for the weak clear air signals, that will be used instead of conventional SNR discussed in Section 5.2 for censoring data and setting threshold values.

### **5.5. Dual Polarization Spectral Field**

For the dual polarimetric radar data H and V spectra can be constructed for each resolution volume (Figure 5.2a and 5.2b). Accordingly, there are two spectral fields for each radial. The spectral fields of echoes from horizontally and vertically polarized waves are shown Figure 5.6b and 5.6c. These spectral fields are from echoes at 11 pm, elevation  $0.5^\circ$ , and azimuth  $180^\circ$ . The blotchy band emerging around  $-20 \text{ m s}^{-1}$  in spectral fields appears similar in both channels. However, the continuous band, centered at  $-10 \text{ m s}^{-1}$ , exhibit a significant difference exceeding in power 5 dB between the channels. Consequently, the polarimetric values of the portions of spectra containing the described bands will be different.

Hypothetically, if scatterers mixed in a resolution volume exhibit different radial velocities and, therefore, are separated in spectra, than their type can be identified by the polarimetric features of spectral coefficients responsible for the returns. Chosen portions of spectral coefficients, corresponding to the radial velocities of the scatterers of interest, will provide necessary polarimetric information to recognize the scatterer type and to avoid the contribution of contaminants.

## 5.6. Choice of spectral coefficients

An approach using portions of spectral coefficients for distinguishing scatterers separated in spectra but mixed in the resolution volume, is accentuated in Figure 5.8. Assume that the spectral field in each channel contains a continuous velocity band and another band of blotchy paths or blobs. The blobs are contaminants that need to be recognized and filtered; otherwise they can cause errors in the mean velocity estimates. Doppler spectrum at some range  $A$  in each horizontal (Figure 5.8c) and vertical (Figure 5.8d) channel is expected to have 2 peaks. The corresponding peaks locations (in Doppler velocity) are similar. However, the powers and spectral widths of the peaks are different because of the scattering properties and body shapes of the scatterers. In Figure 5.8c and 5.8d the dashed-dotted and dashed rectangles enclose spectral coefficients around the suspected peaks. Polarimetric variables computed only from the spectral coefficient enclosed in a dashed rectangle most likely carry features of the insects. Suppose, the polarimetric variables computed for the spectral coefficient enclosed in the dash-dotted rectangle yield the scatterers as migrating birds. In a simple case the band in spectral field occupies a narrow window of velocities and does not wave out of the window. For a more complicated case the wind band can be tracked in the spectral field, and then a narrow window of velocities should be positioned on the track and used for computation of the mean wind velocity. If tracking can not be accomplished then every block of spectra needs to be questioned for the position (Doppler velocity) of stand alone additional peaks (high powers) and then filtered. Doppler spectra at the two polarizations can be compared,

and polarimetric variables can be computed from contiguous spectral coefficients. The differences between the scattering properties of birds and insects can be resolved in the spectral domain and used in distinguishing between wind/insects and birds.

The polarimetric variables can be computed from the chosen portions of complex spectral coefficients at the two polarizations. Spectral coefficients for computing the differential reflectivity (or other polarimetric variables) can be adaptively selected according to the SNR, or other criteria such as applying a window over a band of velocities.

The described technique can be easily applied to the presented radial (11 pm, elevation  $0.5^\circ$ , azimuth  $180^\circ$ ) because the velocity bands are well separated and the magnitude of velocity does not significantly change with range (height). The part of the spectral field containing signal is shown in Figure 5.9. The rectangle drawn with a solid line encloses contributions with radial velocities from  $3 \text{ m s}^{-1}$  to  $13 \text{ m s}^{-1}$ . These scatterers are most likely insect. The rectangle drawn with a dashed line encloses contributions with radial velocities from  $15 \text{ m s}^{-1}$  to  $26 \text{ m s}^{-1}$ , which are assumed to be migrating birds. The  $Z_{DR}$  values computed for this radial are shown in Figure 5.10a. The dotted curve corresponds to the mean  $Z_{DR}$ , in other words,  $Z_{DR}$  computed with the maximum window (e.g., all values of spectral coefficients between  $-35$  and  $35 \text{ m s}^{-1}$  are included). The solid and dashed lines correspond to the  $Z_{DR}$  computed with the window retaining the signal power of presumed insects and birds, respectively. Likewise windows are used for the copolar correlation coefficient  $\rho_{hv}$  computations (Figure 5.10b).

Generally, it is hard to distinguish the curves at close ranges due to the ground clutter contamination and at far ranges due to low SNR. Nonetheless, separation is clear along most of the radial. In fact, birds and insects have about 5 dB difference in mean  $Z_{DR}$  at ranges between 30 km and 60 km (this azimuth). The histograms of the  $Z_{DR}$ ,  $\rho_{hv}$  and  $\delta$  of the presented radial (Figure 5.11), computed for ranges from 10 to 70 km expose the distinct separation. No doubt that the favorable geometry whereby the beam is pointed in the wind direction tremendously enhances this separation in the spectral densities of the polarimetric variables.

Positioning of the window is not trivial if the wind is changing along a radial, or if its direction is oblique to the beam. The polarimetric variable values heavily depend on the window location and width. The recovered wind velocity is shown in Figure 5.12. The streaks can be corrected using velocity azimuth display (VAD) analyses. Birds and insects are not evenly mixed in the scanned area. The maximum powers in the bands (Figure 5.9) can be estimated from the spectral peaks. Power in spectral coefficients of the bird and insect band depicted in Figure 5.13 indicates that in this direction (South) from the radar returns from insects dominate at ranges up to 20 km and the returns from birds dominate at ranges from 50 to 80 km (0.5 km to 1.1 km in height). The return power in the insect band decreases with range with  $R^{-2}$  (i.e., volume is uniformly filled with insects), while the power in the bird band has a peak at about 60 km (about 0.8 km in height) indicating that birds tend to form a layer.

## **6. Spectral Polarimetric Analyses**

The benefits of spectral analyses exposed in chapter 5 instigated formulation of a conceptually new approach for the polarimetric variable computations. This section starts with a description of the computations done to obtain the spectral density of polarimetric variables. Subsequent examples with novel polarimetric spectral densities are presented. The VAD technique is expanded into novel SVAD (spectral VAD) approach using the concept of polarimetric spectral densities. The section provides examples of the SVADs computed for different number of ranges and gives an example of recovered wind velocity. The section concludes with a discussion about a preferred polarimetric variable for the SVAD estimation.

### **6.1. Spectral densities of polarimetric variables**

It was shown in previous chapter that the values of polarimetric variables computed for the different section of multimodal spectra can be used for distinguishing mixed species in the resolution volume if the species have different polarimetric properties. The sequence of spectral coefficients of a bimodal spectrum has two peaks, each with the significant powers at a corresponding velocity value. Two windows can be positioned on the peaks covering the latter and the surrounding coefficients. Figure 6.1 recollects how the window positions are chosen: the arrangement of the two peaks and the valley between them are located; and the width of the windows is estimated to guarantee that the windows contain the spectral coefficients with significant powers. Doppler spectra at the two polarizations can be

compared, and polarimetric variables can be computed from contiguous complex spectral coefficients. The differential reflectivity, the differential phase and the copolar correlation coefficient are computed according to equations (2.9), (2.11), and (2.12) respectively. Choosing a correct window location is imperative and greatly affects the values of consequent polarimetric variables. To investigate the contribution of spectral coefficients to the resulting value of polarimetric variable I consider the smallest possible window. I compute polarimetric variables for every pair of spectral coefficients whenever possible and for the three point running averages of spectral coefficients otherwise. Thus obtained values denote the spectral densities of polarimetric variables. There is no universally accepted definition for spectral densities of polarimetric variables. Researchers have defined and used a spectral covariance matrix (Unal and Moisseev 2004), used spectral density of differential reflectivity,  $Z_{DR}$  (Yanovsky et al. 2005, Kezys et al. 1993) and spectral density of differential phase (Unal and Moisseev 2004, Kezys et al. 1993). In a dual polarization system two spectral densities are available, at H and V polarizations; from these it is possible to estimate the differential properties at localized resolved Doppler shifts.

For  $M$  transmitted pulses there are  $M$  spectral coefficients in the spectra from a resolution volume. Let  $k$  be an ordered number of spectral (Fourier) coefficient that takes values from 1 to  $M$ ;  $k$  can be transformed to corresponding radial velocity in the unambiguous velocity interval from  $-v_a$  to  $v_a$ . Then,  $s_h(k)$  and  $s_v(k)$  is an H-V pair of complex spectral coefficients containing both the signal and the noise from the

corresponding channels (Figure 6.2). To obtain spectral densities of differential reflectivity the  $Z_{DR}$  values are computed for every H-V pair of spectral coefficients of the power spectral densities (Kezys et al. 1993, Yanovsky et al. 2005) according to

$$Z_{DR}(k) = 10 \log_{10} \frac{|s_h(k)|^2}{|s_v(k)|^2} + C, \quad (6.1)$$

where  $C$  is the calibration constant which accounts for the difference in the system gains of the two channels. For the spectral data presented here  $C = -2.9$  dB and is estimated by comparing the values obtained at the same time and with the KOUN radar but with two different receivers, as described in appendix A.

I estimate the spectral densities of the complex copolar correlation coefficient (magnitude and phase) from a running 3 point average on contiguous complex spectral coefficients of the H and V channels (Figure 6.3). The spectral density of the copolar correlation coefficient is computed according to

$$\rho_{hv}(k) = \frac{\sum_{m=\langle k-1 \rangle_M}^{\langle k+1 \rangle_M} s_h(m) s_v^*(m)}{\sqrt{\sum_{m=\langle k-1 \rangle_M}^{\langle k+1 \rangle_M} |s_h(m)|^2 \sum_{m=\langle k-1 \rangle_M}^{\langle k+1 \rangle_M} |s_v(m)|^2}}, \quad (6.2)$$

where  $\langle n \rangle_M$  stands for  $n \bmod(M)$ , needed to perform operation circularly. The 3 point average is chosen to preserve good spectral resolution, comparable to the resolution of the other spectral densities. Maximum spectral resolution could be achieved with a 2 point running average, which however would center the spectral estimate in-between the adjacent coefficients.

The spectral density of the scatterers' differential phase  $\Phi_{DP}$  is computed relative to the system phase  $SysPhase$  as

$$\Phi_{DP}(k) = -\arg[\rho_{hv}(k)] \times 180/\pi + SysPhase (^\circ). \quad (6.3)$$

The system phase of the KOUN digital receiver is estimated from the ground clutter reflectivity returns (Zrnić et al. 2005) to be  $168^\circ$ . The estimation procedure is summarized in Appendix B. In the data presented there was no precipitation along the propagation path and the phase (Equation 6.3) is caused by the differential shift upon backscattering,  $\delta(k)$ , i.e.,  $\delta(k) = \Phi_{DP}(k)$ . Insects might introduce a small propagation phase shift but I neglect it. Similar to the widely accepted abbreviation of power spectral density PSD, I use  $Z_{DR}SD$ ,  $\rho_{hv}SD$  and  $\delta SD$  to abbreviate spectral densities of corresponding polarimetric variables.

## 6.2. Example of the spectral densities of polarimetric variables

Spectral densities of polarimetric variables along the presented radial (11 pm, elevation  $0.5^\circ$ , azimuth  $180^\circ$ ) are shown in Figure 6.4. Only one of the two bands evident in power spectral fields (Figure 5.8) is apparent in the spectral fields of polarimetric variables. The band located at smaller velocities and caused by insects. The bird band is masked by noise in the polarimetric spectral density fields. The insect band is vivid and exhibits  $Z_{DR}$  values between 3 dB and 10 dB in,  $\rho_{hv}$  in the range 0.7 to 1.0, and  $\delta$  in the range  $60^\circ$  to  $80^\circ$ . Streaks at ranges 0 to 10 km are due to the ground clutter returns. The insect band in  $Z_{DR}SD$  and  $\rho_{hv}SD$  fields dissipates

beyond the 70 km range due to small SNR. The  $\delta$ SD on the contrary, stretches along the whole radial.

The spectral coefficients caused by birds in the PSDs shown in Figures 5.2 and 5.8 exhibit powers well above noise. That means that the polarimetric properties of the bird' spectral coefficients can be estimated if the noise is removed. Spectral densities of polarimetric variables along the same radial (11 pm, elevation  $0.5^\circ$ , azimuth  $180^\circ$ ) with powers exceeding noise level are shown in Figure 6.5. Two bands become apparent in all three shown spectral fields. The presented radial is directed south at  $180^\circ$ , while the wind blows toward south-west at about  $225^\circ$ . The radial shows two bands well separated in the Doppler velocity. However, the separation is not as clear in all radials. The nature of radial velocity dictates that maximum velocity is located at the azimuth parallel to the direction of flow and zero velocity is found at the azimuth perpendicular to the flow (sinusoid in VAD). Hypothetically, when there are two mean flows with different headings (one flow is shifted in azimuth with respect to the other flow) then there will be azimuths in which the flows will appear as moving at the same radial velocity to the radar (intersection of the two sinusoids). The separation of insect and bird bands at such azimuths is challenging. The velocities at the azimuths where the separation of the two bands is tougher can be estimated from the VAD sinusoids. The VAD sinusoids are discussed in section 6.3.

The  $\delta$ SD in the radial at azimuth  $180^\circ$  (Figure 6.5c) displays two bands: a vivid broad band at approximately  $10 \text{ m s}^{-1}$  of about  $68^\circ$ , and a less distinct narrow band located around  $20 \text{ m s}^{-1}$  displaying erratic phases. The  $\rho_{hv}$ SD values are slightly

larger in the insect band compared to the bird band. The  $\delta$ SD in the insect band displays larger values. The histograms of spectral polarimetric variables in the selected bands are shown in Figure 6.6. The results for insects and birds are indicated by a line without marker and a line with a dot marker, respectively. The part of spectral field designated as birds demonstrates very broad distribution of  $\delta$  and a concentrated distribution of  $Z_{DR}$ . The part of spectral field designated as insects shows compact distributions of both  $Z_{DR}$  and  $\delta$ . The mean of  $Z_{DR}$  for insect is larger than that for birds by about 7 dB. The  $\delta$  values for insects span over a narrow number of frequencies with a crest at  $68^\circ$  (this radial). The  $\rho_{hv}$  of insects shows larger values with most occurrences close to 1. On the other hand, the  $\rho_{hv}$  of birds is distributed over a larger interval with more occurrences between of  $\rho_{hv}$  between 0.7 and 1, and with a maximum at 0.95. The histograms show that polarimetric spectral fields can discriminate types of scatterers in the radial that exhibits a good separation in velocity. Even though the histograms of polarimetric spectral fields overlap the offsets are obvious and the mean values of the distributions differ. The discrimination might be a challenge in radials with less obvious separation in velocity than in the presented radial. The events in the selected bands are representative because they have most power.

### **6.3. Two-dimensional histogram**

There is, perhaps, a more visually pleasing way to discriminate types of scatterers. The 2D histograms of spectral polarimetric densities in the radial are

submitted in Figure 6.7, 6.8, and 6.9. The histograms are computed for every resolved Doppler shift (spectral coefficient) to capture the polarimetric properties of all present scatterers in a radial at ranges 10 to 70 km. The histograms confirm that at least two scatterer types are present in the scanned region and clarify the diversity of distributions corresponding to these scatterers' polarimetric spectral returns.

The 2D histogram of the  $\delta\text{SD}$  (Figure 6.7) shows a cluster of scatterers with backscatter differential phase of about  $70^\circ$ , concentrated at velocity of about  $7 \text{ m s}^{-1}$ . A wide band in the 2D histogram is evident at about  $21 \text{ m s}^{-1}$  with the phases spread from  $-180^\circ$  to  $180^\circ$ . There are also scatterers with positive phases and velocities close to zero. The 2D histogram of the  $Z_{DR}\text{SD}$  (Figure 6.8) shows an odd shaped squiggle with a confined cluster for insects and a spread in Doppler velocity and in  $Z_{DR}$  region for birds. The brightest curve on the squiggle also emerges at  $7 \text{ m s}^{-1}$  with more than 5 dB  $Z_{DR}$ . The 2D histogram of the  $\rho_{hv}\text{SD}$  (Figure 6.9) shows a blob at  $7 \text{ m s}^{-1}$  with values close to 1. A wide band of scatterers with smaller values of  $\rho_{hv}$  emerges around  $20 \text{ m s}^{-1}$ . The spectral coefficient due to wind carried insects produce blobs at  $7 \text{ m s}^{-1}$  in all 2D histograms of polarimetric densities in the presented radial. These 2D histograms are used to evaluate the constituents of the resolution volumes in Section 7.3. The differential phase value of insects (blob in Figure 6.7) in the presented radial is almost  $30^\circ$  larger than the value  $40^\circ$  that was previously reported by Zrnić and Ryzhkov (1998). This inconsistency is discussed in Appendix B.

## 6.4. Spectral VAD

Herein the spectral densities are presented in the VAD format; for short abbreviated as SVAD. The azimuth angle is along the abscissa, the velocities (spectral coefficients) are along the ordinate, and the intensity coded spectral values are depicted with color. To construct SVADs spectral fields are computed for all 360° of the scan. Thus the SVAD technique provides distributions of the polarimetric variables in the azimuth and velocity space.

Zhang et al. (2005) examined Doppler moment and polarimetric variables and reported azimuth dependence; they investigated the mean values of polarimetric variables, in other words, one parameter per resolution volume. The spectral polarimetric density exposes the velocity content of the parameter instead of its mean value. Different spectral portions of the parameter might enjoy different characteristics in azimuth. A special spectral azimuth display offers means to observe changes in spectral content of a parameter as a function of azimuth.

To construct the spectral velocity azimuth display, spectra are computed for radials (typically 360°) of the scan, and averaged over a fixed range interval at each radial. The mean spectral density (over a fixed range interval) as a function of azimuth is presented in Figure 6.10. For a vivid visual effect I chose ranges from 30 to 70 km (from 0.2 km to 1 km in height) for the SVAD computation thus avoiding contamination by ground clutter and noise. Each spectral coefficient at a fixed azimuth is a median of 120 spectra (between 30 and 70 km). In the  $S_h$ SVAD (Figure 6.10a) two traces are clearly seen and both have sinusoidal shapes. The two sinusoids

indicate  $12 \text{ m s}^{-1}$  from North-East to South-West; and  $20 \text{ m s}^{-1}$  from North to South. In the  $Z_{DR}$ SVAD (Figure 6.10b) the sinusoid with smaller amplitude appears bright and well defined with 5 to 8 dB values corresponding to the insect returns. The sinusoid with larger amplitude exhibits smaller  $Z_{DR}$  values and has discontinuities in azimuth. This sinusoid is due to returns from birds (Figure 6.11). At the directions ( $240^\circ$  to  $260^\circ$  and  $60^\circ$  to  $80^\circ$ ) where the two sinusoids intersect the  $Z_{DR}$  decreases due to bird presence but it is still within the values for insects. The maxima of  $Z_{DR}$  (not shown) as function of azimuth are between 3 and 8 dB for insects and are less than about 2.5 dB for birds. These are consistent with previous measurements (Zrnić and Ryzhkov 1998). Further the maximum values for insects occur in the direction of the wind similar to observations by Zhang (2005) who suggest that the strong difference between  $Z_{DR}$  along the wind direction and perpendicular to it is caused by the presence of large insects (moths and locusts) which can fly at speed of 3 to 5 m/s. Although the large averaging interval produces very pleasing plots it comes at a reduced resolution in height.

## **6.5. Number of ranges to average for the SVAD**

Averaging over a large number of ranges might complicate spectral VAD due to incorporation of scatterers possibly separated in height and range, although it gives overall a grand picture of the ongoing movements. Decreasing number of ranges for averaging allows avoiding such complication at the expense of larger uncertainty in the histograms which causes poor contrast.

Figures 6.12, 6.13, and 6.14 demonstrate how averaging along different number of range locations affect the clarity of SVAD. Figure 6.12 shows SVAD ensemble ( $S_h$ ,  $Z_{DR}$ ,  $\rho_{hv}$ , and  $\delta$ ) for one range location at 30 km. Only values above the noise level are displayed. A sinusoidal trace with a broad spectrum width (up to  $20 \text{ m s}^{-1}$ ) demonstrates the severe contamination by birds. Averaging over 4 ranges produces more appealing results. The SVAD images Figure 6.13 display median spectral densities from the range interval from 30 to 31 km (4 range locations). This example exhibits more defined structure of each of the two visible sinusoids. Increasing the number of ranges to 20 (5 km) further improves the sinusoid's shapes and clarity in the presented case. In Figure 6.14 the contribution from the birds are almost completely removed. Thus, for obtaining vertical profiles of wind I present (and use) median spectral densities from the range interval of 30 to 35 km. Both the  $\rho_{hv}$ SVAD and the  $\delta$ SVAD (Figures 6.14c and 6.14d) depict well the sinusoidal shape corresponding to insect returns. With increasing height the depiction is poorer but visible.

Clarity of the polarimetric spectral VAD depends on number of range locations used for estimation. In the case of only one range location (250 m resolution) the sinusoids are intermingled and fuzzy. The sinusoids are easy to perceive in both cases when averaging is performed over 4 range locations (1 km) and 20 range locations (5 km). The cases with averaging perform well due to the nature of the bird distribution in the space. Birds usually do not fill the radial in somewhat uniform or continuous manner, even though their echoes might have larger powers than the insect echoes.

The bird echoes appear granular, spotty. The spectral components corresponding to birds differ vividly from range to range, sometimes growing above the insect spectral peak and at other times diminishing to the noise level. Power threshold at the noise level and median over contiguous ranges provide an effective way for diminishing the contribution from the spectral coefficients of the exceptional peaks.

## **6.6. VAD from SVAD**

The VAD technique has been used to determine several features of the wind field: aerial average wind speed, direction, divergence and deformation. The zeroth harmonic of the VAD provides the horizontal divergence. The first harmonic of the VAD gives the average wind speed and direction. The resultant deformation and orientation of the axis of dilatation can be found from the second harmonic.

Estimation of insect velocities can be achieved using the SVAD. Application of thresholds on the polarimetric variables in the SVAD can eradicate contributions from scatterers with different polarimetric signatures. In some cases (or aspect angles) diverse scatterers might have similar polarimetric signatures and thus would be hard to separate. Because there are four SVADs (one for each polarimetric variable) it follows that a combined use of these would facilitate better separation of scatterers than what is possible from a single SVAD. The sinusoids in Figure 6.10 and 6.11 intersect at about  $60^\circ$  and at  $240^\circ$  challenging separation attempts at these azimuths. Therefore the velocity values estimated from such SVADs might have gaps. Such gaps are due to uncertainty caused by mixing of the polarimetric values at the

intersection of scatterer bands (sinusoids), or by changes associated with different aspect angles. The suitable VAD technique (Rabin and Zrnić 1979) for such data with gaps is part of a suite of algorithms on the WSR-88D. The technique is based on the assumption that the power of higher harmonics can be neglected and the zeroth and first harmonic are obtained from the least squares fit.

The example presented in Figure 6.15 shows VAD deduced from SVADs of differential reflectivity at ranges from 30 to 35 km. Thresholds are applied simultaneously to all polarimetric spectral densities as follows. Adaptive threshold is applied to the field of differential reflectivity to remove all spectral coefficients with  $Z_{DR}$  below half the maximum of the median value at the specified velocity bin. All spectral coefficients having the copolar correlation coefficient below 0.7 are discarded. Median filter over 3 range locations and 6 spectral coefficients (on each polarimetric spectral density) is applied. All spectral coefficients corresponding to the  $Z_{DR}$  values below 2 dB are removed. 2 dB is the largest differential reflectivity previously measured from birds (Zrnić and Ryzhkov 1998, Mueller 1983). After the thresholds have been applied I take the maximum of the differential reflectivity in the spectrum at each azimuth and use the least squares fit described by Rabin and Zrnić (1979) to generate the wind speed and direction. The cross marker indicates the recorded velocities (Figure 6.15c). The solid line shows the estimated velocity from the harmonic least square fit. From the VAD, the directions and velocities of insects (hence wind) are deduced. The SVAD analysis has been applied to all the data at  $0.5^\circ$  elevation using the same procedure as for Figure 6.15; but, it is a running SVAD

incrementing at 250 m intervals. The resulting field is depicted in Figure 6.16b. It is much smoother than the original and the large velocities are gone. Further, the decrease of velocities between 50 and 80 km is evident and the higher values at closer range hint that a low level jet might be present. The VAD deduced from SVAD for the higher elevations are shown in Figure 6.17. Wind velocity and direction points derived from these are indicated in Figure 6.18 with a cross marker. The time of radar measurements is 04 UT and the VAD deduced speeds and directions agree better with the rawinsonde observations at 0 UT. The difference in wind velocity might be due to the onset of the low level jet at night or the dominant insects might be active flyers.

### **6.7. Speculations about censoring with $\rho_{hv}$**

By examining the PPIs of  $\rho_{hv}$ , power and velocity, one can notice that the high  $\rho_{hv}$  values correspond not only to the locations with significant returns in power but also to the other locations with insignificant powers but with consistent (non-noisy) velocity fields. Hypothetically, the  $\rho_{hv}$  can be used alone or in combination with the power to threshold or censor unreliable returns. To examine the potential of  $\rho_{hv}$  values for the censoring arrangement I refer to an uncensored PPIs of  $Z_h \rho_{hv}$  at  $6^\circ$  elevation (Figure 6.19a and 6.19b). In this context uncensored means that the insignificant returns, such as noise, are included in analyses. I take resolution volumes at all azimuths at a fixed range and compute its histogram of  $\rho_{hv}$ . I repeat this for all ranges of the PPI and plot the result as a 2D histogram with range and  $\rho_{hv}$  in

the axes (Figure 6.19c). Horizontal axis shows the values of the copolar correlation coefficient. Vertical axis shows range from the radar (top of the image) to 117 km (bottom of the image). Obviously, because of high radar beam elevation, the significant returns are at close ranges and the noise is at far ranges (beyond 30 km). The  $\rho_{hv}$  of noise shows a distribution with a peak at about 0.15. The  $\rho_{hv}$  of significant returns indicates values larger than 0.5 with most occurrences above 0.7. This example demonstrates that the  $\rho_{hv}$  of noise and signal are extensively different. This fact gives an option to use  $\rho_{hv}$  as a threshold instead or in a combination with the power threshold (Ryzhkov et al. 2005).

Similar effect can be observed in the  $\rho_{hv}$  spectral density. Although the 2D histograms of the  $\rho_{hv}$  in Figure 6.9 show only a distribution at a constant range, the signal portion of spectral densities appears to have larger values of  $\rho_{hv}$ . Consequently, application of the combination power and  $\rho_{hv}$  thresholds on spectral densities can enhance the clarity of the spectral density. This simplifies the identification task and polarimetric distributions in velocities produce sharp and definite SVADs. The polarimetric spectral densities exhibit diverse and perceivable features even at low SNR conditions.

## **6.8. Preferable parameters for scatterer discrimination**

In the presented examples the differential reflectivity appears to be a good discriminator of the scatterer types. However, the squiggle in the histogram shown in Figure 6.8 clearly exposes that some scatterers with large velocities do exhibit large

differential reflectivity values. The differential phase helps to resolve this uncertainty. The blob on the histogram of differential phase density (Figure 6.7) is definite and credible. The change of distributions of polarimetric densities in time is investigated in Chapter 7, and shows some advantages of the backscatter differential phase compared to the other polarimetric parameters. The best discriminator, however, is the ensemble of all polarimetric parameters.

## **7. Intrinsic polarimetric values of biological scatterers**

This section contains analyses of the signals acquired during transition between diurnal and nocturnal types of scatterers. The 2D histograms of velocity and polarimetric variable are constructed for sectors in range and azimuth to reduce statistical uncertainty. An ensemble of such 2D histograms is used to assess the occurrence of scatterers moving at a certain velocity and exhibiting certain polarimetric properties. The differences in the intrinsic values of polarimetric variables for diurnal and nocturnal types of scatterers are noteworthy. The mean flows of different scatterer types are deduced from the clusters with large occurrences and similar polarimetric properties. The marginal distributions for two dominant types of diurnal and two dominant types of nocturnal scatterers are obtained. These distributions yield significant new insights into the composite VADs, corresponding PPIs and mean values of polarimetric variables. A novel three dimensional azimuthal spectral histogram 3DASH is presented as a visualization tool for viewing the ensemble of 2D histograms. 3DASH displays polarimetric properties and velocity distributions as a function of azimuth of the contributing scatterers. Transparency is used to censor small occurrences and expose the dominant scatterers' polarimetric, azimuthal, and velocity signature. The advantages of spectral density of backscatter differential phase to other polarimetric spectral densities are discussed.

## 7.1. Polarimetric spectral densities in one radial

Six cases of echoes are chosen for the investigation. The collection times of these cases can be approximated as the top of each hour from 6 pm to 11 pm local time (Section 4.2). The PPIs of polarimetric variables computed using standard processing technique (Doviak and Zrnić 1993) with no censoring whatsoever are shown in Figure 7.1. Because clear air echoes are generally weak the standard censoring techniques might result in very sparsely filled radar displays. The portion of the trustworthy echoes can be assessed not from the powers, but rather from the high values of the  $\rho_{hv}$  (Section 6.6).

The PPIs are expected to show polarimetric properties of the contributing echoes. A biological scatterer has a characteristic shape. A change in the angle between the propagation direction and the axis of scatterer is anticipated to produce a gradual change in the corresponding polarimetric value. The dependence in azimuth is expected to be systematic and to have some symmetry. However, the PPIs display bizarre shapes and irregular patterns. The PPIs indicate that the dominant scatterers at 6 pm descend by 8 pm and get replaced by a different type(s) of scatterers. The symmetry of  $Z_{DR}$  on the PPI is apparent at 6, 7 and 8 pm. The symmetry in PPIs of all polarimetric variables at 8 pm is remarkable. All PPIs display unforeseen values, bizarre patterns, and velocities exceeding  $25 \text{ m s}^{-1}$  at 9, 10 and 11 pm. However, the rawinsonde measured calm winds below  $12 \text{ m s}^{-1}$  at low altitudes (Figure 4.2). The disagreement between the atmospheric sounding and radar returns is large. I seek an

explanation for the peculiar shapes and unrealistic values of moments and polarimetric variables in the PPIs by examining the polarimetric spectral densities.

Example of the polarimetric spectral densities in one radial (elevation  $0.5^\circ$ , azimuth  $180^\circ$ ) for the time instances 7, 8, 9, 10, and 11 pm are presented in Figure 7.2. Color scale shows the values of  $S_h$ ,  $\rho_{hv}$ ,  $\delta$ , and  $Z_{DR}$ . Only spectral coefficients corresponding to  $\rho_{hv}$  larger than 0.7 are displayed. Doppler Spectrum (Figure 7.2  $S_h$ ) depicts several bands (paths) formed by backscattered powers above the background noise. The band at zero velocity shows the residuals from ground clutter filtering. The ground clutter was removed in the frequency domain with a notch-and-interpolate filter. Another band at about  $10 \text{ m s}^{-1}$  is due to the insects carried by the wind while the band at about  $20 \text{ m s}^{-1}$  is due to migrating birds. The Doppler velocity spread of the exposed bands changes as the evening progresses. The spectral spread of the wind/insects' band is about  $7 \text{ m s}^{-1}$  at 6 pm; narrows to  $5 \text{ m s}^{-1}$  at 8 pm; increases again to more than  $10 \text{ m s}^{-1}$  by 9 pm and stays wide from 9 pm to 11 pm.

These changes can be explained by a gradual transformation of the content within the resolution volume from diurnal to nocturnal biological scatterers. Active flying diurnal insects contribute to a wider spectrum at 6 pm. These insects descend prior to the sunset, causing the narrowing of the spectral width at 7 pm and 8 pm. Nocturnal insects and birds rise after sunset when the main flow of nocturnal bird migration starts. Both birds and insects use the wind to increase distances they travel overnight. Birds, being larger and faster flyers, can adjust their heading so that often it does not coincide with the wind direction. Radar detects a combination of echoes

from birds and insects (passive and/or active). The velocities of scatterers are superimposed, which causes a dramatic increase in the spectral width at 9 pm. As long as migration continues the spectrum stays wide (10 pm, 11 pm, etc.). The wind speed and direction estimated from such echoes using standard techniques are wrong and represent neither wind nor bird migration velocity. The region of spectral coefficients above noise exceeds  $20 \text{ m s}^{-1}$  in width. This region contains two paths, one at the velocities of approximately  $10 \text{ m s}^{-1}$  and the other at  $20 \text{ m s}^{-1}$ . The paths are clearly separated in Doppler velocity and indicate that 2 types of scatterers are sharing the airspace. The types can be discriminated if the scatterers in the paths have different polarimetric properties. Consequently, the radial velocities for the recognized types can be extracted. In Figure 7.2 the scatterers in the two paths have different polarimetric properties. One path ( $10 \text{ m s}^{-1}$  at azimuth  $180^\circ$ ) includes echoes mostly from insects. The other path ( $20 \text{ m s}^{-1}$  at azimuth  $180^\circ$ ) contains purely bird echoes. The values of  $\rho_{hv}$ ,  $\delta$ , and  $Z_{DR}$  in the insect/wind path are different from the corresponding values in the bird path (Zrnić and Ryzhkov 1998, Bachmann and Zrnić 2007). The signal power in the paths decreases with range and dissipates. However, the range where the peak power is 20 dB above the noise level extends to 70 km (Figure 7.2  $S_h$ ). The polarimetric values in the paths do not exhibit significant changes in range (Figure 7.2  $\rho_{hv}$ ,  $\delta$ ,  $Z_{DR}$ ). Close to the radar (from 0 to 10 km) the velocities associated with the paths increase with range and then appear stable. This is expected as the wind typically increases with height. Hence, we choose spectral densities

between ranges 20 and 70 km to assess the statistics of the echo content in a radial in a 2D histogram (Section 6.2).

## 7.2. Histograms of spectral densities

Figures 7.3a, 7.3b and 7.3c show 2D histograms of  $Z_{DR}$ ,  $\rho_{hv}$  and  $\delta$  respectively, in the radial at 180° azimuth and during the indicated times of the evening. Each histogram illustrates the prevalence of scatterers with certain polarimetric values in a radial as a function of radial velocity. Dark color represents larger occurrence. The last column of Figure 7.3 was already presented in Figures 6.7, 6.8, and 6.9 with a different color scale and full range of  $\rho_{hv}$ .

Insects can be recognized by the peak in the differential reflectivity and at low velocity in all but 9 pm example. A cluster with largest occurrence (red dot) does not necessarily indicate insects and is indistinct. The histograms of the spectral differential phase show a stable cluster (blob) of phase at 6, 7 and 8 pm that is disrupted at 9 pm. This cluster is from diurnal insects. A similar stable cluster but with larger mean value of phase can be also observed at 10 and 11 pm together with a stretch at larger velocities. The cluster is from nocturnal insects. The stretch is due to birds producing a large span of differential phases. At 9 pm (after the sunset) both insect clusters appear to be present as well as a stretch from birds. Moreover there are occurrences at close to zero velocities. This indicates a transition time when some scatterers descend, other ascend, while still others have already started migrating. The

copolar correlation histograms display clusters for insects and a band (stretch) for birds.

### 7.3. Histograms in discrete radials

Here I extend the analyses presented in Section 7.2 by examining the change in azimuth. Figure 7.4a, 7.4b and 7.4c show ensemble of 2D histograms of  $Z_{DR}$ ,  $\rho_{hv}$  and  $\delta$  respectively constructed for the  $30^\circ$  increments on azimuths from  $30^\circ$  to  $360^\circ$  for the sake of example. Gray shade represents the occurrences, with a larger occurrence depicted by a darker color. Azimuthal and time dependences of the polarimetric spectral densities can be observed from this ensemble. The distributions of scatterers' polarimetric properties form bands ( $\rho_{hv}$ ,  $Z_{DR}$ ), squiggles ( $Z_{DR}$ ) and clusters ( $\rho_{hv}$ , or  $\delta$ ). The scatterers with a narrow spread of velocities and high  $\rho_{hv}$  values dominate at 7 and 8 pm. The velocity distribution is slightly broader at 6 pm and much broader at 9, 10 and 11 pm. There is a pattern with two features in the  $\rho_{hv}$  distribution in azimuths  $30^\circ$  through  $210^\circ$  at 10 pm and 11 pm. First is the concentrated cluster of scatterers (blobs) with  $\rho_{hv}$  in the interval 0.9 to 1 and smaller velocity values. Second is the elongated distribution of scatterers with  $\rho_{hv}$  in the interval 0.7 to 1 and larger velocity values.

The blobs with high  $\rho_{hv}$  values are caused by small insects. Grouping clusters with similar properties in the ensemble of histograms I locate three sinusoids. The clusters with similar differential phase are used at 6 and 7 pm. The blobs from either

histogram can be used at 8 pm. The clusters with the maximum  $Z_{DR}$  values are used at 9, 10, and 11 pm. The VAD sinusoids are manually obtained by connecting the blobs and. Three sinusoids appear to indicate the wind, insects and birds, and are shown with dash-dotted, dotted, and dashed lines respectively. Recall these 2D histograms are computed only for radials spaced by a discrete step of  $30^\circ$ , therefore the fit of sinusoids was performed manually with the purpose to evaluate the feasibility of this method. The high concentration of scatterers with similar phase and velocity forms blobs which are most distinct at 8 pm. At earlier times these are smeared in both velocity and phase, sometimes forming two focus points (blobs). A small velocity difference (about  $3 \text{ m s}^{-1}$ ) and a directional shift (about  $30^\circ$ ) obscure the two scatterer types in the histograms at 6 pm and 7 pm. At later times (9, 10, 11 pm) the wind blobs are surrounded by the irregularly shaped clusters with the apparent dependency in azimuth. The scatterers with high velocities at azimuths  $180^\circ$  through  $240^\circ$  display full range of  $\delta$  ( $-180^\circ < \delta < 180^\circ$ ) at 9 pm. These are caused by birds. However, the same scatterers at different azimuths occupy only a shorter interval of  $\delta$  making it difficult to identify the scatterer type.

At the first glance the  $Z_{DR}$  histograms (Figure 7.4a) display complicated squiggles. However, the maximum  $Z_{DR}$  value in all averages represents the insects. In the presented case it appears that the dominant nocturnal insects are passive wind tracers, which are either not flying or have a random motion relative to the wind, and thus, represent the wind (dash-dotted sinusoid). All additional scatterers contribute to bias the wind velocity (dashed and dotted lines). Furthermore, the difference in the

heading of the scatterer types (maximum in the sinusoids) complicates the situation and causes asymmetry of the composite PPIs. The polarimetric values depend not only on azimuth but also on the directional shift between the scatterers' mean flows.

The presented technique provides opportunity for visual assessment of contamination in a PPI. For two or more sinusoids in a composite VAD, standard techniques for moments and polarimetric variable estimation should be replaced with techniques which use judicious spectral analyses followed by the appropriate recognition and filtering schemes. However, the presented ensemble encompasses only a limited number of discrete azimuth locations (e.g.,  $30^\circ$  increments on azimuth). Visualizing such ensemble (histograms in a queue) becomes difficult for a larger number of azimuths. Stacked 2D histograms (instead of queued on a line) result in a 3D box of occurrences, which is discussed in the next Section.

#### **7.4. Velocity Azimuth Polarimetry Display**

This section explains the formation of a three-dimensional display that can expose signatures of dominant scatterers in velocity, azimuth, and polarimetric variable space. I call this novel 3D visualization display 3DASH in reference to the conventional VAD.

##### **7.4.1. 2D histogram of $\delta$ SD for a sector in range and azimuth**

I use SNR in combination with copolar correlation to censor polarimetric spectral densities. Spectral coefficients with low correlation ( $\rho_{hv} < 0.7$ ) and low power ( $S_h < 5\text{dB} + N_h$ ) are censored in the presented analyses for clarity. To evaluate and quantify

the overall dependence in azimuth I partition the scanned area into portions (Figure 7.5a). Each portion covers an area of  $20^\circ$  in azimuth and 20 km in range. The range is chosen in the “mid range” interval 30 to 50 km to insure sufficient SNR and absence of ground clutter residuals. We estimate  $\delta SD$  in each portion and make a 2D histogram of the resultant spectral field. An example of the 2D histogram is presented in Figure 7.5b. This histogram is for the portion at azimuth  $140^\circ$ , indicated in Figure 7.5a. Such histogram shows occurrences of scatterers that have the backscatter differential phase  $\delta$  within 30 intervals of  $12^\circ$  each, and exhibiting specific radial velocity within 128 intervals of  $0.55 \text{ m s}^{-1}$  each. Gray scale shows the number of occurrence. Because of censoring the field of occurrences is sparse.

Two clusters are visible in Figure 7.5b, a dim broad cluster and a confined bright cluster (blob). The dim cluster covers a large area with velocities in the range from  $-10$  to  $-20 \text{ m s}^{-1}$  and backscatter differential phase in the range from  $0^\circ$  to  $150^\circ$ . The bright blob covers an area with velocities in a range from  $-3$  to  $-10 \text{ m s}^{-1}$  and backscatter differential phase in the range from  $50^\circ$  to  $100^\circ$ . From mean values of radial velocities, the blob is due to the wind blown insects, while the dim cluster is caused by migrating birds.

#### 7.4.2. 3D histogram of $\delta SD$

Collection of the described 2D histograms forms a 3D box. There are 18 azimuthal locations (Figure 7.5a) and 128 bins for the radial velocity with values from  $-35$  to  $35 \text{ m s}^{-1}$  and 30 bins for the backscatter differential phase with values from  $-180^\circ$  to  $180^\circ$ . I illustrate the formation of the 3DASH with five histograms in

Figure 7.6a. Gray scale represents the number of occurrences. If there were an overlap between two images depicting the histograms the viewer would not be able to observe the obscured occurrences. To a certain degree obscuration can be avoided using color transparency (Foley et al. 1996, MathWorks 2006). Figure 7.6b depicts the same five histograms as in Figure 7.6a but after making the small counts transparent. Consequently all 18 histograms are visible in Figure 7.6c. A small number of occurrences is concealed with transparency for clarity of the internal view. This is the 3DI “differential phase”-velocity-azimuth display. The transparency permits to look inside the 3D box and observe properties hidden otherwise. The degree of transparency can be adjusted. In the presented examples transparency is 10 % of maximum occurrence

The well defined clusters from different azimuth locations (such as the one presented in Figure 7.5b) forms a helix-like curl which projects a sinusoidal path in velocity-azimuth-plane (Section 7.5). The azimuth- $\delta$ -plane and the velocity- $\delta$ -plane are expected to expose the azimuthal change of differential phase. Define spectral spread as the width of helix in the velocity space. The spectral spread is narrower than the standard spectral width (square root of second moment) because of censoring and concealing 10% of occurrences. Similarly, define phase spread as the width of helix in the differential phase space. The combination of spectral spread and the phase spread of the helix-like curl can indicate the purity of detected scatterer type and the harmony of its behavior. The scatterers moving in unison and exhibiting similar shape

are expected to have narrow spectral spread, narrow phase spread, and large number of occurrences.

### **7.5. Example of 3DASH for evaluation of contributing scatterers**

Herein I evaluated the composition of scatterers and its evolution over the evening. Favorable winds and fair weather conditions prompted bird and insect migration. Diurnal birds were outnumbered by two types of insects in the evening until the sunset (about 7:50 pm). I classify the two types of insects as active and passive. Birds and active insects descended by sunset. Passive insects' signatures were still present an hour after the sunset (9 pm) but gradually disappeared (by 10 pm). After the twilight (about 9:30 pm) commotion of multiple scatterers with diverse polarimetric signatures was identified. Nocturnal migrating bird ascended faster than insects. Birds formed several layers at different altitudes. The layer below 2 km in altitude was occupied by nocturnal migrating insects who shared their space with migrating birds. I use 3DASH to confirm our previous findings and to illustrate the potential of this new display. The important point is that special censoring schemes can be created to display diverse contributing types. The censoring procedure in the presented examples is aimed to weaken the migrating birds' contributions. I hypothesize that active diurnal insects descend rapidly and are completely landed by sunset, while passive diurnal insect fall out and are still falling after the sunset. If the insects fall speed is  $0.5 \text{ m s}^{-1}$  and the altitude between 1 km and 2 km it takes insects between 30 minutes to an hour to reach the ground.

### 7.5.1. Clear Air Traced by Passive Insects

Among the presented three cases, the most uniform is the 8 pm case (Figure 7.7). This case occurred immediately after the sunset. The helix appears symmetric and well defined. The projections clearly show sinusoidal bands in both velocity-azimuth and  $\delta$ -azimuth planes. The  $\delta$ -velocity plain shows a well defined ellipse with more occurrences at locations corresponding to maxima in the  $\delta$ -azimuth sinusoid. Both spectral and phase spreads are relatively narrow. Symmetric and passive scatterers such as small insects are the possible cause of such a signature. Our examination of the scatterers' behavior indicates that most of diurnal active biological scatterers descended by 8 pm and nocturnal biological scatterers have not ascended yet. Therefore we conclude that the perfect helix signature is caused by the non-migrating insects.

### 7.5.2. Precipitation-free Air filled with Ascending Birds and Insects

A contrasting example occurred one hour later at 9 pm (Figure 7.8) wherein the helix is severely distorted. There are many occurrences indicating small and large velocities. The ellipse in the  $\delta$ -velocity plane still has features similar to the ellipse at 8 pm, nonetheless, there are many additional occurrences with large positive values of differential phase. The projections indicate significant broadening of the sinusoidal bands. Additional occurrences are seen in the azimuths between  $150^\circ$  and  $220^\circ$ . Occurrences in azimuths between  $150^\circ$  and  $220^\circ$  show large spread of  $\delta$  and are from migrating birds. Comparing  $\delta$ -azimuth plane at 8 pm and 9 pm we find additional scatterers with positive values of  $\delta$  at all azimuths. These are signatures of nocturnal

active (migrating) insects. From resemblance with 8 pm case we deduce that in this example the passive (non-migrating or migrating without an effort) insects' signature is still present. A broadening of phase spread is due to nocturnal insects, although nocturnal insects are not numerous enough to mask birds' signatures. As the amount of insects increases, their signatures tend to stand out in the histograms because of tight clustering; moreover the contributions from migrating birds would censor out due to sporadic nature of bird beam filling and the censoring scheme. The polarimetric properties of nocturnal insects can be compared with those in clear air at twilight from the difference of 3DASH at 9 am and at 8 pm.

### 7.5.3. Insects in Precipitation-free Air and at Night

By 10 pm (Figure 7.9) the helix clears up and exhibits positive  $\delta$  that slightly drifts having phase between  $0^\circ$  and  $100^\circ$  at north, between  $20^\circ$  and  $100^\circ$  at east, between  $50^\circ$  and  $100^\circ$  at south, and drops to  $-30^\circ$  to  $70^\circ$  at west. The ellipse is replaced by a sideways-figure-eight in the  $\delta$ -velocity plain. The largest occurrences in the sideways-figure-eight show mirrored phase of about  $70^\circ$ . These are nocturnal migrating insects. A patch of bird phases at azimuth  $200^\circ$  is evident. This patch is the residual contamination from nocturnal migrating birds whose signatures did not censor out (see Figure 6.14 at azimuth  $200^\circ$ ).

The 10 pm case is interesting because of the mixture of the scatterer types moving in different directions with different velocities. Any additional information of the resolution content might prove useful. Therefore in addition to already presented in Figure 7.9 3DASH of the differential phase, I present the 3DASHs of the

differential reflectivity and copolar correlation coefficient in Figure 7.10. These 3DASHS are shown with a grayscale with darker color representing larger occurrence. In the 3DASH of differential reflectivity (Figure 7.10a) clusters form two broad curls. One of these shapes is a relatively better formed helix. It indicates smaller velocities and larger differential reflectivity values and therefore is due to insects. The other clustering appears irregular and is due to birds. Rotation of the 3DASH is a must for a user to fully appreciate the capability of this novel display. Figure 7.10a shows a view (a position of the 3D object) in which the helix-like shape from insects and the other shape of sporadic occurrences from birds are displaced from each other in velocity and direction. In the 3DASH of copolar correlation (Figure 7.10b) clusters form a sinusoid-like curl (in the azimuth velocity plane) of high correlation values, indicating small insects. The other occurrences with gradually diminishing values from high (overlapping the ones for insects) to small are from birds. An unexpected observation is a burst of high correlation values at  $200^\circ$  with high velocity values caused by birds. This region can be also observed in  $Z_{DR}$ . This is a case wherein birds have higher  $Z_{DR}$  and  $\rho_{hv}$  than insects. A possible explanation is a favorable orientation. This is an important observation. Previously reported comparison of the mean  $Z_{DR}$  values of insects and birds still holds. Nonetheless, it is important to realize that there are that there are situations in which the birds and insects mean  $Z_{DR}$  signatures can be misinterpreted. In the 3DASH of differential phase (Figure 7.10c) clusters form a helix-like curl. The scatterers moving in unison and exhibiting similar shape and orientation are expected to produce a well defined

helix. Birds have noise-like differential phases. Insects have a narrow band of phases that changes in azimuth. Therefore this 3DASH depicts the insects well. This is by far the most visually pleasing 3DASH.

#### 7.5.4. Summed up 3DASH

The presentations in figures 7.7, 7.8, and 7.9 are convenient for viewing the distribution of occurrences in the three dimensional space, but can not be used to determine the actual numbers. This is because the occurrences are modulated by transparency so that an outside envelope of the histogram corresponding to the first value above a threshold is observed. Thus the views at different look angle (top, left, front) expose the first values exceeding the threshold while the values behind are essentially obscured.

For quantitative representation summed values over any one of the variables produces two dimensional histograms in which the number of occurrences can be easily quantified. Such histograms are shown in Figure 7.11 and 7.12 for the times from 6 pm to 11 pm. A darker shade of gray represents larger occurrence. The images organized in 3 columns such that the left column shows the velocity-azimuth histogram, center column shows the velocity-“polarimetric variable” histogram, and right column displays the “polarimetric variable”-azimuth histograms.

The velocity-azimuth histograms (left column in Figures 7.11 and 7.12) signify that the spectral spread of dominant scatterer slightly decreases by 8 pm and tremendously increases by 9 pm. This indicates the descent of diurnal scatterers and ascent of nocturnal scatterers exhibiting large range of velocities. The velocity- $\delta$

histograms (Figure 7.11 middle column) capture a change in pattern from almost circular at 6 pm, to a symmetric elliptical at 8 pm, and transforming to a different symmetric pattern resembling figure-eight by 11 pm. The location of dominant scatterers (blobs) is easily seen from these histograms. The velocity- $Z_{DR}$  histograms (Figure 7.12 middle column) reveal fuzzy pattern that is approximately symmetric relative to zero velocity. At earlier times (6 pm and 7 pm) the  $Z_{DR}$  values in the pattern fill in between 3 dB and 15 dB. At later times there are more occurrences below 10 dB. The occurrences velocity- $Z_{DR}$  histograms do not cluster as well as in the velocity- $\delta$  histograms.

The  $\delta$ -azimuth histograms (Figure 7.11 right column) expose a remarkable “flip” in phase at 8 pm associated with sunset (at about 7:50 local time). I do not know what caused it and speculate that it could be from an extensive change in scatterers’ orientation and composition, or some artifact. If the scatterers are indeed responsible then the sinusoidal  $\delta$ -azimuth dependence at 8 and 9 pm and an almost linear dependence at 11 pm are important features that could be used for establishing values of intrinsic polarimetric variables, useful for classification algorithms. The  $Z_{DR}$ -azimuth histograms (Figure 7.12 right column) are fuzzy and are hard to interpret. Although the dumb-bell pattern is present the strength of  $Z_{dr}$  is not even; the values east of the radar are weaker than the ones to the west. Dominant insects of the same type are expected to have similar polarimetric signatures. A possible adaptive strategy to sense the dominant insects’ signature is given in Section 7.6.

## 7.6. Insects' intrinsic polarimetric values

In previous section it was shown that biological scatterers occupying the atmosphere at different times of day produce different polarimetric signatures. The signature of insects is important because (1) the velocity of insects is close to the environmental wind; (2) the reflectivity of insects can be higher than that of clear air. Compared to birds, insects have higher values of  $\rho_{hv}$  and  $Z_{DR}$ , with some exceptions. It was shown in Section 7.5.3 that birds could have higher values of  $\rho_{hv}$  and  $Z_{DR}$ . Nonetheless, the later do not pose a problem if the velocity values are included in analyses, because birds fly faster than insects. Therefore, I present a scheme for adaptive selection of spectral coefficients most probably produced by insects' returns that are likely good tracers of the wind.

The procedure is summarized below.

1. Choose range span (i.e., range span of 5 km in the presented case, results in 20 range locations for analyses, and about 100 m in height).
2. Select azimuth.
3. Estimate power spectral densities ( $S_h$  and  $S_v$  with dimensions 128×20 for the presented case).
4. Filter ground clutter.
5. Estimate spectral densities of polarimetric variables ( $Z_{DR}$ ,  $\rho_{hv}$ ,  $\delta$ , with dimensions 128×20 each).
6. Estimate adaptive mask:
  - a) compute mean in range of  $Z_{DR}$  and  $\rho_{hv}$  (dimensions 128×1 each);

- b) normalize mean of  $Z_{DR}$  and mean of  $\rho_{hv}$ ;
  - c) multiply normalized curves from b);
  - d) threshold the resulting curve so that top half is 1 and bottom half is 0;
  - e) find the beginning and the end of the unmasked window (1s).
7. Mask spectral polarimetric densities (dimensions adaptive $\times$ 1 each).
  8. Compute mean of the unmasked portion of spectral polarimetric densities (dimensions 1 $\times$ 1 each).
  9. Repeat steps from 2 to 8 for all the azimuth locations.

I applied this procedure to evaluate insects' polarimetric signatures at ranges from 30 to 35 km. The resulting curves are shown in Figure 7.13 for the earlier evening times (6, 7 and 8 pm). The same curves smoothed with a 9 point median filter are given in Figure 7.14. The azimuthal dependences and the values in these plots indicate that the peak values of  $Z_{DR}$  are reaching 10 dB at 6 pm, increase to 12 dB at 7 pm and decrease to 5 dB to the east and 7 dB to the west of the radar by 8 pm. The discontinuities at about 160° and at 320° in the Figure 7.14 are due to partial degradation of signals from ground clutter filtering in the region of zero radial wind velocity. The flip in phase at 8 pm is difficult to explain. The change of insects' intrinsic polarimetric variables in time is shown in Figure 7.15. The uneven spacing in collection of volume scans results in empty columns in the images. The discontinuities (due to ground clutter filtering at the zero radial velocity) appear as paths at about 120° and 300°. Overall images show that a big change happened during the sunset. Perhaps if more data was collected between 7:50 pm and 8 pm the cause

of backscatter phase flip would be obvious. With the existing dataset I can only speculate. Possible explanations for the observed phase flip at sunset are:

1. Insects to the east of the radar see sunset before the insects to the west, and orient head down causing the decrease in intrinsic  $Z_{DR}$  by about 2 dB.
2. Insects from a higher altitude to the east of the radar see sunset before the insects from the lower altitude to the west and descend. This creates a situation in which there are two types of insects: the higher altitude insects to the east and the lower altitude insects to the west.
3. Insects to the east of the radar are already ascending nocturnal insects. This also creates a situation with two types of insects: the nocturnal insects to the east and the diurnal insects to the west of the radar.

## **7.7. Conclusion**

An extension of conventional VAD to a novel three-dimensional display (3DASH) allows assessing of polarimetric properties, azimuthal dependences, and velocity distributions of contributing scatterers. Appropriate censoring can be applied to mask undesirable contributors by discarding their polarimetric spectral densities. Such censoring leaves small occurrences of these unwanted signatures in histograms. Setting transparency for the insignificant occurrences provides a visualization tool to glean at the internal 3D polarimetry-velocity-azimuth field of the occurrences. The wind signature produces a helix in the 3DASH from which one can obtain the usual divergence, wind speed, direction, and deformation. Also the helix reveals the dependence (mean and spread) of polarimetric variables as a function of azimuth.

The 3DASH analyses can be used to investigate and establish the values (functions) of polarimetric variables for filtering and recognition, to assess the degree of contamination and its azimuthal disparity, and to evaluate the composition of the detected motion. Once the values are established the adaptive automated procedures can be used to compute intrinsic polarimetric variables.

## **8. Parametric spectral estimation techniques**

In this section parametric spectral estimation techniques are explored for a potential to estimate the true wind velocity.

### **8.1. Composite spectrum – speculations**

During bird migration season the velocity in precipitation-free air mainly consists of a combination of velocities of birds and insects. It was shown that the insect velocity can be estimated from such severely contaminated data. However, the example at 11 pm indicates that decontaminated velocity is still biased by about  $3 \text{ m s}^{-1}$  (Figure 6.18) at low elevations. The ensemble of histograms presented in Section 7 also hints that there is something else in the resolution volume beside migrating birds and insects. I investigate the spectral shape and assume that there are 3 types of scatterers present in a resolution volume, at least at ranges between 20 and 50 km (and heights between 200 meters and 600 meters). Figure 8.1 illustrates my speculations. Because the wind is assumed to be known from sounding it can be modeled as a Gaussian centered at the wind velocity (Figure 8.1d). The migrating birds tend to fly with similar velocities and therefore bird spectral peaks can be modeled with a Gaussian positioned at the mean bird velocity (Figure 8.1b). The spectral coefficients peaking between birds and wind contribution (Figure 8.1c) could be the contributions from actively flying insect. The mean velocities of these scatterer types (Figures 8.1b, 8.1c and 8.1d) can be viewed as three spectral peaks superposed

on a noise floor (Figure 8.1f). These velocities can be estimated using parametric spectral modeling.

## **8.2. Examples of spectra estimated using different methods**

Spectral density fields along the same radial are assessed using different PSD estimation methods and presented in Figure 8.2. The periodogram and the multi taper method (MTM), shown in Figure 8.2a and 8.2b respectively, are nonparametric methods. I present these here for visual assessment of parametric methods. MTM uses combinations of modified periodograms to estimate the PSD. These periodograms are computed using a sequence of orthogonal tapers (windows in the frequency domain) specified from the discrete prolate spheroidal sequences (MathWorks, 2006). Presented spectra estimated using MTM with three tapers (Figure 8.2b), results in a smoother estimate than periodogram. Parametric methods such as Modified covariance (MC) and Burg are shown in Figure 8.2c and 8.2d respectively. The subspace methods are a part of parametric techniques that are also known as frequency estimation techniques. The subspace methods are based on eigen decomposition of the correlation matrix and are good for detecting sinusoids in noise. Eigen value decomposition (EV) and multi signal classification (MUSIC) methods require a prior knowledge of signal content such as the number of complex sinusoids, and do not preserve power. However, the subspace methods provide a good frequency resolution even for a considerable small number of samples (MathWorks, 2006). Because frequency can be translated to Doppler velocity these methods are promising

for the true wind estimation. The presented parametric methods use argument three which indicates the number of modeled sinusoids (Figure 8.1f). The purpose of this investigation is to determine if any of the available methods when applied to the signal along the radial can position an additional band close to the insect/ wind band. It appears that both MC(3) and Burg(3) fail, and both EV(3) and MUSIC(3) detect such additional band at ranges from about 30 to 50 km. Moreover, MUSIC(3) appears to provide better resolution at the indicated location. Therefore I choose MUSIC method for further investigation.

The zoomed in portion of PSDs estimated using Periodogram and MUSIC are shown in Figure 8.3. The PSDs estimated with autoregressive models of order AR(2) and AR(3) are presented in Figure 8.3b and 8.3c respectively. The AR(2) model shows two definite bands representing mean velocities of the birds and the insects. The AR(3) model shows three bands but the velocities corresponding to these bands are less prominent. The AR(3) model appears to split the insect band into two bands at about  $5 \text{ m s}^{-1}$  and  $10 \text{ m s}^{-1}$ . The atmospheric sounding (rawinsonde) at 0 UT detected  $7 \text{ m s}^{-1}$  wind at the surface. However, the velocity estimated using the spectral VAD technique at 4 UT and 30 km range was  $12 \text{ m s}^{-1}$  in the direction of the wind ( $220^\circ$ ) and  $9 \text{ m s}^{-1}$  in the  $180^\circ$  radial. Either the wind increased from 0 UT to 4 UT or the insects were active flyers. The AR(2) estimate has a peak at  $7 \text{ m s}^{-1}$  and 30 km range. AR(3) models approximate two peaks (at  $5$  and  $10 \text{ m s}^{-1}$ ) at 30 km range. These appear to be the trace of passive insects carried by the wind and the trace of the mean velocity of active insects.

The  $Z_{DR}$  between the modeled channels (not shown) exhibits the polarimetric differences in bands with higher values for the insect band. Although it appeared correct for the presented example, I do not think such a  $Z_{DR}$  parametric spectral density is trustworthy. If the peaks in the modeled PSDs of H and V channels do not exactly match then the  $Z_{DR}$  values may vary dramatically. I suspect that the AR(2) model captures the wind and birds velocities accurately, as determined by independent observations. It seems that the AR(3) model correctly obtains the velocity of the true wind and therefore can be used to determine the bias.

### **8.3. Processing technique**

The reason that I use a combination of non-parametric and parametric spectral analyses is based on the following. First, the non-parametric technique is well known and accepted for the weather radar applications. Second, the parametric technique we use requires a prior knowledge of the physical process which the non-parametric method can provide. Third, meteorological parameters such as spread of Doppler velocities, and reflectivity are difficult to obtain with parametric methods. And last, at low elevations the ground clutter is sporadic and therefore the model order for matching the physical process is not known unless there is a priori or spectral information.

The presented technique is summarized below:

1. Estimate non-parametric spectrum (DFT) for each resolution volume.

2. Apply the Smirnov-Kolmogorov test on the spectrum coefficients to estimate the noise power. Then remove the noise.
3. Check power of spectral coefficients at and close to zero velocity; notch them if ground clutter is detected; interpolate across the notch using adjacent non-clutter coefficients.
4. Compute polarimetric spectral densities from the spectra of the horizontal and vertical channels.
5. From polarimetric spectral densities estimate the number of the scatterer types.
6. Perform the IDFT on the ground-clutter corrected signal.
7. Estimate spectrum using the parametric model of the order estimated in 5.
8. Extract the wind velocity from the band of passive scatterers in the spectra using a special technique.

## 9. Conclusion

Polarimetric spectral analysis of the weather radar returns in precipitation-free air, in the evening and at night reveals the simultaneous presence of migrating birds and insects mixed within the radar resolution volumes throughout the lower atmosphere. The polarimetric variables (reflectivity, differential reflectivity, copolar correlation coefficient, and differential phase) associated with resolvable Doppler shifts are computed from the power spectra of horizontally and vertically polarized returns. Thus the spectral density of these polarimetric variables exhibit separation of the two species. The speed measurements of insects and migrating birds can be resolved by constructing spectral VADs and isolating the insect velocity sinusoid from the additional sinusoids caused by contaminants such as birds. Further, from the combined use of the spectral densities of the polarimetric variables it might be possible to reconstruct velocity azimuth (VAD) profiles of the wind. Specifically, I use the spectral densities of copolar correlation coefficient and the spectral noise level to isolate the spectral values of  $Z_{DR}$  which are caused by insects. Then I associate the Doppler velocity at the maximum value of such thresholded spectral density of  $Z_{DR}$  with the return from insects and perform a VAD analysis on these velocities.

The possibilities offered by polarimetric spectral analysis are immense and have hardly been explored. The distributions of polarimetric variables in velocity provide a unique way for observing multiple processes in each resolution volume and understanding the values of the resulting polarimetric averages. I presented techniques which can be used for quality assessment of the spectral moments and

polarimetric variables. I extended one dimensional VAD analyses to two dimensions (SVAD), and then, further to three dimensions (3DASH).

I demonstrated the ability of the two dimensional SVAD to capture the velocities of two scatterer types, migrating birds and insects, at the same time. This provides information for meteorologists (wind direction and speed) and for ornithologists (birds mean motion direction and speed) simultaneously. This technique can also be used for the quality assessment of a PPI. If there is one sinusoid in the VAD, then the dominant scatterers are of one type, and the moments in PPIs reflect the signatures of this type of scatterers. If there are two or more sinusoids in the VAD, then the moment show biased estimates and should be recalculated using more sophisticated (spectral) techniques. I demonstrated the potential of the three dimensional azimuthal spectral histogram 3DASH to capture not only direction and velocities of dominant scatterer types but also their intrinsic polarimetric signatures. This is a first step on the way to understand and explore the constitution of the polarimetric averages widely used in scatterer classification algorithms.

I have observed and documented a case depicting the “schedule” and the interactions of the diurnal and nocturnal scatterer. The diversity in intrinsic polarimetric signatures of scatterers in the same class “insects” is presented. Actively flying insects vigorously hold their schedule and descend/ascend on time. Passively blown insects depend on environmental conditions and have to fall for more than an hour trying to reach the ground. The intrinsic polarimetric signatures of, say, two types of insects can be vastly different and depend on heading (which does not

necessarily coincide with the wind). Large insects, with elongated bodies, have strong azimuthal dependencies, larger maxima and smaller minima in  $Z_{DR}$ . Smaller insects with more spherical bodies have less azimuthally pronounced polarimetric signatures with smaller  $Z_{DR}$ . The spans of  $\delta$  of the two types of insects are also different (in values and in the width of span). The 3DASH can be used to document these azimuthal function and the widths of spans of values for the scatterer type of interest.

I documented an unexpected observation revealed by the 3DASH. Apparently, there are cases when intrinsic  $Z_{DR}$  of birds is larger than that of insects. This observation illustrates the potential of 3DASH to raise awareness and to provide recourses for understanding of the polarimetric means. I proposed a special technique on the polarimetric spectral densities for estimating the backscatter differential phase inherent to insects. The dependence of  $\delta$  in azimuth is smooth compared to the dependence of  $\delta$  obtained by standard procedures. Nonetheless, the values in the east and west semicircles of radar coverage defy simplistic explanation. The changes are surprisingly rapid so that observations at less than five minute intervals are needed to capture the continuity of evolution at the time of sunset. Even after the sunset and well into the night the biological inhabitants of the PBL continually present evolving and somewhat inhomogeneous fields of polarimetric variables. I have observed and documented the remarkable “flip” in  $\delta$  during the sunset although I could not explain it. Further studies with the rapid volume scan strategies during the sunset are needed to examine and make sense of the observed phenomenon.

I have demonstrated that an autoregressive model can pinpoint several velocities of contributing scatterers within the same resolution volume. I believe this is the first attempt to identify velocities of three (not one) types of contributing scatterers for a single resolution volume. I have shown that the combination of non-parametric and parametric spectral analyses can identify birds, insects and wind.

## References

- [1] G.L. Achtemeier, “The use of insects as tracers for clear air boundary-layer studies by Doppler radar,” *J. Atmos. Oceanic Technol.*, 8, 746–765, 1991.
- [2] W.M. Angevine, “Errors in mean vertical velocities measured by boundary layer wind profilers,” *J. Atmos. Oceanic Technol.*, 14, 565–569, 1997.
- [3] S.M. Bachmann and D.S. Zrnić, “Spectral density of polarimetric variables separates biological scatterers in the VAD display,” *J. Atmos. Oceanic Technol.*, Amer. Meteor. Soc., to be published 2007.
- [4] E.A. Brandes, “Dual-polarization radar fundamentals and algorithm prospects, Report on Next Generation weather radar program – operational support facility, WSR-88D Commerce-Defense-Transportation,” May 2000.
- [5] M.M. Butler and D.A. Johnson, “Feasibility of Mitigating the Effects of Wind farms on Primary Radar,” *Alenia Marconi Systems Limited*, ETSU W/14/00623/REP DTI PUB URN No. 03/976, 2003.
- [6] J.W. Chapman, D.R. Reynolds, A.D. Smith, E.T. Smith and I.P. Woiwod, “An aerial netting study of insects migrating at high altitude over England,” *Bulletin of Entomological Research*, 94, 123-136, 2004.
- [7] T. Cole, “Bird Strikes A Growing Concern...As Spring Gets Everyone Flying,” Aviation Publishing Group, 2005. Available online <http://www.avweb.com/eletter/archives/avflash/214-full.html#186949>
- [8] L.B. Cornman, R.K. Goodrich, C.S. Morse, and W.L. Ecklund, “A fuzzy logic method for improved moment estimation from Doppler spectra,” *J. Atmos. Oceanic Technol.*, 31, 1287-1305, 1998.
- [9] T.J. Dean and V.A. Drake, “Properties of biotic targets observed with an X-band radar profiler and the potential for bias in winds retrieved from Doppler weather radars,” Proc. *11th Australasian Remote Sensing and Photogrammetry Conf.*, Brisbane, Queensland, Australia, Australian Institute of Remote Sensing, 698–711, 2002.
- [10] R.H. Diehl and R.P. Larkin, “Introduction to WSR-88D (NEXRAD) for Ornithological research,” *USDA forest service Gen. Tech. Rep.* PSW-GTR-191, 13 pp, 2004.
- [11] R.J. Doviak and D.S. Zrnić, *Doppler Radar and Weather Observations*, Academic Press, 1993, p. 562.

- [12] V.A. Drake and A.C. Gatehouse, *Insect Migration*, Cambridge University Press, 1995, p. 478.
- [13] H.Q. Feng, K.M. Wu, D.F. Cheng, and Y.Y. Guo, "Radar observation of the autumn migration of the beet armyworm *Spodoptera exigua* and other moths in northern China," *Bulletin of Entomological Research*, 93, 115-124, 2003.
- [14] J.D. Foley, van Dam A., S.K. Feiner and J.F. Hughes, *Computer Graphics: Principles and Practice*, Addison-Wesley Publishing Company, Inc., 1996.
- [15] G. Galati, *Advanced Radar Techniques and Systems*. Peter Peregrinus Ltd., 1993.
- [16] S.A. Gauthreaux Jr., and C.G. Belser, "Displays of bird movements on the WSR-88D: Patterns and Quantification," *Weather and Forecasting*, Amer. Meteor. Soc, 13, 453-464, 1998.
- [17] S.A. Gauthreaux Jr., D.S. Mizrahi, and C.G. Belser, "Bird migration and bias of WSR-88D wind estimates," *Weather and Forecasting*, Amer. Meteor. Soc 13, 465-481, 1998
- [18] F.B. Gill, *Ornithology*, 2<sup>nd</sup> edition Freeman & Cia, 1994.
- [19] E.E. Gossard, "Radar research on the atmospheric boundary layer," *Radar in Meteorology*, D. Atlas, Ed., Amer. Meteor. Soc., 477-527, 1990
- [20] R. Grantham and D.C. Arnold, "Beneficial insects," *Oklahoma Cooperative Extension Fact Sheets F-7307, 7307-1 – 7307-7*, 2005.
- [21] B. Greerts and Q. Miao, "A simple numerical model of the flight behavior of small insects in the atmospheric convective boundary layer," *J. Environmental Entomology*, 34(2), 353-359, 2005.
- [22] T. Griesser and H. Richer, "Multiple peak processing algorithm for identification of atmospheric signals in Doppler radar wind Profiler spectra," *J. Meteorol. Zeitschrift*, N.F. 7, 292-302, 1998.
- [23] R.C. Goff, F. Amodeo, D. Pace, J. Tauss, "Future FAA operational needs for WSR-88D architecture," *IEEE Proc. Aerospace and Electronics Conference*, NAECON 1997, 1, 341 - 345 pp., 1997.
- [24] M.H. Hayes, *Statistical Digital Signal Processing and Modeling*, John Wiley & Sons, 1996.

- [25] I. Holleman, H. V. Gasteren, and W. Bouten, "Validation of bird movement signatures in weather radar wind profiles using a dedicated bird radar," *32nd Conf. on Radar Meteorology*, Albuquerque, NM, Amer. Meteor. Soc., P7R12, 2005.
- [26] D.L. Hartmann "Cross Spectrum Analysis," ATM552 notes, available online at [www.atmos.washington.edu/~dennis/552\\_Notes\\_6c.pdf](http://www.atmos.washington.edu/~dennis/552_Notes_6c.pdf), 2006.
- [27] K. Jungbluth, J. Belles, and M. Schumacher, "Velocity contamination on WSR-88D and wind profiler data due to migrating birds," Preprints, *27<sup>th</sup> Conf. on Radar Meteorology*, Vail, CO, Amer. Meteor. Soc., 666–668, 1995.
- [28] V. Kezys, E. Torlaschi, and S. Haykin, "Potential capabilities of coherent dual polarization X-band radar," Preprints, *26<sup>th</sup> Int. Conf. on Radar Meteorology*, Norman, OK, Amer. Meteor. Soc., 106-108, 1993.
- [29] T.J. Lung, S.A. Rutledge, and J. Stith, "Observations of clear air Dumbbell-shaped echo patterns with the CSU-CHILL polarimetric radar," *J. Atmos. Ocean. Technol.*, 21, 1182-1189, 2004.
- [30] R.P. Larkin, W.R. Evans, and R.H. Diehl, "Nocturnal flight calls of Dickcissels and Doppler radar echoes over South Texas in Spring," *J. Field Ornithol.*, 73, 2-8, 2002.
- [31] R.P. Larkin and R.H. Diehl, "Spectrum width of birds and insects on pulsed Doppler radar," *Illinois Press*, 20 pp., 2001.
- [32] R.M. Lhermitte and D. Atlas, "Precipitation motion by pulse Doppler radar," *Proc. 9th Weather Radar Conf.*, Kansas City, AMS, 218-223, 1961.
- [33] E.M. Martner and K.P. Moran, "Using cloud radar polarization measurements to evaluate stratus cloud and insect echoes," *J. Geophys. Res.*, 106, 4891–4897, 2001.
- [34] C.S. Morse, R.K. Goodrich, and L.B. Cornman, "The NIMA method for improved moment estimation from Doppler spectra," *J. Atmos. Ocean. Technol.*, 19, 274-295, 2002.
- [35] E.A. Mueller and R.P. Larkin, "Insects observed using Dual-Polarization radar," *J. Atmos. Ocean. Technol.*, 2, 49-54, 1985.
- [36] E.A. Mueller, "Differential reflectivity of birds and insects," Edmonton, Canada, Amer. Meteor. Soc, 1983.

- [37] D.E. Pedgley, D.R. Reynolds, J.R. Riley, and M.R. Tucker, "Flying insects reveal small-scale wind systems," *Weather*, 37, 295–306, 1982.
- [38] R. Rabin and R. J. Doviak, "Meteorological and astronomical influences on radar reflectivity in the convective boundary layer," *J. Appl. Meteor.*, 28, 1226-1235, 1989.
- [39] R. Rabin and D. Zrnić, "Subsynoptic-scale vertical wind revealed by dual Doppler radar and VAD Analysis," *J. Atmos Sciences*, 37, 644-654, 1979.
- [40] J.R. Riley, "Radar cross section of insects," *Proc. IEEE.*, 73, 228–232, 1985.
- [41] J.R. Riley, "Radar returns from insects: Implications for meteorological radars," Preprints, *29th Int. Conf. on Radar Meteorology*, Montreal, QC, Canada, Amer. Meteor. Soc., 390-393, 1999.
- [42] R.E. Rinehart, *Radar for Meteorologists*. Rinehart Publications, 1997.
- [43] H. Russchenberg, L. Lighthart, J. Baptista, and G. Brussaard, "Remote sensing of precipitation with a multipolarised Doppler (FM-CW) research radar: Application to propagation studies," *J. ESA*, 1, 87-100, 1990.
- [44] R.W. Russell and J. W. Wilson, "Radar-observed "fine lines" in the optically clear boundary layer. Reflectivity contributions from aerial plankton and its predators," *Bound.-Layer Meteor.*, 82, 235–262, 1997.
- [45] A.V. Ryzhkov, S.E. Giangrande, and T.J. Shuur, "Rainfall estimation with a polarimetric prototype of WSR-88D," *Applied Meteor.*, 44, 502-515, 2005.
- [46] M.I. Skolnik, *Radar Applications*, IEEE press, 1987.
- [47] G.W. Stimson, *Introduction to Airborne Radar*, SciTech Publishing Inc., 1998.
- [48] S. Torres, and D.S. Zrnić, "Ground Clutter Filtering with a Regression Filter," *J. Atmos. Ocean. Tech.*, 16, 1364-1372, 1999.
- [49] R.E. Saffle and L.D. Johnson, "NEXRAD product improvement overview," *IEEE Proc. Aerospace and Electronics Conference*, NAECON, 1, 288-293, 1997.
- [50] T. Schuur, A.V. Ryzhkov and P. Heinselman, "Observation and classification of echoes with the polarimetric WSR-88D Radar," *NSSL Report*, October 2003.
- [51] D. Sirmans, "Calibration of the WSR-88D," *OSF Report*, 1992.

- [52] C.M.H. Unal and D.N. Moisseev, "Combined Doppler and polarimetric radar measurements: correction for spectrum aliasing and nonsimultaneous polarimetric measurements," *J. Atmos. Oceanic Tech.*, 21, 443-456, 2004.
- [53] C.R. Vaughn, "Birds and insects as radar targets: A review," *Proc. IEEE*, 73, 205-227, 1985.
- [54] J.M. Wilczak, R.G. Strauch, F.M. Ralph, B.L. Weber, D.A. Merritt, J.R. Jordan, D.E. Wolf, L.K. Lewis, D.B. Wuertz, J.E. Gaynor, S.A. McLaughlin, R.R. Rogers, A.C. Riddle, and T.S. Dye, "Contamination of Wind Profiler Data by Migrating Birds: Characteristics of Corrupted Data and Potential Solutions," *J. Atmos. Ocean. Tech.*, 12(3), 449-467, 1995.
- [55] J.W. Wilson, T.M. Weckwerth, J. Vivekanandan, R.M. Wakimoto, and R.W. Russell, "Boundary layer clear air radar echoes: Origin of echoes and accuracy of derived winds," *J. Atmos. Ocean. Technol.*, 11, 1184-1206, 1994.
- [56] H. Winston, C. Briede, R. Lehtinen, T. Oakley, and J. Nash, "Quantative assessment of improved spectral moments selection algorithms on an 64 MHz clear air Doppler wind profiler," *Vaisala Report*, 2003.
- [57] F.J. Yanovsky, H.W.J. Russchenberg, and C.M.H. Unal, "Retrieval of information about turbulence in rain by using Doppler-polarimetric Radar," *IEEE Trans. Microw. Theory Tech.*, 53, 444-450, 2005.
- [58] A. Zahrai and D. S. Zrnić, "The 10-cm-wavelength polarimetric weather radar at NOAA's National Severe Storms Laboratory," *J. Atmos. Oceanic. Technol.*, 10 (5), pp. 649-662, 1993.
- [59] P. Zhang, A. Ryzhkov and D. Zrnić, "Detection of Birds and Insects Using Polarimetric Radar Observations," *NEPDT Fourth Quarterly Report* P5.13, 2004.
- [60] P. Zhang, S. Liu, and Q. Xu, "Identifying Doppler velocity contamination caused by migrating birds," *J. Atmos. Oceanic. Tech.*, 22, 1105-1113, 2005.
- [61] D.S. Zrnić, "Simulation of weather like Doppler spectra and signals," *J. Applied Meteor.*, 14, 619-620, 1975
- [62] D.S. Zrnić, N. Balakrishnan, A.V. Ryzhkov, and S.L. Durden, "Use of Copolar Coefficient for Probing Precipitation at Nearly Vertical Incidence," *IEEE Trans. on Geosci. and Remote Sensing*, 32(4), 740-748, 1994.

- [63] D.S. Zrnić and R.J. Doviak, "Matched Filter Criteria and Range Weighting for Weather Radar," *IEEE Trans. on Aerospace and Electronic Systems*, 14(6), 925-930, 1978.
- [64] D.S. Zrnić, V. Melnikov, and A.V. Ryzhkov, "Correlation coefficients between horizontally and vertically polarized returns from ground clutter," Submitted to the *Jour. Atmos. Oceanic Technol.*, 2005.
- [65] D.S. Zrnić, V. Melnikov, and J.K. Carter, "Calibrating the differential reflectivity on WSR-88D," Proc. 32<sup>nd</sup> *Int. Conf. on Radar Meteorology*, Albuquerque, NM, Amer. Meteor. Soc., 4R-1, 2005.
- [66] D.S. Zrnić, R. Raghavan and V. Chandrasekar, "Observation of Copolar Correlation Coefficient through a Bright Band at Vertical Incidence," *J. of Applied Meteorol.*, 33(1), 45-52, 1994.
- [67] D.S. Zrnić and A.V. Ryzhkov, "Observation of Insects and Birds with Polarimetric Radar," *IEEE Trans. on Geosci. and Remote Sensing*, 36(2), 661-668, 1998.
- [68] D. S. Zrnić and A.V. Ryzhkov, "Polarimetry for Weather Surveillance Radar," *Bulletin Amer. Meteor. Soc.*, 80(3), 389-406, 1999.
- [69] Department of Commerce, *NEXRAD Technical manual*. Revision B, 1998.
- [70] Accu-Weather, *NEXRAD Doppler Radar Information Guide*, 1995.
- [71] Cornell Laboratory of Ornithology, 2006. Available online at <http://www.birds.cornell.edu/>
- [72] MathWorks, 2006: *MATLAB Technical manual*. Reference, 2006. Available online <http://www.mathworks.com>
- [73] Northern Prairie Biological Resources, 2006. Available online <http://www.npwrc.usgs.gov/resource/othrdata/>
- [74] NatureServe supported by the U.S. Geological Survey, 2006. Available online <http://www.natureserve.org/explorer/ranking.htm>
- [75] Bird Strike Committee USA, 2006. Available online <http://www.birdstrike.org>

## Appendix A. Differential Reflectivity Calibration

The values of the differential reflectivity  $Z_{DR}$  computed on two different systems could be different due to the unbalanced channels. Therefore, it is not equitable to blindly compare the resulting polarimetric variables. Calibrating one system by another (that is considered to be already calibrated) will allow a fair evaluation of the  $Z_{DR}$  values obtained with the two systems.

To calibrate the differential reflectivity, two sets of the  $Z_{DR}$  PPIs are computed using the Sigmet data and RRDA data. Calibration and checking of  $Z_{DR}$  on the Sigmet system is performed daily and monitored continuously, therefore its  $Z_{DR}$  is my basis for comparison. Examples of reflectivity in channel H, velocity in channel H and differential reflectivity computed from Sigmet and RRDA data are shown in Fig.A.1. The PPIs to the right are for RRDA. The PPIs to the left are from Sigmet. The reflectivity PPI computed with RRDA shows less ground clutter than the Sigmet reflectivity, because of better performance of presented spectral adaptive notch filter compared to filter used in Sigmet. The RRDA  $Z_{DR}$  is computed using the same processing steps that Sigmet uses for its polarimetric variables computation. Close ranges might be affected by a ground clutter contamination, while the far ranges could have too low signal to noise ratio. Therefore, a segment stretching from 30 km to 80 km in range and from  $170^\circ$  to  $190^\circ$  in azimuth is chosen to compare the differential reflectivity values of the two systems. The chosen portion is indicated on the differential reflectivity PPI with a dashed line. The histograms of the selected sectors indicate that the RRDA values are 2.9 dB lower than those of the Sigmet (Fig.A.2). Consequently, I add this constant to all computed  $Z_{DR}$  values.

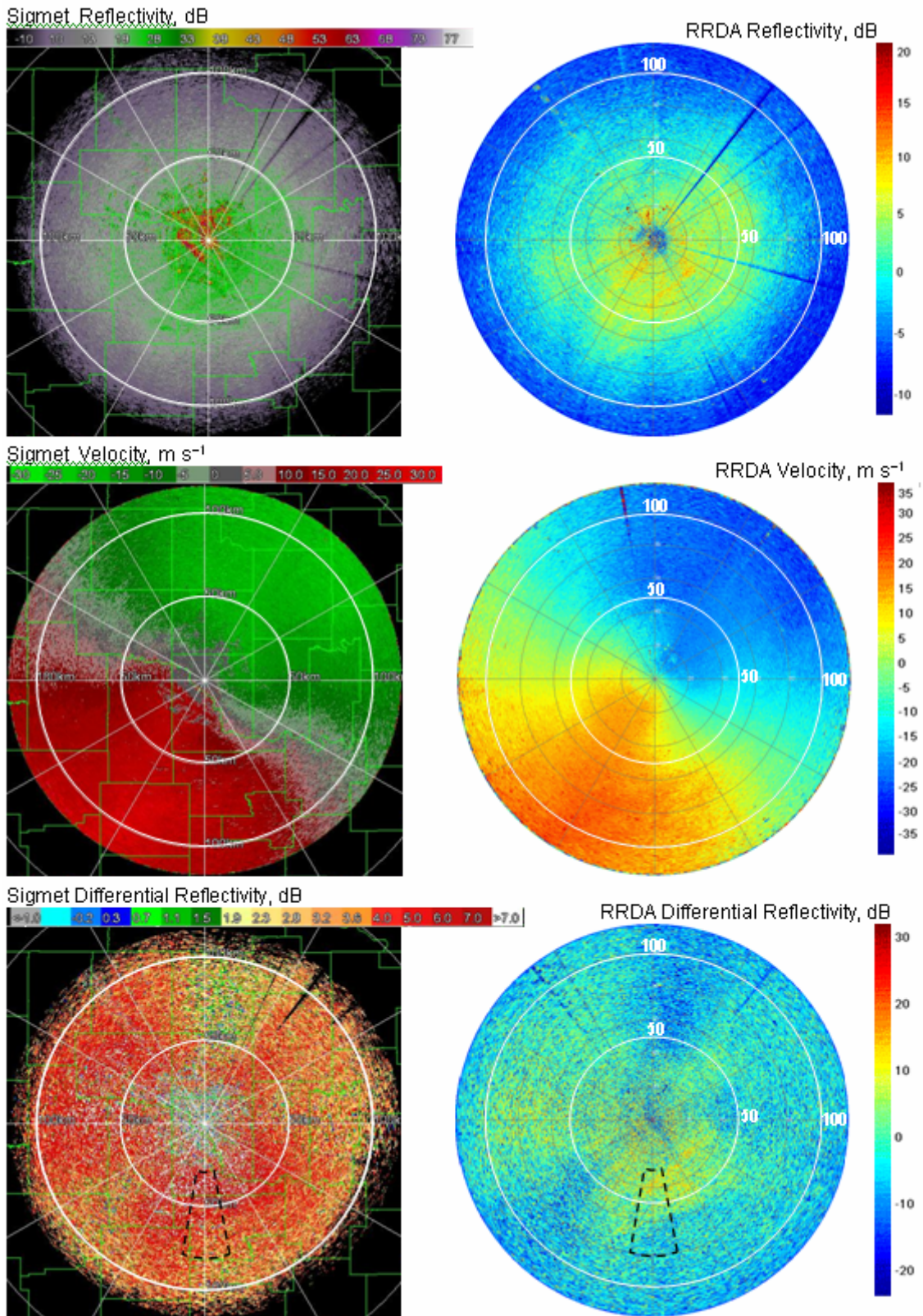


Figure A.1. Comparing PPIs computed from Sigmet and RRDA data

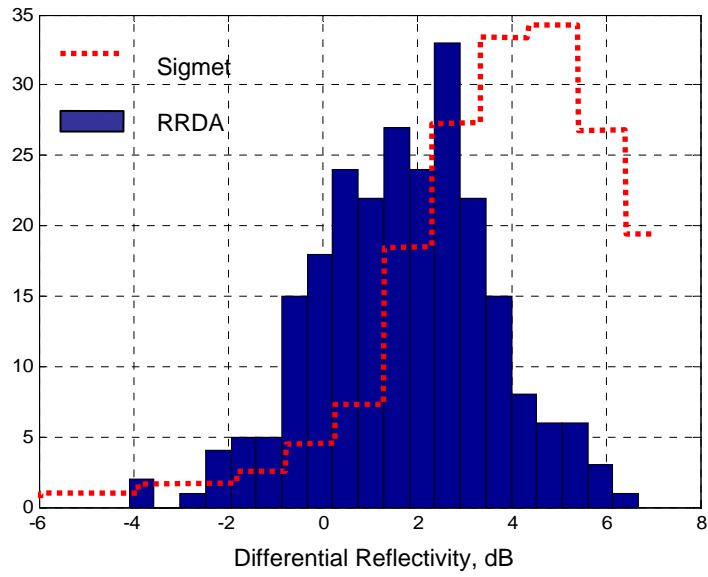


Figure A.2. Comparing the histograms of the chosen segment of the differential reflectivity computed for Sigmet data and RRDA data of the same event.

## Appendix B. System Phase Computation

Zrnich and Ryzhkov (1998) reported that the insects have differential reflectivity between 2 and 9 dB and the differential phase of about 25 degree. They used the Cimmaron radar to attain these results. The phase is specified relatively to the system phase. In order to compare phase measurements obtained with the different radars, it is necessary to correct computed phases with the appropriate system phases. Table B.1 summarizes the available phase information for the mentioned receivers

Table B.1

Radar	Phase span, degrees	System phase, degree
Cimmaron	-80 ° ...100°	-54°
KOUN Sigmet	-180°..180°	-158°
KOUN RRDA digital receiver	-180°..180°	-168° is estimated below

The phases in Cimmaron radar are confined to the interval from -80 to 100 degrees with the system phase -54 degree. The KOUN (Sigmet) phase has twice the span of the Cimmaron, from -180 to 180 degrees, with a system phase -158 degree. The KOUN RRDA digital receiver has a separate connection, different cables and, therefore, a different system phase. How to find the system phase of the KOUN digital receiver? According to Zrnich (2005) the following steps are performed: (a) the reflectivity PPIs for horizontal and vertical polarizations are computed; (b) all reflectivity values below 30dBZ are ignored; (c) the differential phase is computed using Equation (2.11); (d) histogram of the differential phase is used to estimate the system phase. Apparently there is a large number of resolution volumes that display greater than 30 dB reflectivity

values in clear air conditions. Most of the high reflectivity resolution volumes are located at ranges below 20 km as shown in Fig. C.1 and are returns from ground scatterers.

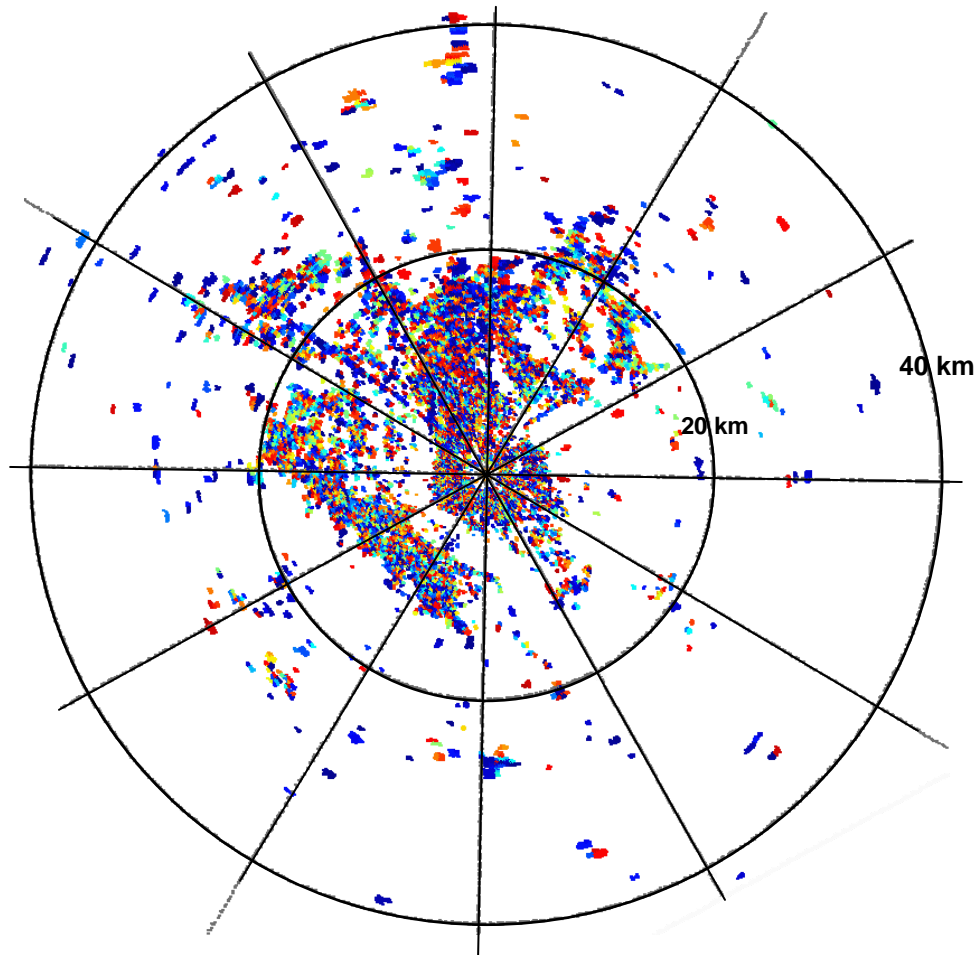


Fig. C.1. Resolution volumes with reflectivity greater than 30 dB in clear air conditions

The histogram of the reflectivity values exceeding 30 dB is shown in Fig. C.2. The broad peak corresponds to the system phase  $-168^\circ$ . The narrow peak at  $98^\circ$  is a mystery phase leak from the first range gate. The narrow peak in the histograms can be eliminated if processing skips first range gate (Fig C.3). It is interesting to point that the

## Appendix C. Cross spectrum vs. copolar correlation spectral density

Cross spectrum analyses are used to determine the relationship between two time series as a function of frequency (Hartmann 2006). For example, if two time series have peaks at the similar frequency, than there might be coherent modes at the particular frequencies, and these periodicities (the peaks) are related in phase.

The cross spectrum is found by  $H^*(v_k) \cdot V(v_k) = S_{hv} = S_{HV}(v_k)$ . It is not normalized. Therefore the argument of the cross spectrum at each  $v_k$  is  $\arg[S_{HV}(v_k)] \equiv \delta(v_k)$ . However, the  $S_{HV}(v_k)$  is not equivalent of  $\rho_{hv}$ . By normalizing the cross spectrum one can get power distribution function of the cross spectrum

$$Density\_PDF = \frac{S_{HV}(v_k)}{\sqrt{\sum |S_{HV}(v_k)|^2}}$$

Evaluation of the correlation coefficient, on the other hand, requires at least two adjacent coefficients (see eq. 6.2). The estimate derived from three spectral coefficients

$$\rho_{hv}(v_k) \cong \frac{\sum_{k=1}^3 S_{HV}(v_k)}{\sqrt{\sum_{k=1}^3 |S_{HV}(v_k)|^2}}$$

does not provide maximum spectral resolution (compared to 2 spectral coefficients) but allows to avoid centering spectral estimate in-between the adjacent frequency locations.

## **Appendix D. Change in PPIs over time (up to 117 km range)**

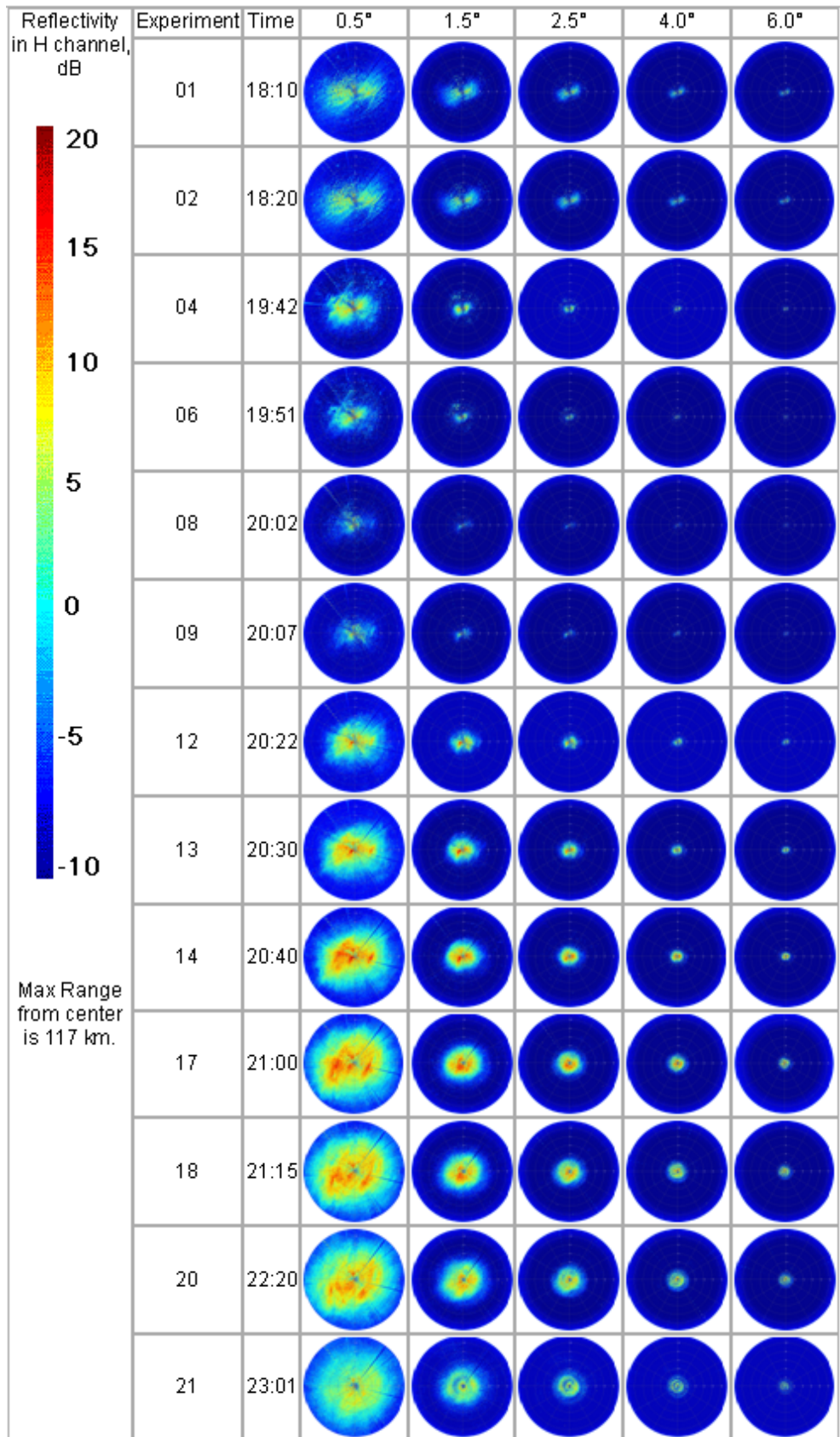
Tables with thumbnails of plan position indicator images are provided here. The overall change over time for each parameter can be observed from these tables. Each thumbnails show 117 km range.

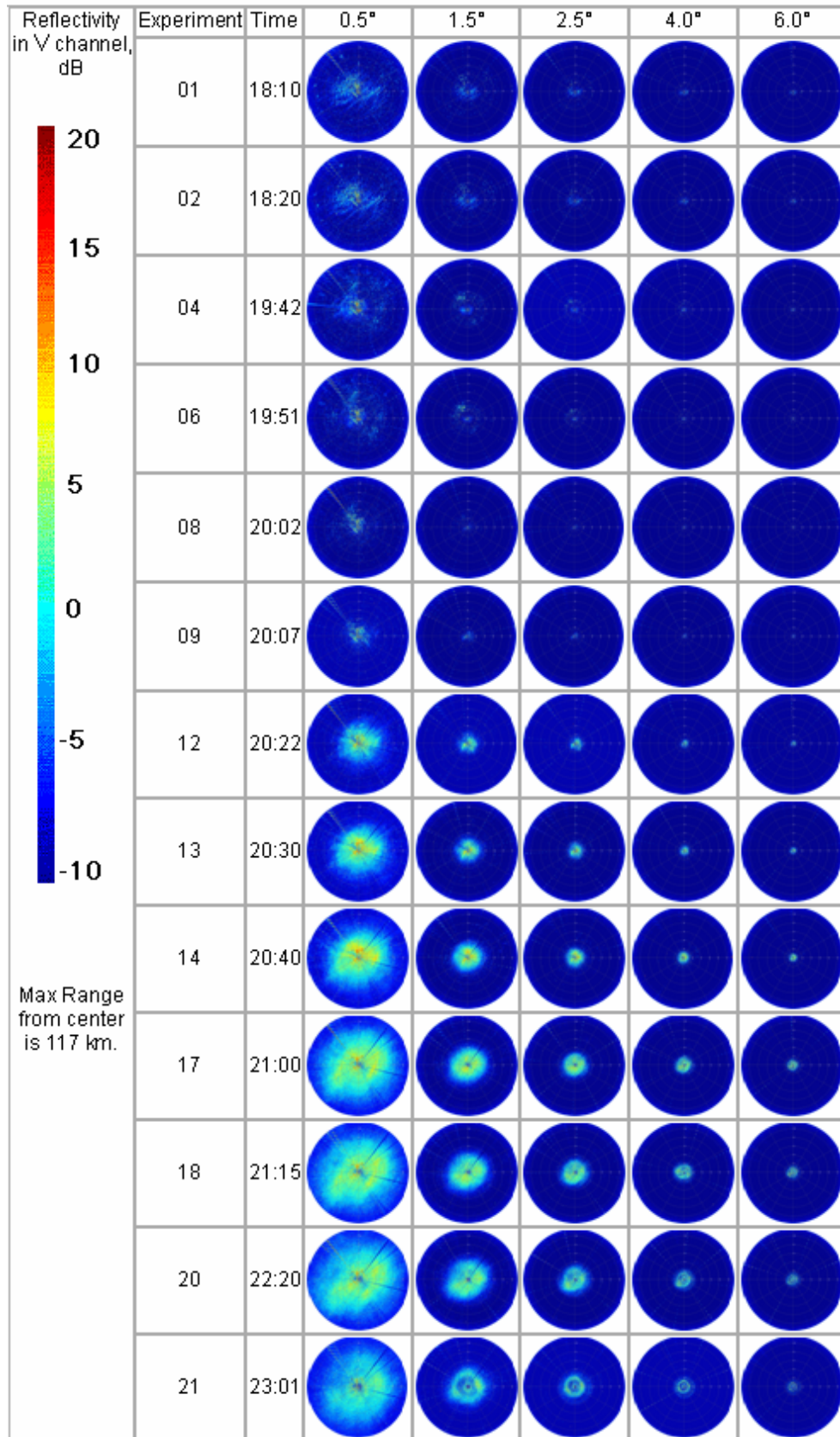
First column in each table names the moment, shows the color scale and states the maximum range of the PPI. Second and third columns show experiment number and local time for the reference. The rest five columns show PPIs at 0.5, 1.5, 2.5, 4 and 6 degrees elevations of the scan, as indicated at the top row of each table.

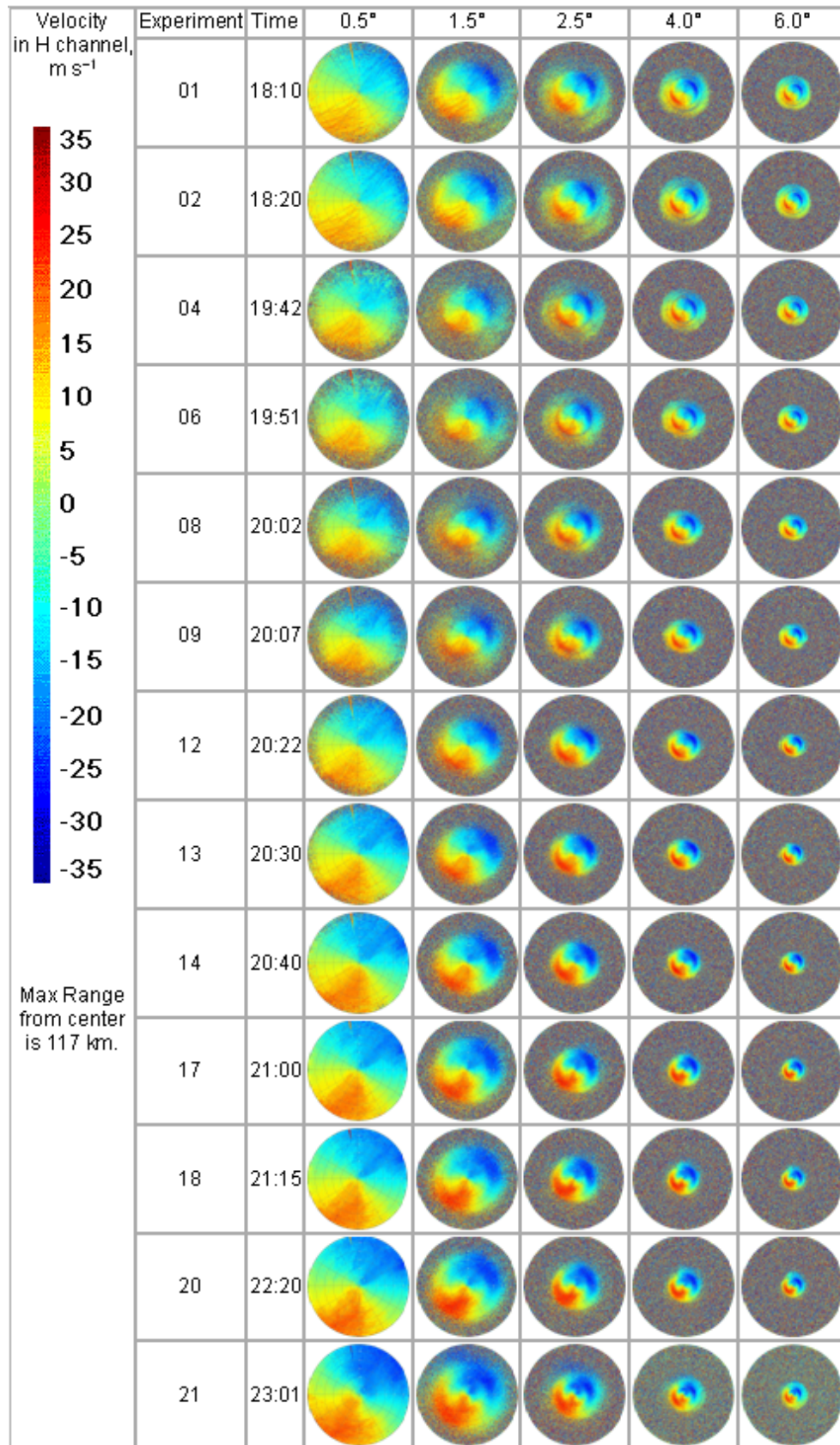
The tables organized in the following order

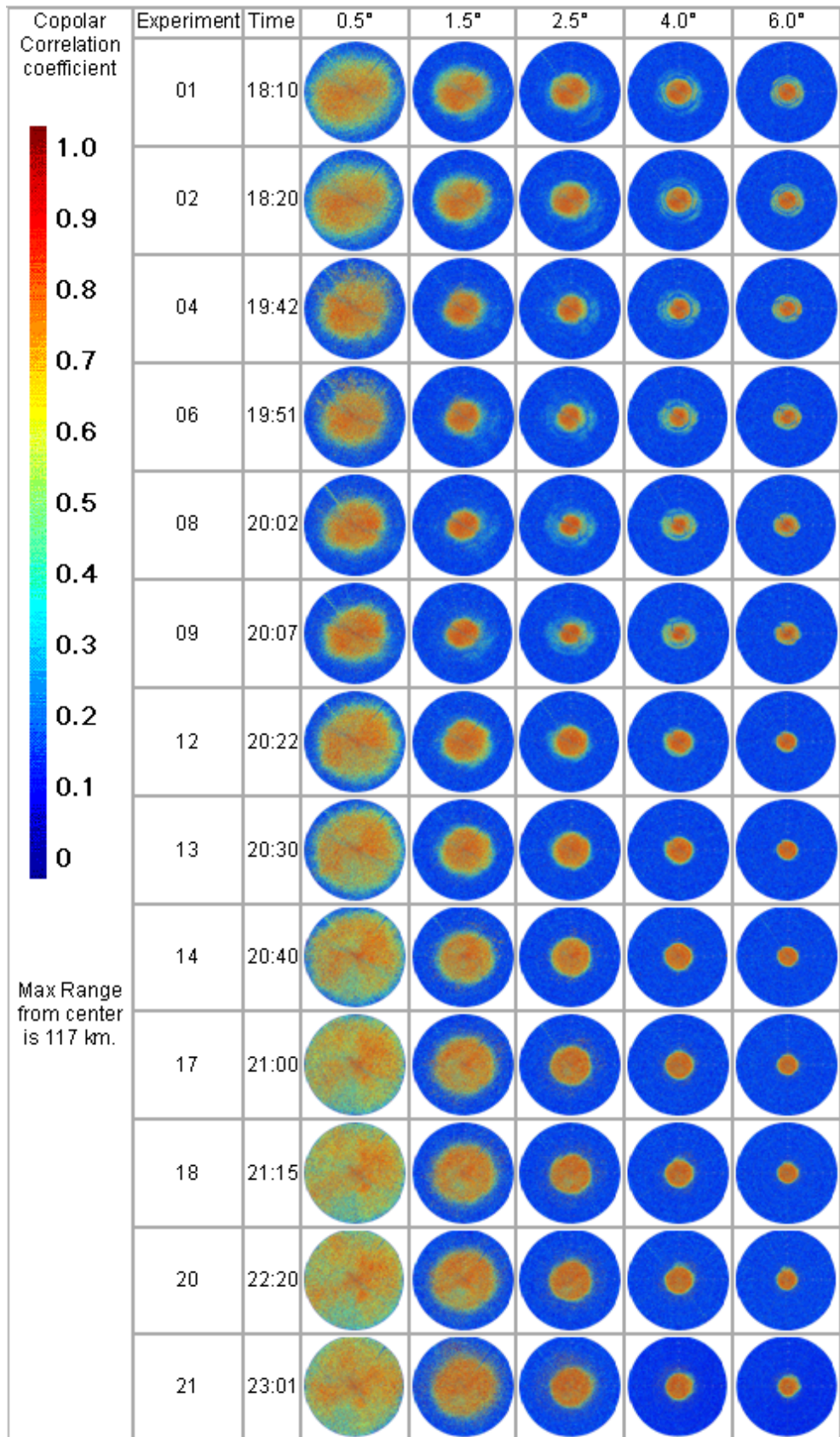
- reflectivity in H channel,
- reflectivity in V channel,
- velocity in H channel,
- copolar correlation coefficient,
- differential reflectivity, and
- backscatter differential phase.

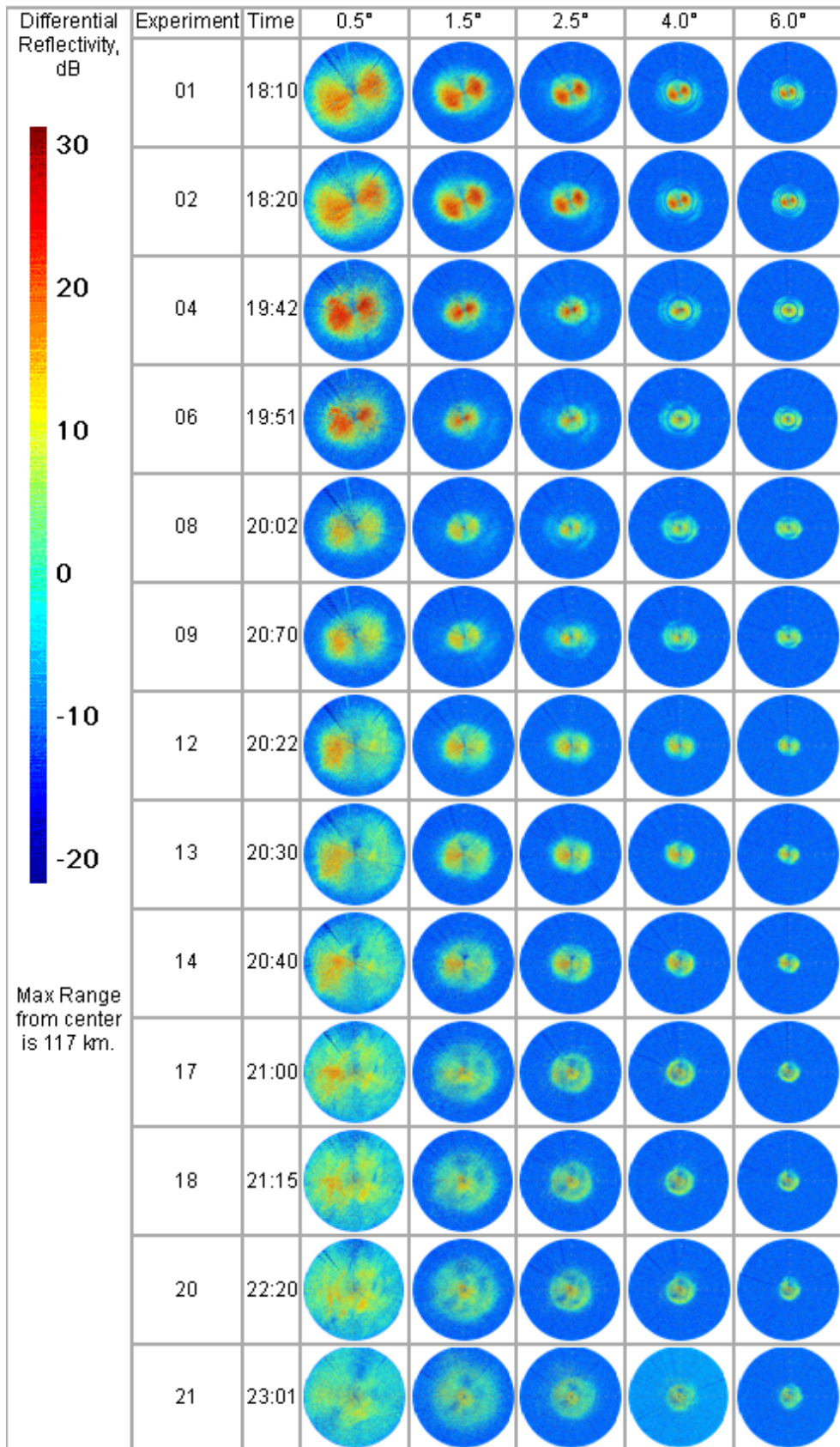
For the times of experiments refer to Table 4.1.

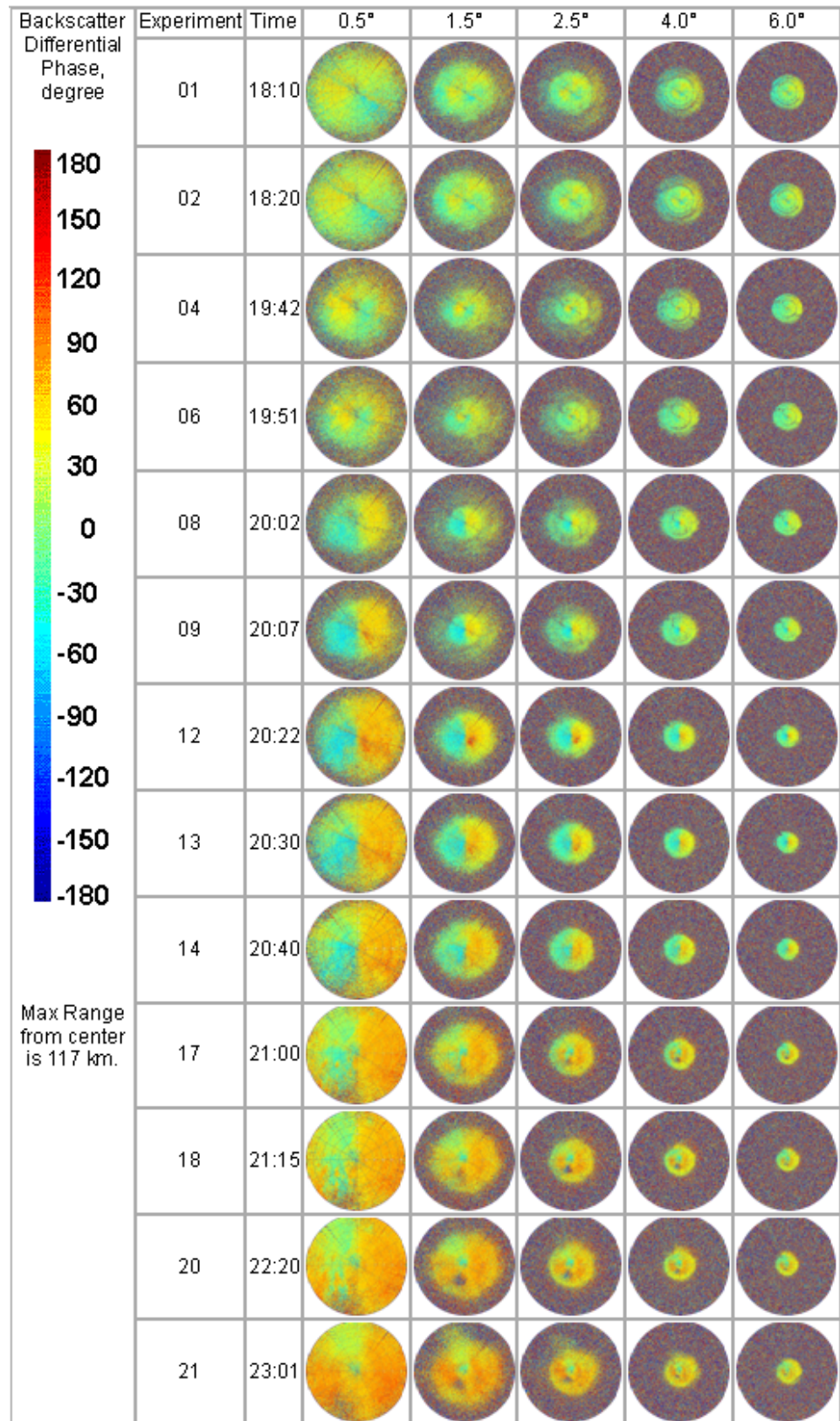








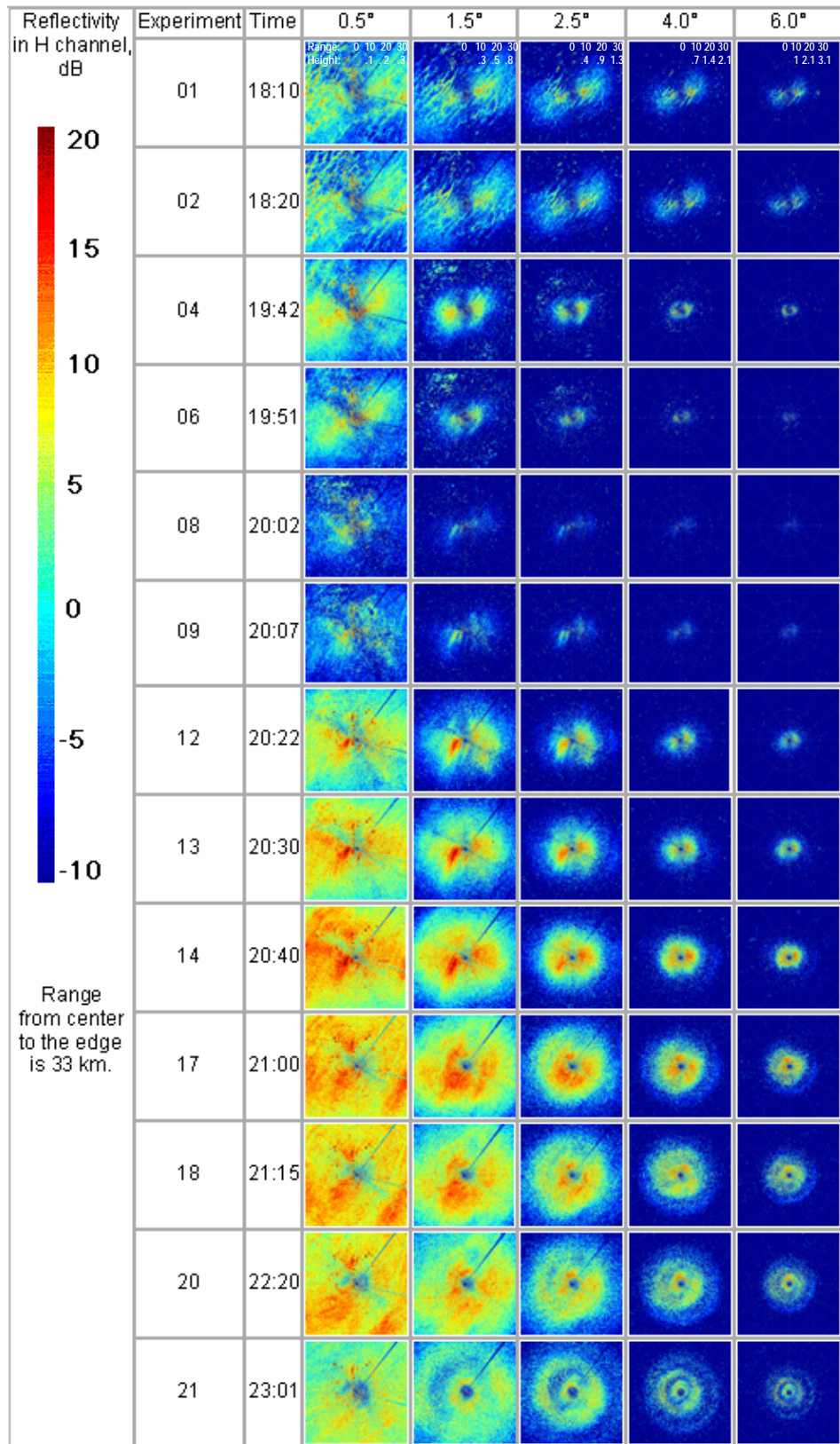


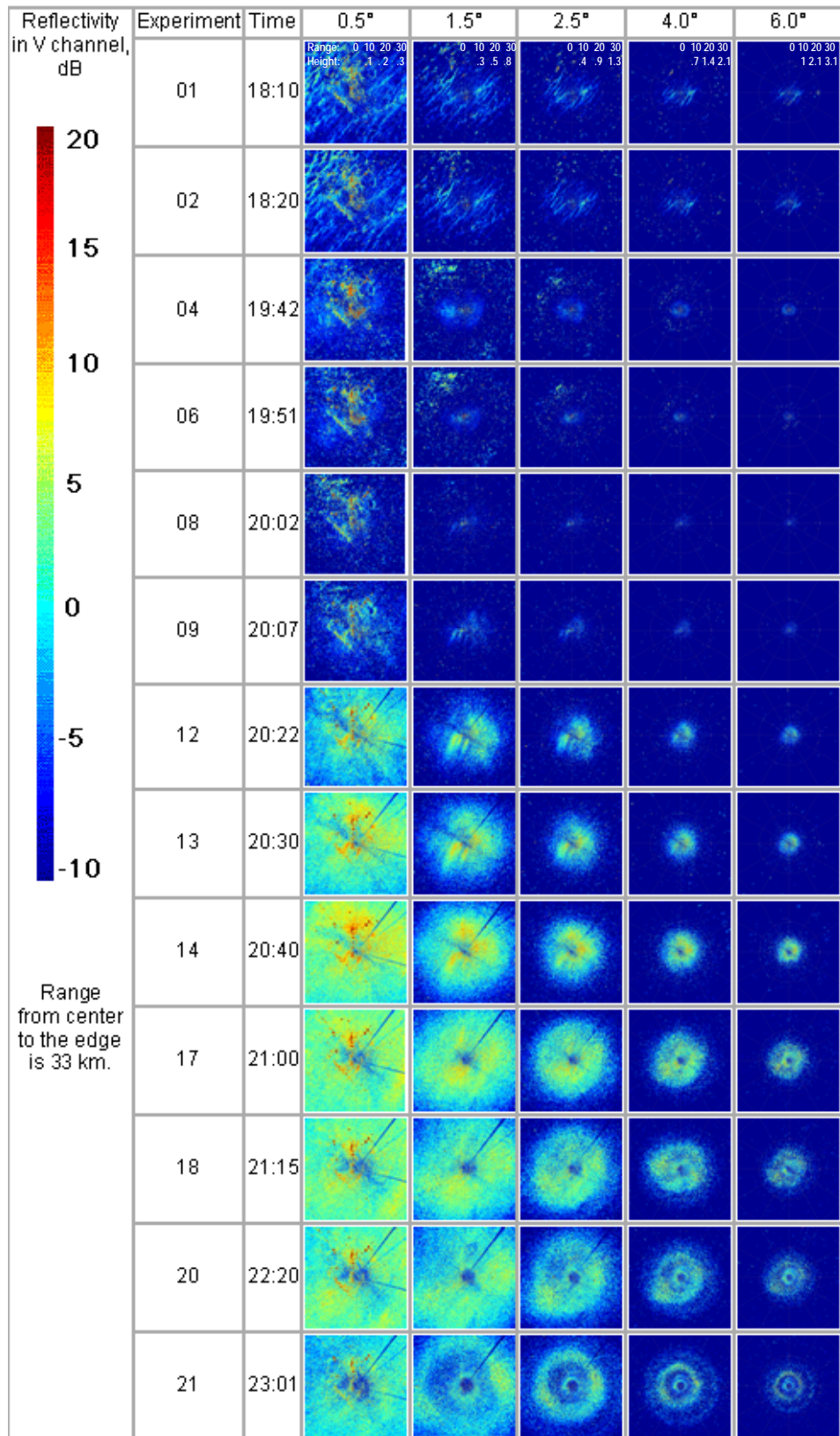


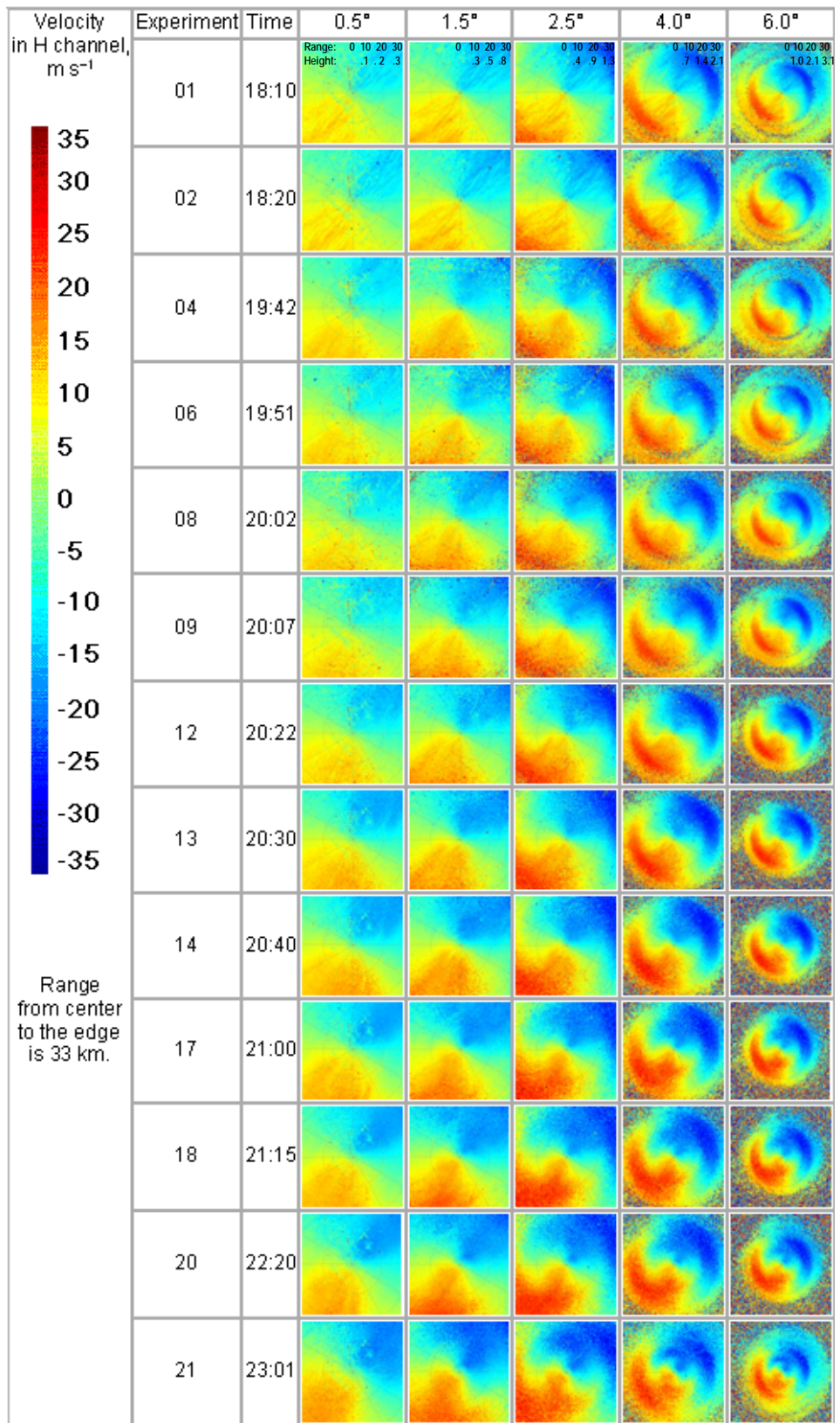
## **Appendix E. Changes in PPIs over time (zoomed)**

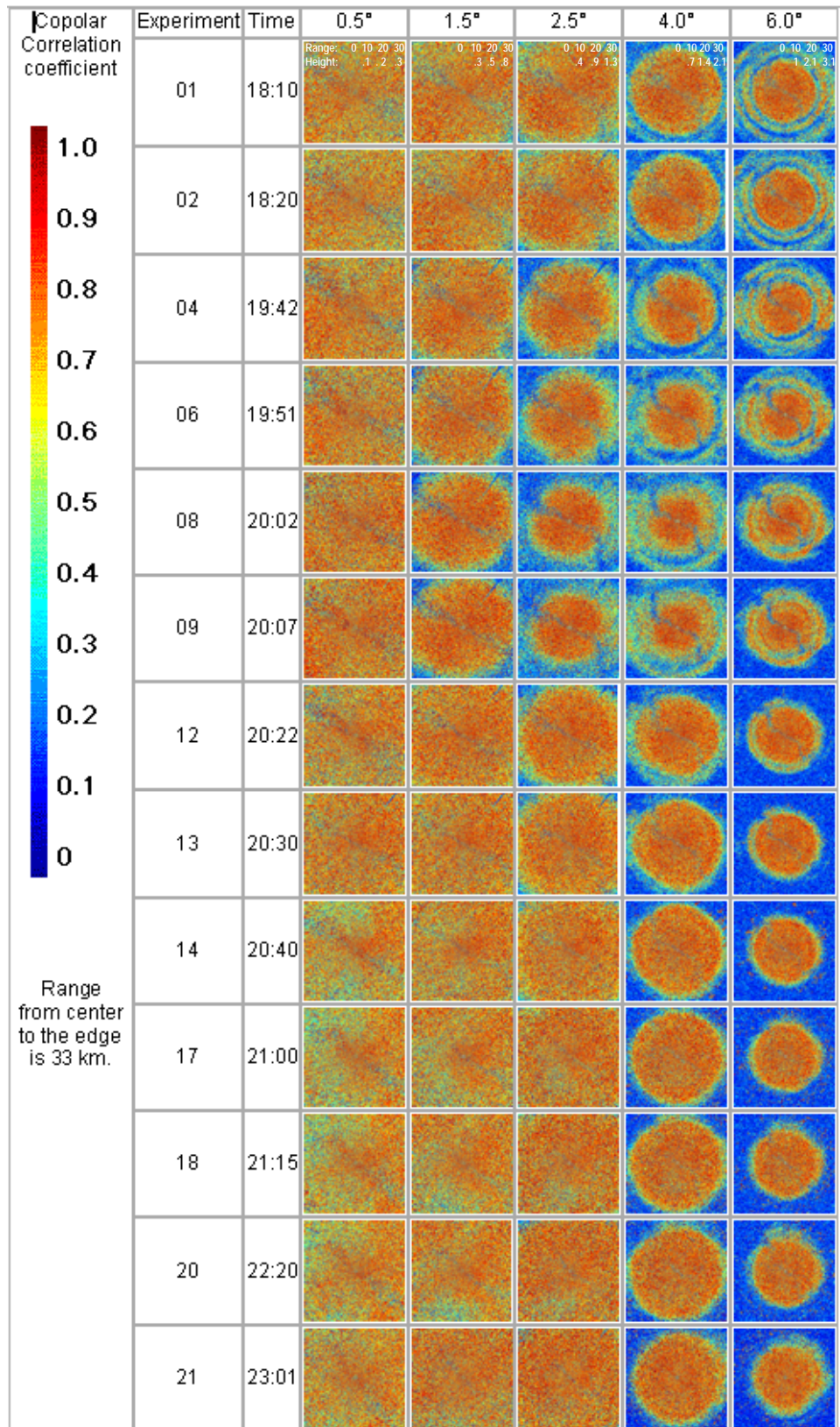
Similar to Appendix D, tables with thumbnails of plan position indicators are provided here. Each thumbnails show 30 km range. The overall change over time for each parameter closer to the radar can be observed from these tables.

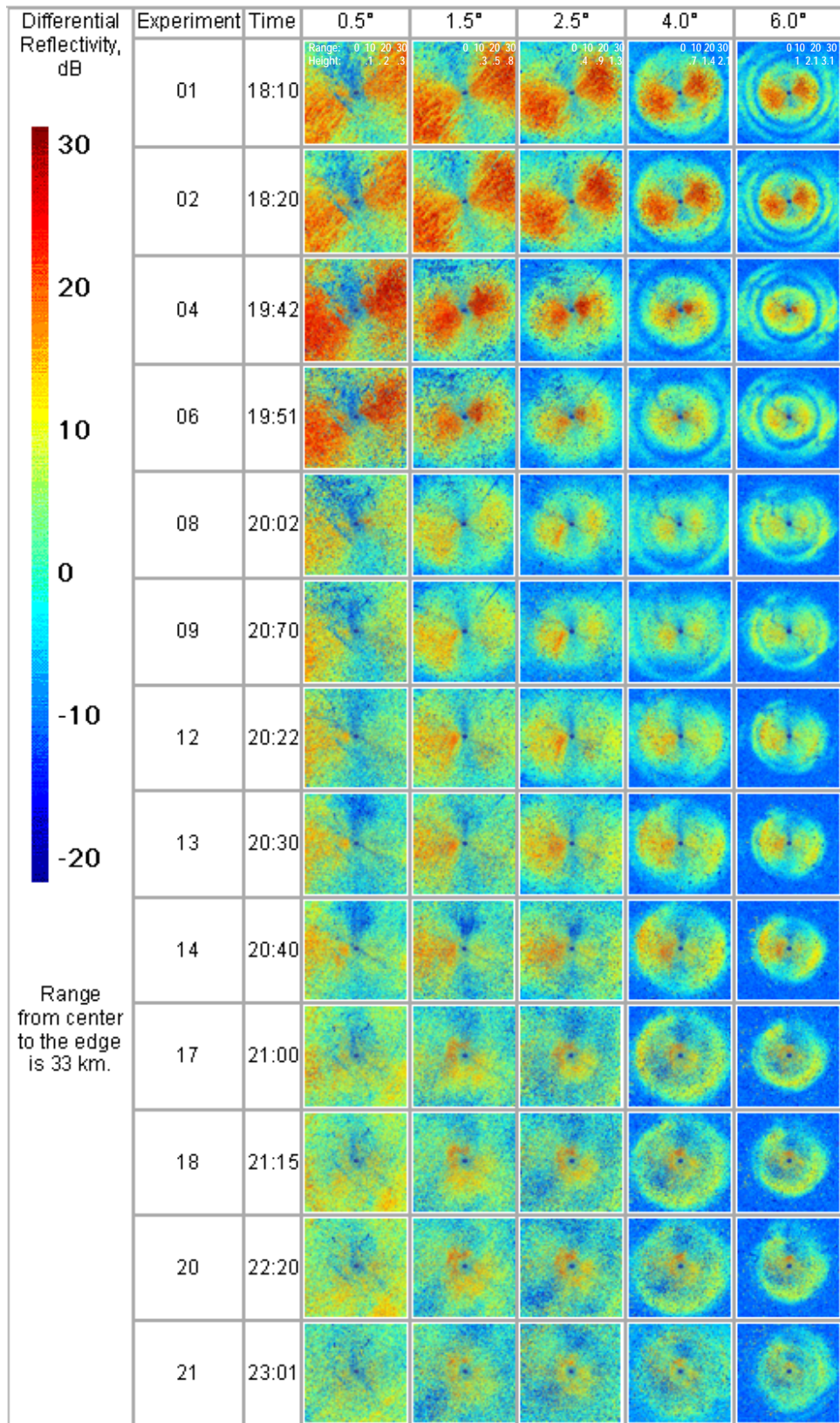
The organization of the tables the same as in Appendix D. The times of experiments are summarized in Table 4.1.

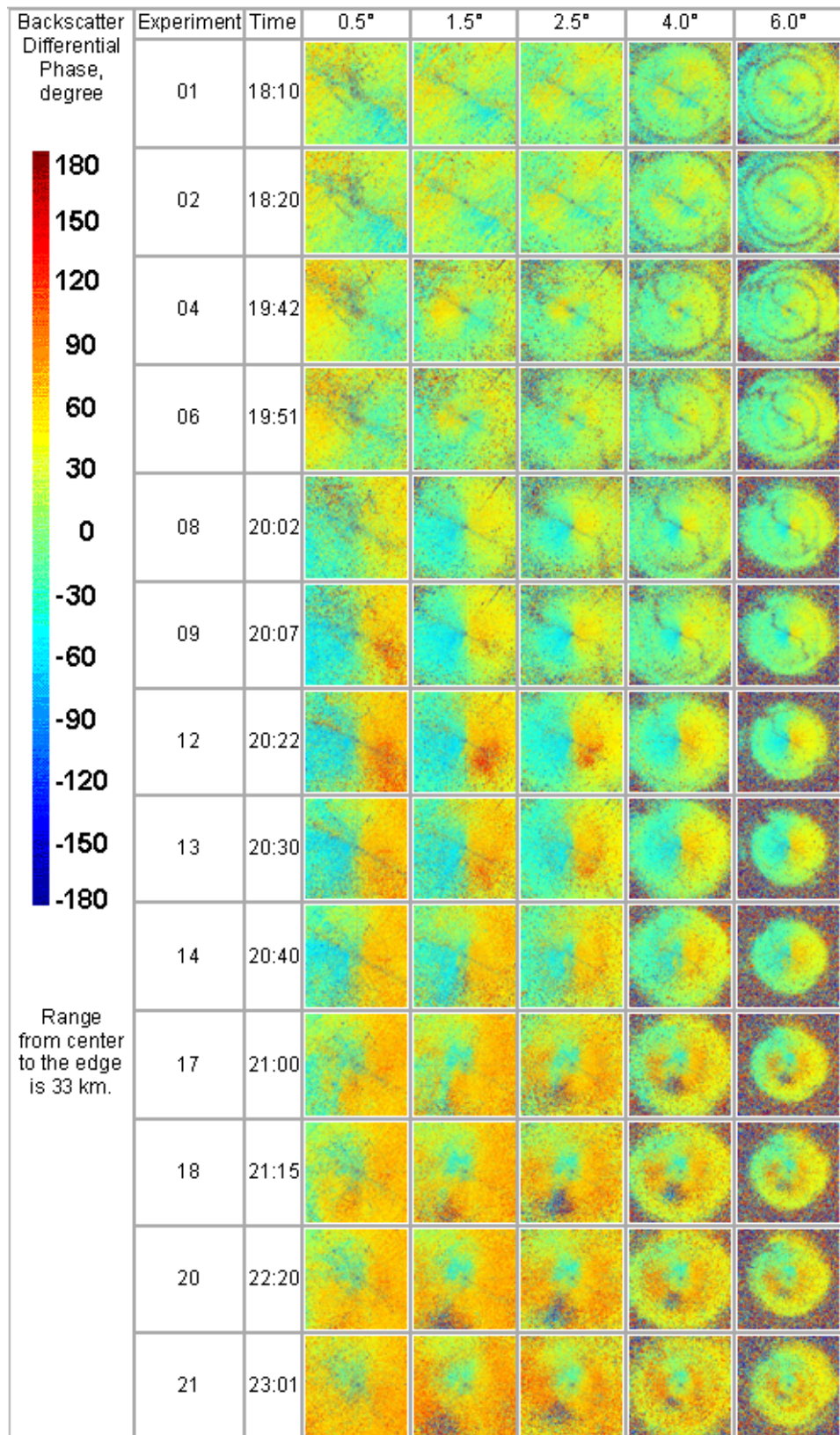












## Appendix F. List of Abbreviations

### General abbreviations

ASL	above sea level
AR, MA	autoregressive and moving average processes
EM	electromagnetic
MUSIC	multiple signal classification
PSD	power spectral density
SNR	signal-to-noise ratio
SVAD	spectral azimuth display
H, V	horizontal and vertical polarization
I-Q	in-phase and quadrature phase components of the echo voltage
PBL	planetary boundary layer
PPI	plane position indicator
RF	radiofrequency
VAD	velocity azimuth display
WSR-88D	weather surveillance radar 1988 Doppler
2D	two dimensional

### Special abbreviations

3DASH	three dimensional azimuthal spectral histogram
$S_h$ SD	power spectral density in H channel
$S_h$ SVAD	spectral VAD of power spectral density in H channel
$Z_{DR}$ SD	spectral density of differential reflectivity
$Z_{DR}$ SVAD	spectral density of differential phase azimuth display
$\rho_{hv}$ SD	spectral density of copolar correlation coefficient
$\rho_{hv}$ SVAD	spectral density of copolar correlation coefficient azimuth display
$\delta$ SD	spectral density of backscatter differential phase
$\delta$ SVAD	spectral density of backscatter differential phase azimuth display

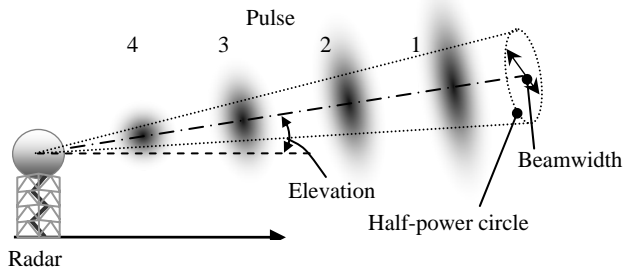


Figure 2.1. Propagation of the radar pulse.

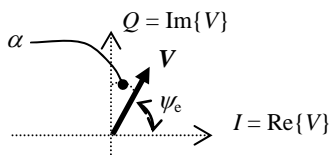


Figure 2.2. Phasor diagram: the Doppler radar receiver detects in-phase I and quadrature-phase Q components of the echo signal  $V$ . I is the real part of the echo voltage  $V$ ; Q is the imaginary part of  $V$ ; and  $\psi_e$  is echo phase.

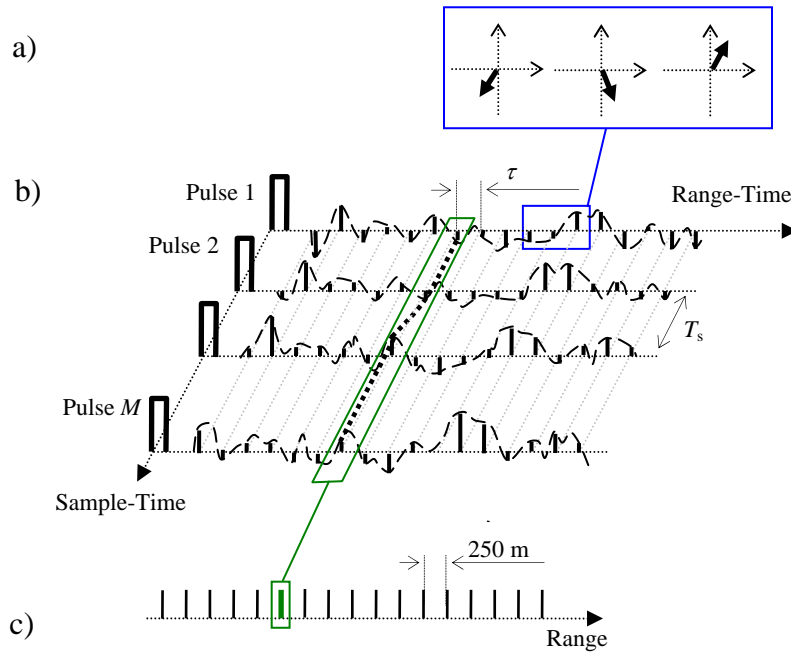


Figure 2.3. A radial of time-series data: a) a sequence of the I-Q samples; b) I-Q samples of backscattered energy for  $M$  pulses; c) radial of spectral moments or polarimetric variables.

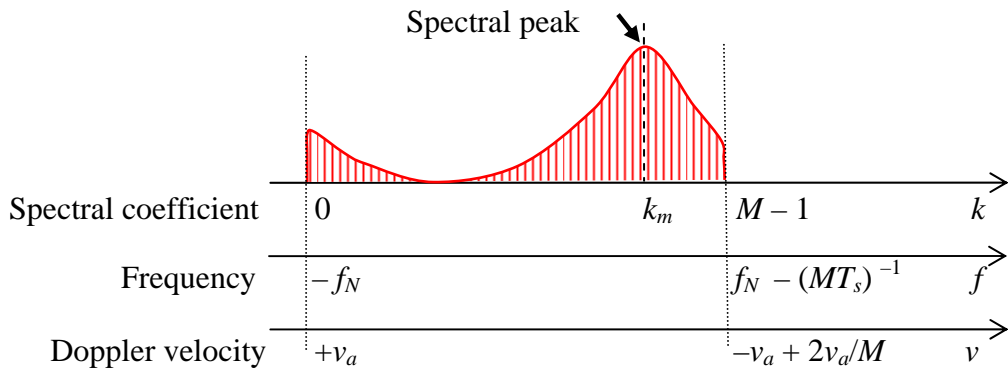


Figure 2.4. Power spectral density

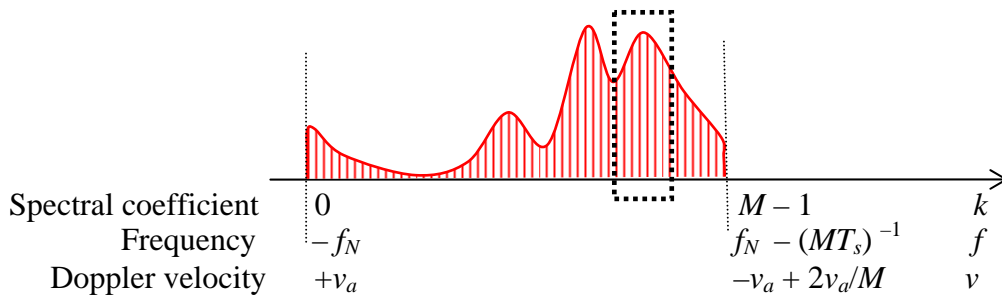


Figure 2.5. Multimodal spectrum

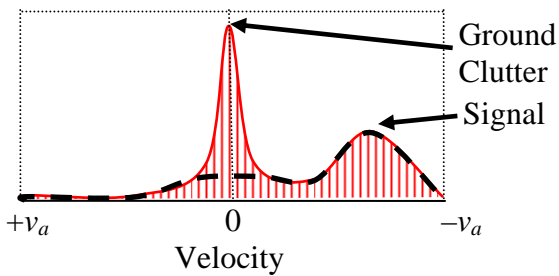


Figure 2.6. Ground Clutter suppression; note the scale from  $v_a$  to  $-v_a$  for simplicity. Contrast this to the scale of DFT discrete values (Figure 2.4, 2.5) where the coefficient stops at  $-v_a + 2v_a/M$ .



Figure 4.1. Dual polarization Doppler research radar KOUN in Norman, OK

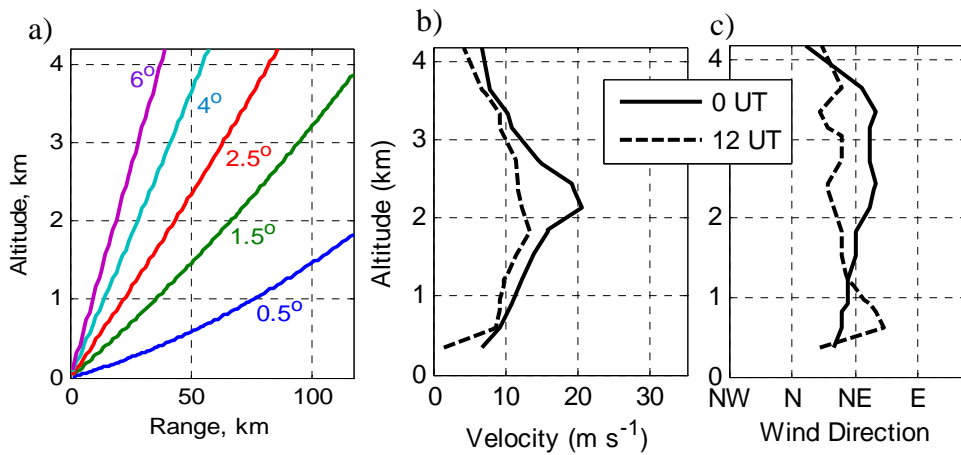


Figure 4.2. In altitude: a) the beam centers of the radar elevation scans; b) vertical profile of wind from the sounding on September 8, 2004 at 0 UT and 12 UT; c) wind direction.

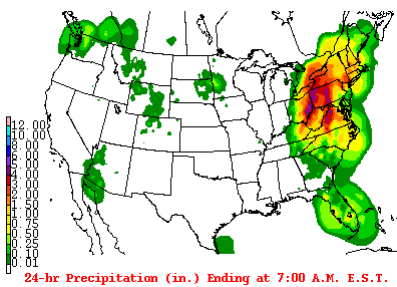


Figure 4.3. A copy of the 24 hour precipitation from the *Daily weather map* ([www.hpc.ncep.noaa.gov/dailywxmap](http://www.hpc.ncep.noaa.gov/dailywxmap)) on September 8, 2004 confirms that there were clear air conditions over Oklahoma.

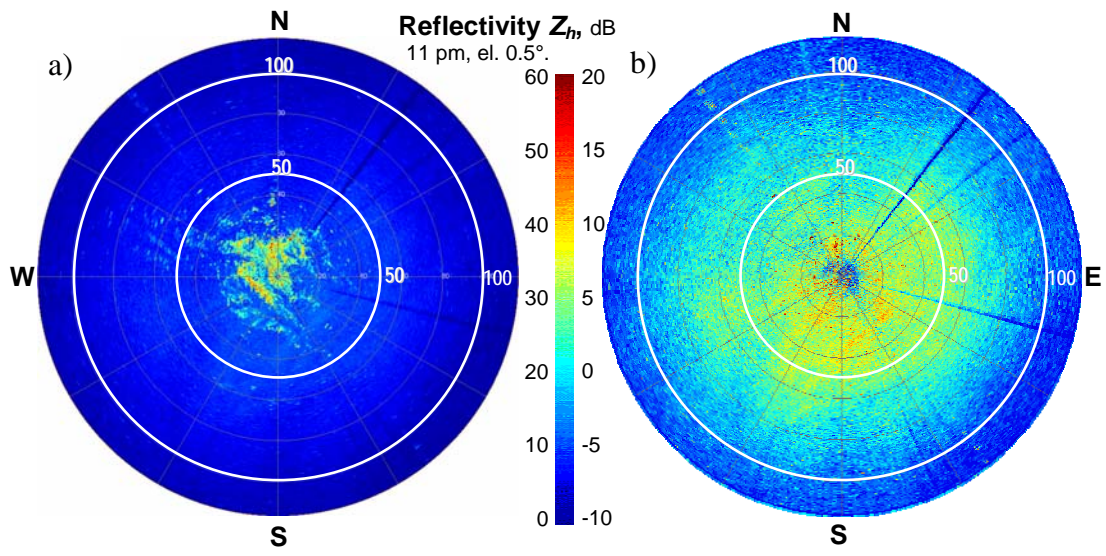


Figure 4.4. Examples of reflectivity in H channel: a) with ground clutter and b) with suppressed ground clutter. The unambiguous range is 117 km.

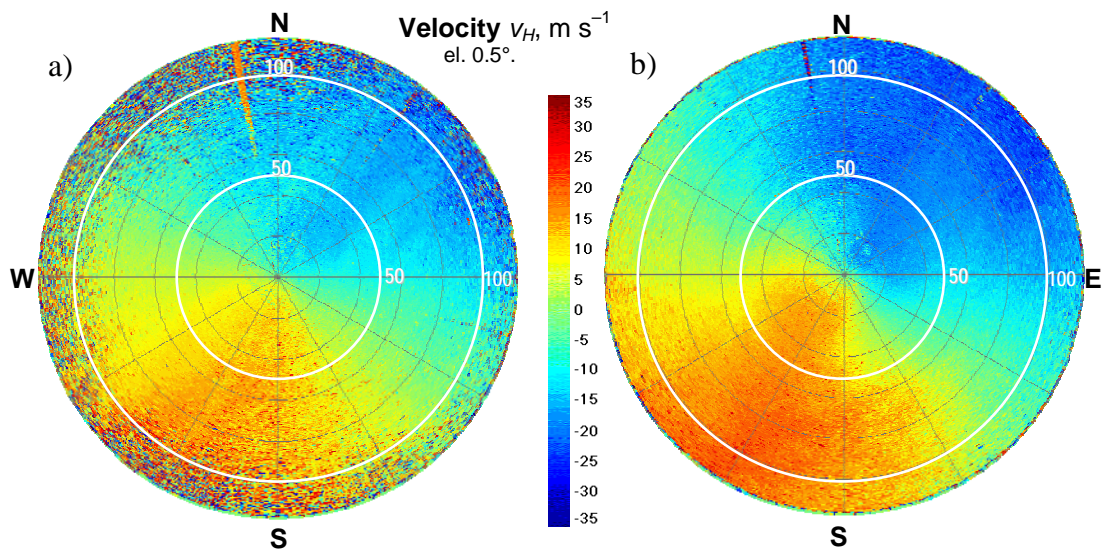


Figure 4.5. Examples of velocity in H channel at a) 8 pm, and b) 11 pm. The wind direction is NNE. The unambiguous range and velocities are 117 km and  $35 \text{ m s}^{-1}$ . Data: September 7 2004, 11 pm, el.  $0.5^\circ$ .

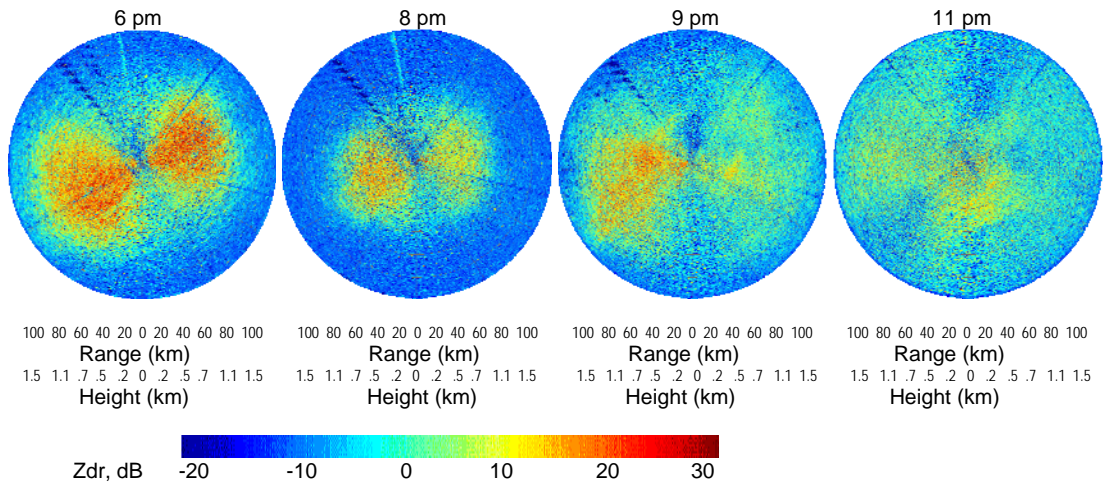


Figure 4.6. The PPIs of the differential reflectivity at elevation  $0.5^\circ$  depict vivid changes in clear air as the evening progresses from 6 pm to 11 pm. Maximum range is 117 km; local time is indicated above each PPI.

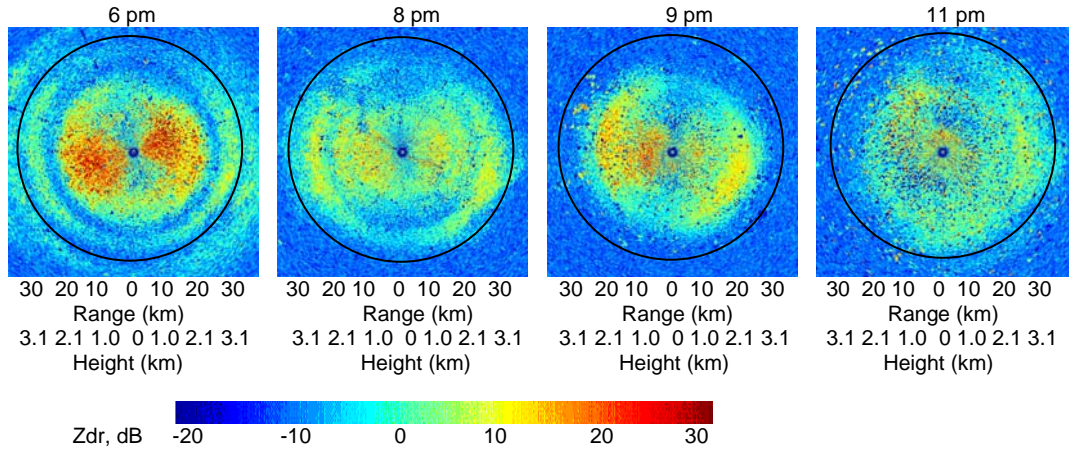


Figure 4.7. Zoomed PPIs of the differential reflectivity at elevation  $6^\circ$  depict changes in clear air as the evening progresses from 6 pm to 11 pm. Range ring indicates 30 km; local time is indicated above each PPI.

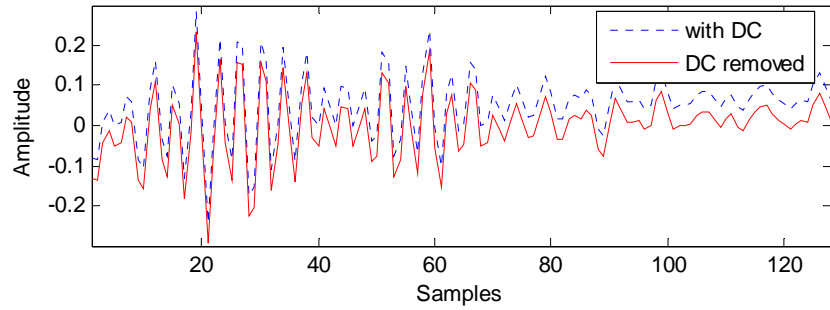


Figure 5.1. Example of the DC correction. Dashed line shows detected signal. Solid line represents corrected for the DC signal. This data is the in-phase component of the H channel signal (11 pm; elevation  $0.5^\circ$ ; azimuth  $180^\circ$ ; range 10 km).

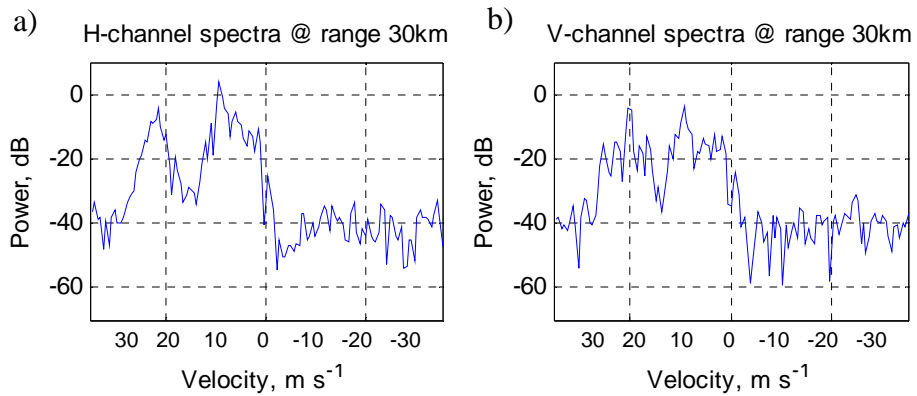


Figure 5.2. Example of power spectral density in a) horizontal and b) vertical channels. Samples are weighted by a Hanning window. Total number of samples is 128. These spectra are from a precipitation-free air with mixed nocturnal biological scatterers (11 pm; elevation  $0.5^\circ$ ; azimuth  $180^\circ$ ; range 30 km;  $\text{SNR}_H = 42$  dB;  $\text{SNR}_V = 35$  dB).

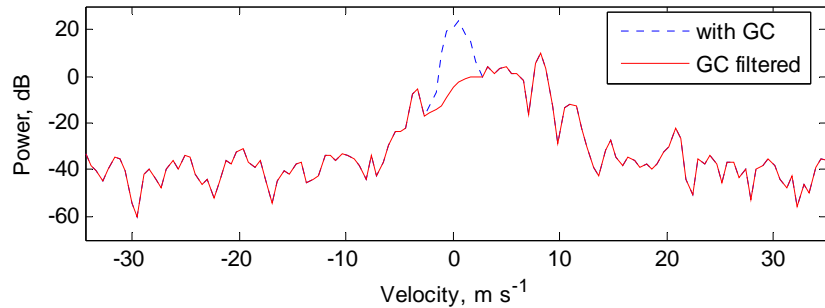


Figure 5.3. Example of the Ground Clutter correction. Dashed line shows detected signal. Solid line represents corrected for DC signal (11 pm, H channel, el.  $0.5^\circ$ ; azimuth  $180^\circ$ ; range 5 km).

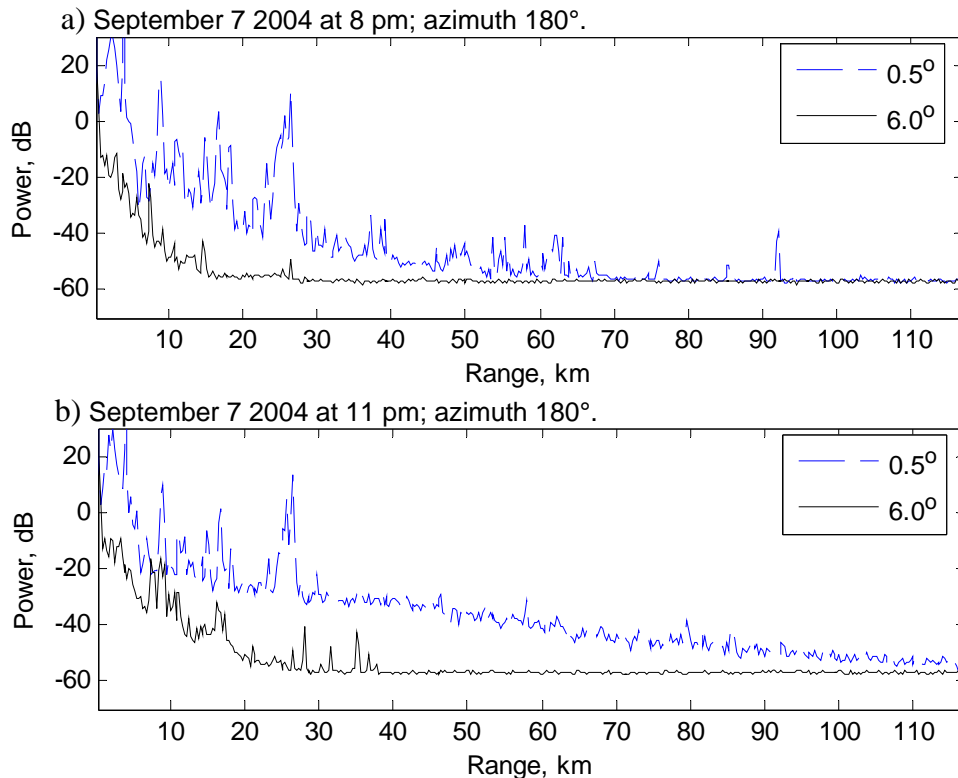


Figure 5.4. Examples of the H signal power in a radial with a) relatively weak clear echo returns, and b) reasonably strong clear echo returns. Dashed and solid lines are used to distinguish radials at elevations  $0.5^\circ$  and  $6^\circ$  respectively. Noise level in both examples is at  $-58$  dB.

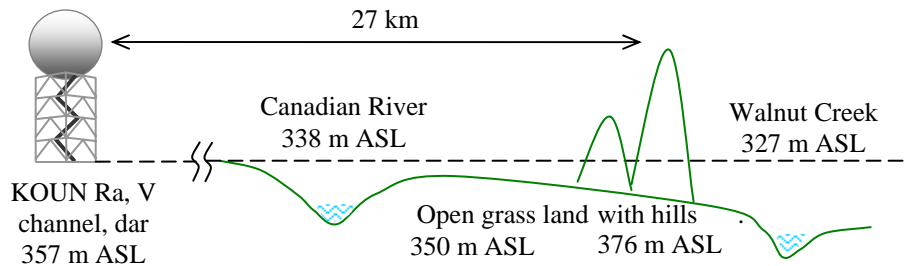


Figure 5.5: A sketch of ground clutter that causes peak at 27 km in Figure 5.4. The KOUN radar is located at 357 m above sea level (ASL) and is schematically shown with a dashed line. The Canadian river ground level is about 20 meters lower and the Walnut Creek ground level is about 30 meters lower than the radar level. The open grass range land situated between the rivers has small hills up to 40 meters above the radar ground level. The echoes from these hills cause large return appearing as a wide peak in Figure 5.4 at the 27 km range.

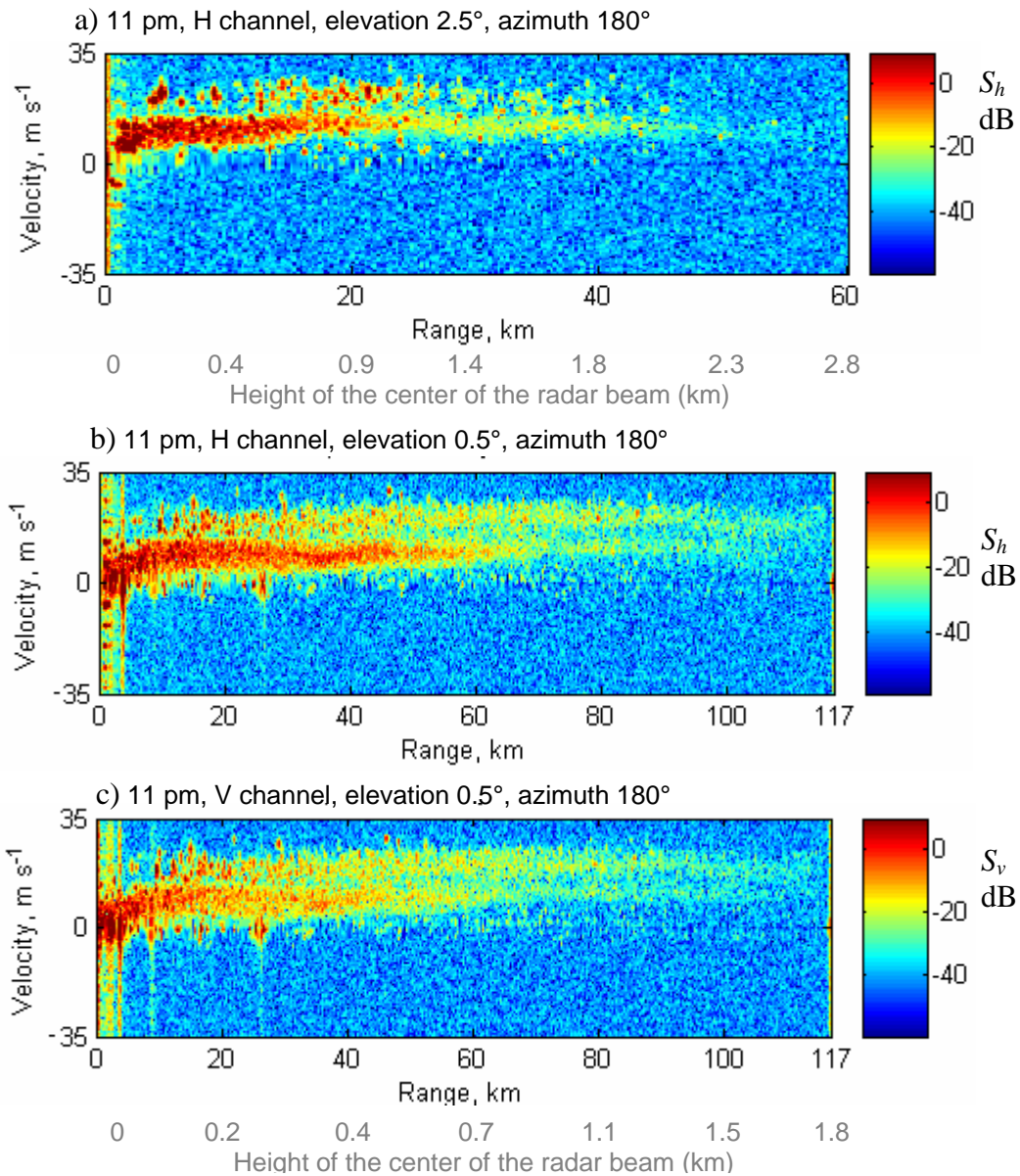


Figure 5.6. Examples of Doppler spectral fields (11 pm, azimuth 180°): a) in H channel at elevation 2.5°, b) in H channel at elevation 0.5°, and c) in V channel at elevation 0.5°. Color scale shows the power in logarithmic units; horizontal axis represents range, and vertical axis represents radial velocity. Two bands with larger than the background powers are evident in all three fields.

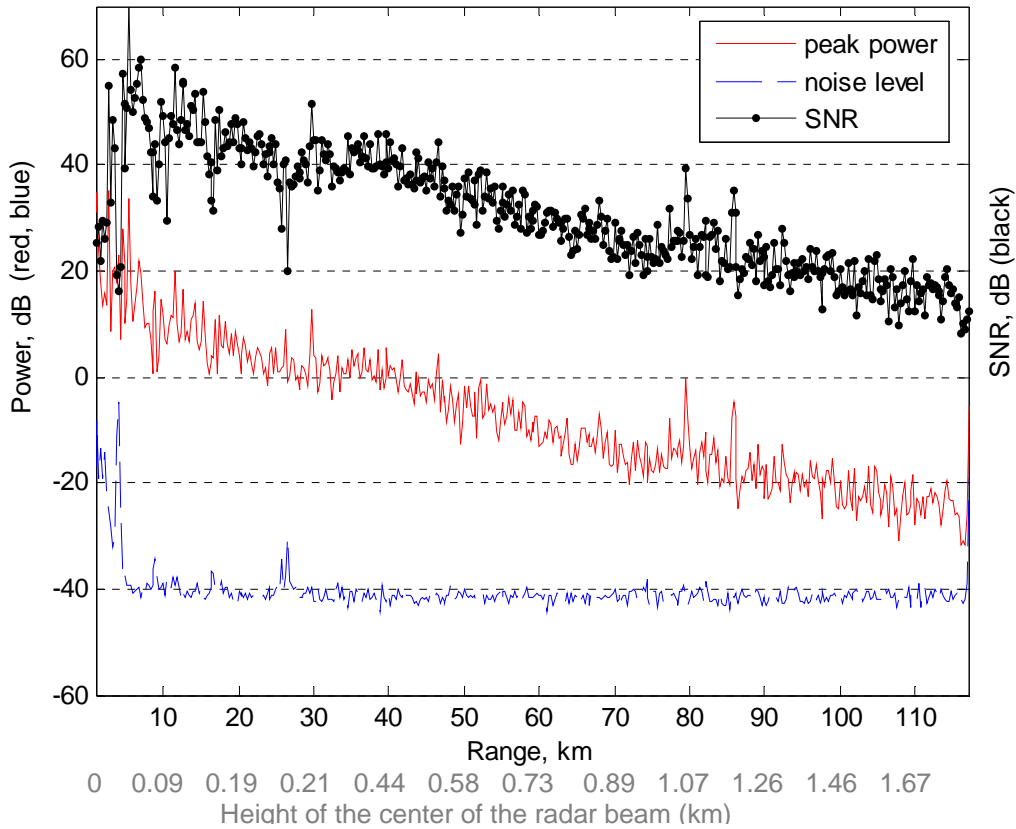


Figure 5.7. Signal peak power to noise ratio computed from spectral fields along a radial. The spectral field image is divided into parts with signal and parts with noise alone; signals having velocities with absolute values smaller than  $2 \text{ m s}^{-1}$  are not considered. The maximum of the signal part is the peak power, indicated with a solid line. The mean of the noise part is the noise level, shown with a dashed blue line. The solid red line with a dot marker is used to plot the ratio of the peak power to noise level in a radial (11 pm; H channel, elevation  $0.5^\circ$ ; azimuth  $180^\circ$ ).

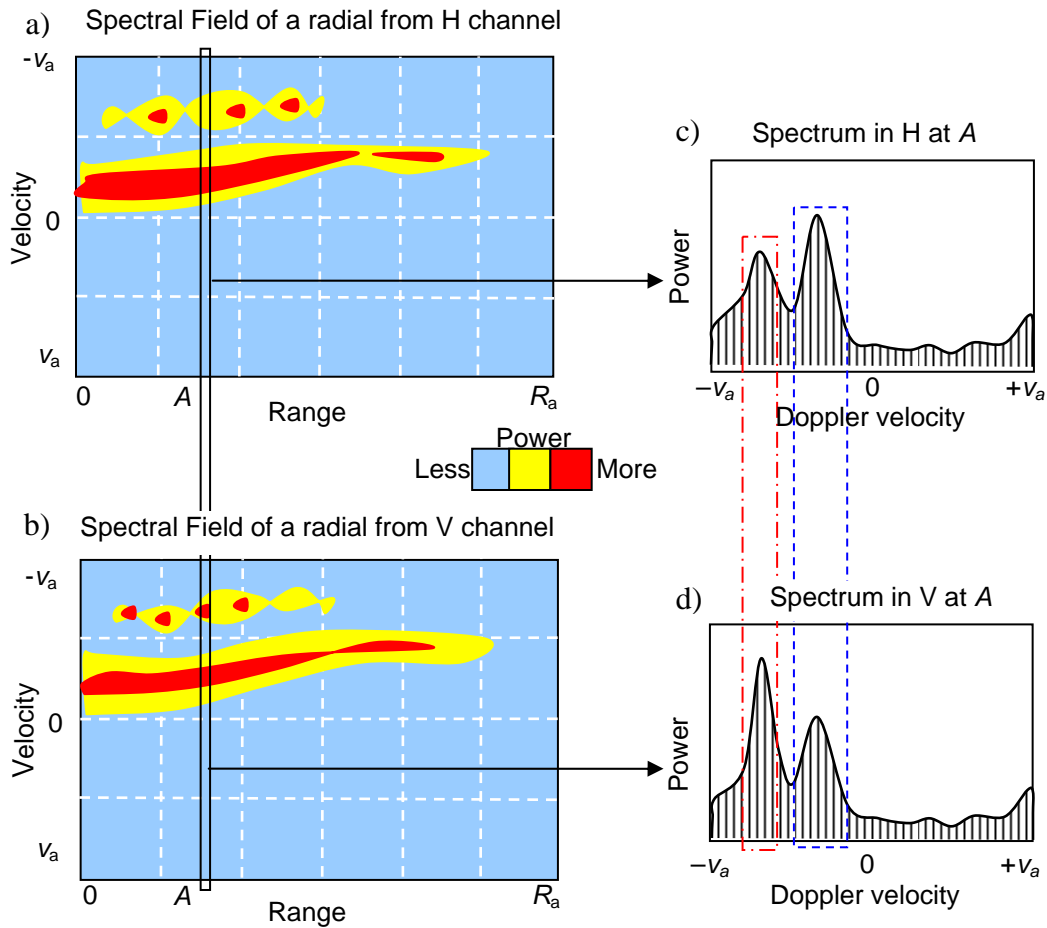


Figure 5.8. Example illustrating how portions of spectral coefficients can be used to identify scatterer type. Spectral fields in a radial from a) vertically and b) horizontally polarized waves are expected to expose a continuous path from wind blown insects and a blotchy path and/or blobs from contaminants, such as migrating birds. Doppler spectrum at some range  $A$  in each c) horizontal and d) vertical channel is expected to have 2 peaks. The peaks are likely to be located at similar radial velocities. However, the powers and spectral widths of these peaks are apt to be different. The dashed-dotted and dashed rectangles enclose spectral coefficients around two such peaks. Polarimetric variables computed only for the spectral coefficient enclosed in the rectangles would reflect the corresponding scatterers' polarimetric features.

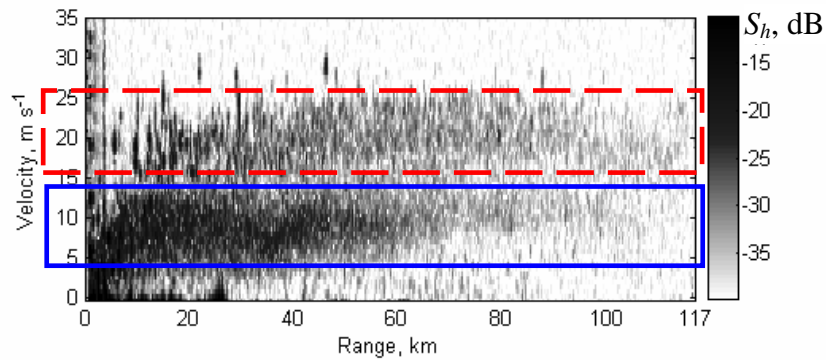


Figure 5.9. Chosen portions of spectral coefficients identify scatterer type in a radial (11 pm, H channel, elevation  $0.5^\circ$ ; azimuth  $180^\circ$ ). There are two bands whose polarimetric properties are of the main interest. The solid and dashed rectangles enclose contributors with radial velocities from  $2 \text{ m s}^{-1}$  to  $13 \text{ m s}^{-1}$  and from  $13 \text{ m s}^{-1}$  to  $25 \text{ m s}^{-1}$ .

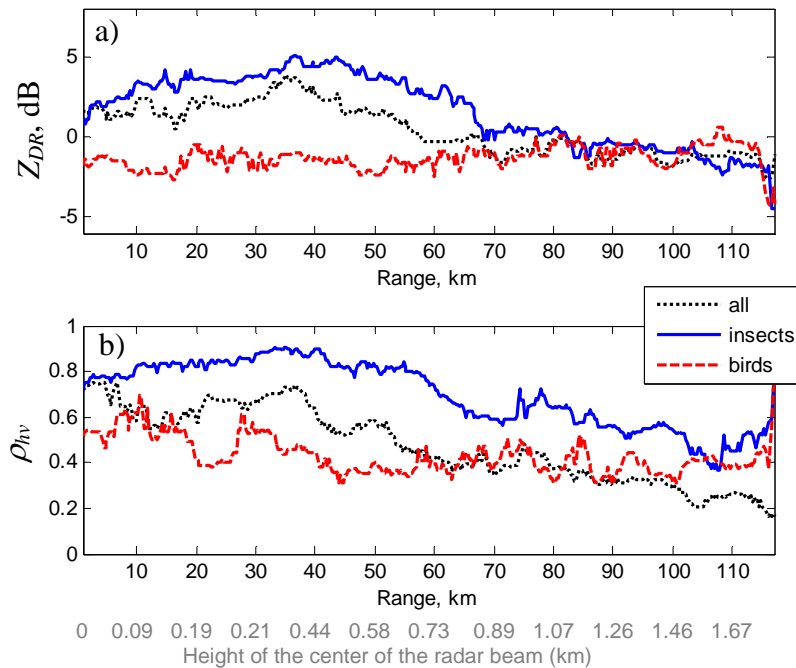


Figure 5.10. Range dependence of polarimetric values computed for chosen portions of spectral coefficients displayed in Figure 5.9: a) differential reflectivity and b) copolar correlation coefficient. The dotted curve corresponds to the mean parameter computed from all spectral coefficients. The solid and dashed lines correspond to the parameter computed with the window retaining the signal power of presumed insects and birds, respectively.

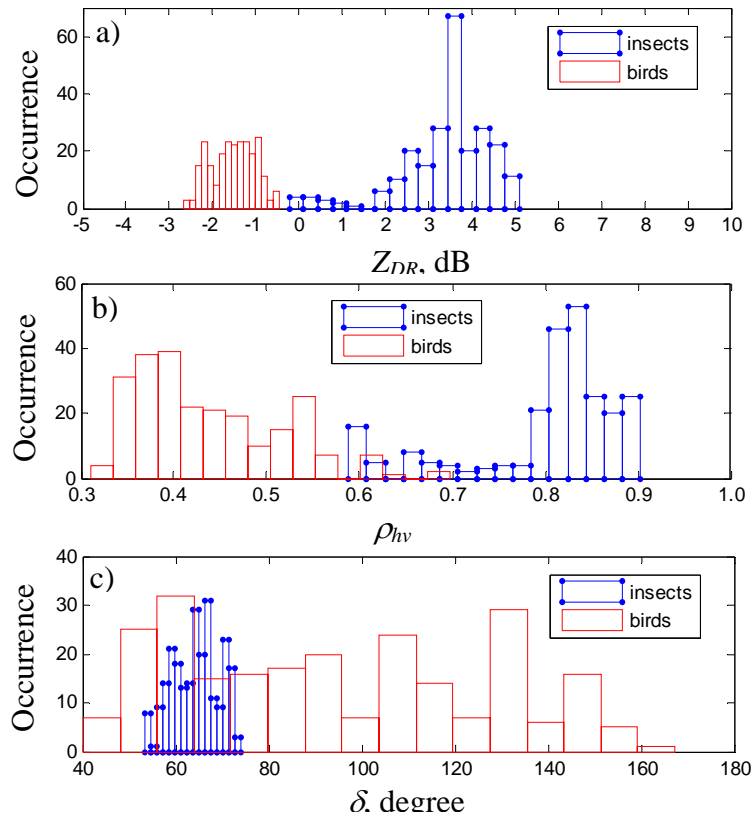


Figure 5.11. Histogram of a) differential reflectivity, b) copolar correlation coefficient and c) differential phase computed from spectral segments designated as insects and bird for the radial at azimuth  $180^\circ$ , elevation  $0.5^\circ$ , and ranges from 10 km to 70 km.

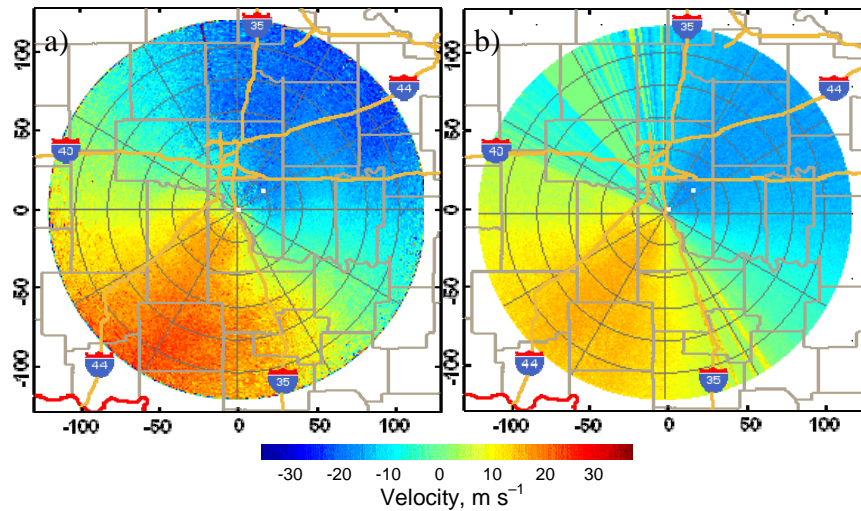


Figure 5.12: The PPI of Doppler velocity (11 pm, H channel, elevation  $0.5^\circ$ ): a) original and b) corrected.

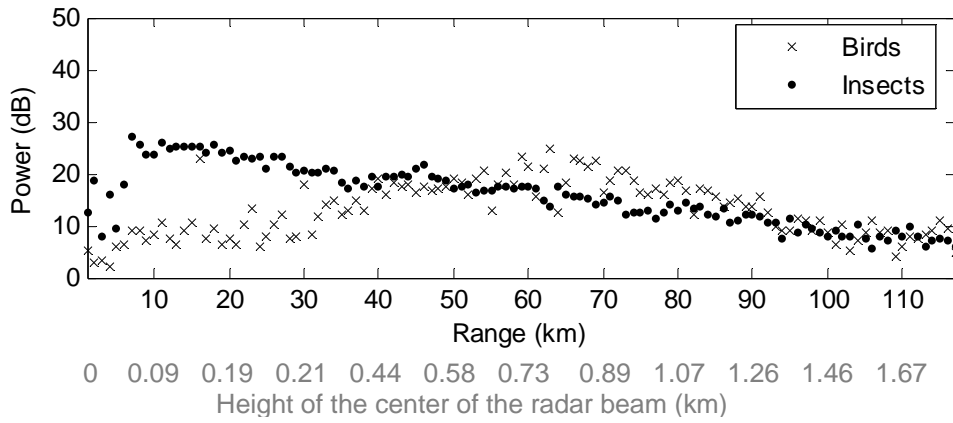


Figure 5.13. Power in spectral coefficients of the bird and insect bands. The power is averaged for azimuths from  $178^\circ$  to  $182^\circ$  and 4 resolution volumes in range. (11 pm H channel, elevation  $0.5^\circ$ )

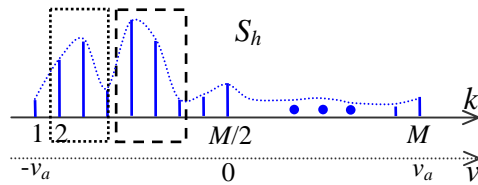


Figure 6.1. Two windows positioned on spectral coefficients of a bimodal spectrum. Each window contains spectral coefficient with significant returns concentrated at a particular velocity. The horizontal axis is labeled with the spectral coefficient number  $k$  and corresponding velocity  $v$ .

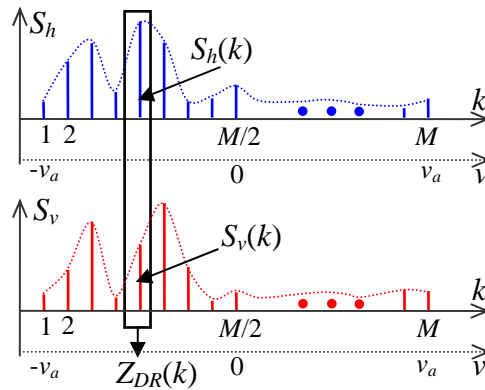


Figure 6.2. Spectra in H (top) and V (bottom) channel are used for the computations of polarimetric spectral densities.

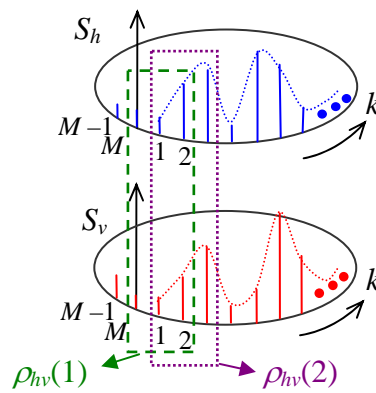


Figure 6.3. Illustration of the three point running averages on spectral coefficients of H and V channels used to compute  $\rho_{hv}$ . To compute  $\rho_{hv}(1)$  the  $M$ th, 1st, and 2nd coefficients enclosed in dashed rectangle are used.  $\rho_{hv}(2)$  is computed using 1st, 2nd, 3rd coefficients enclosed in dotted rectangle. In general,  $\rho_{hv}(k)$  is computed from  $(k-1)$ ,  $k$ , and  $(k+1)$ .

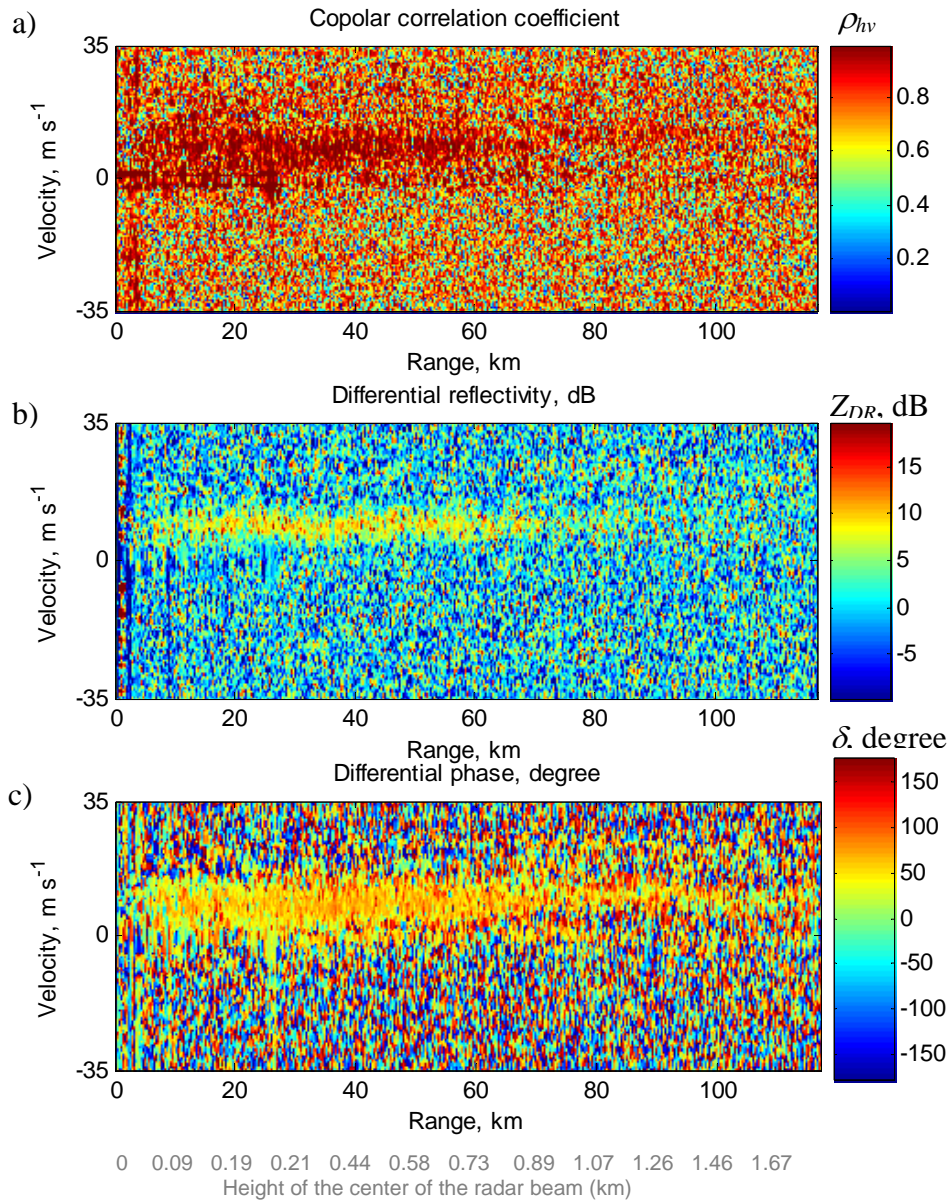


Figure 6.4. Spectral densities of polarimetric variables in a radial: a)  $\rho_{hv}SD$ , b)  $Z_{DR}SD$ , and c)  $\delta SD$ . Each spectral field shows a well defined band caused by the returns from insects. Streaks at ranges 0 to 10 km are due to the ground clutter returns (11 pm, elevation  $0.5^\circ$ , azimuth  $180^\circ$ )

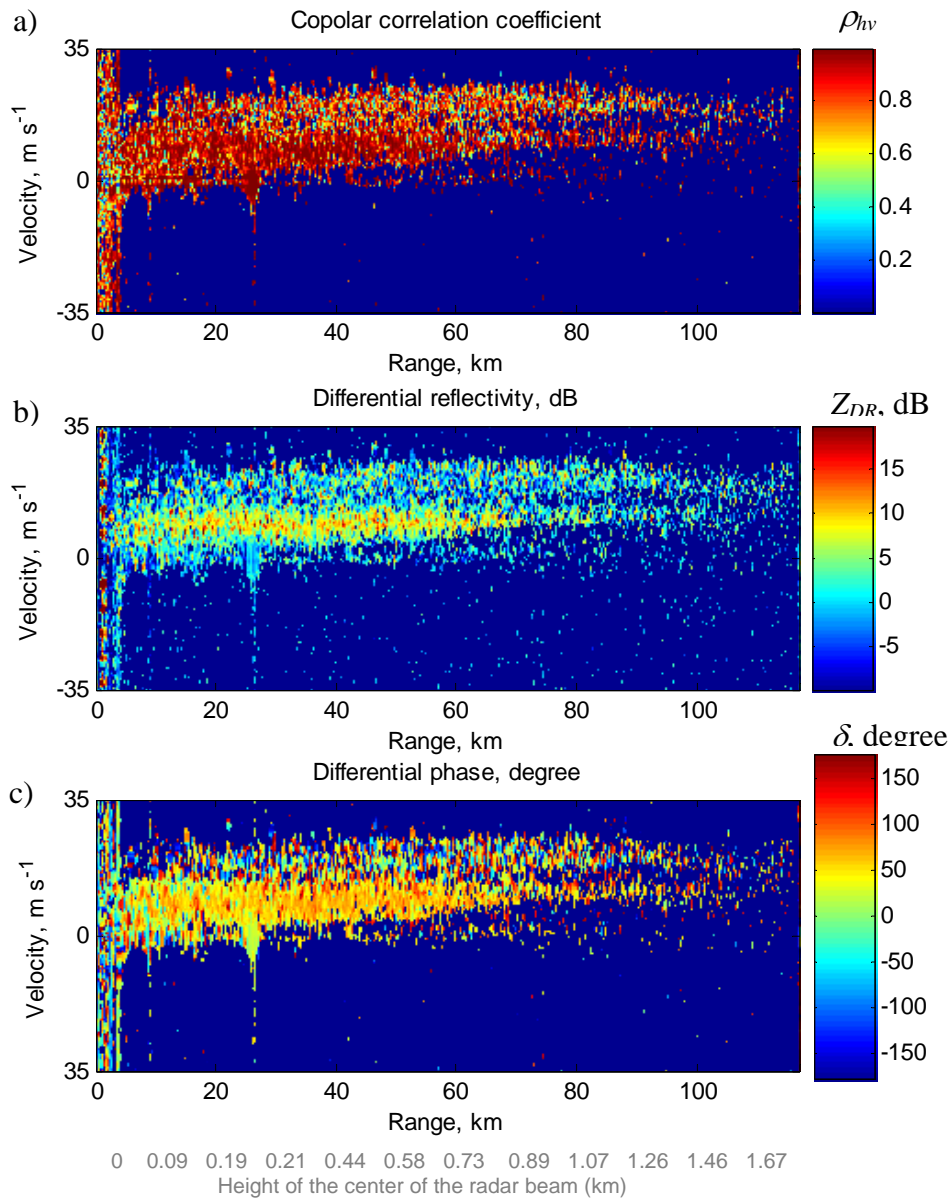


Figure 6.5. Spectral densities of polarimetric variables in a radial after a power threshold: a)  $\rho_{hv}SD$ , b)  $Z_{DR}SD$ , and c)  $\delta SD$ . Each spectral field shows two well defined bands caused by the returns from insects and birds. The radial points at  $180^\circ$ , the wind direction is about  $225^\circ$ .

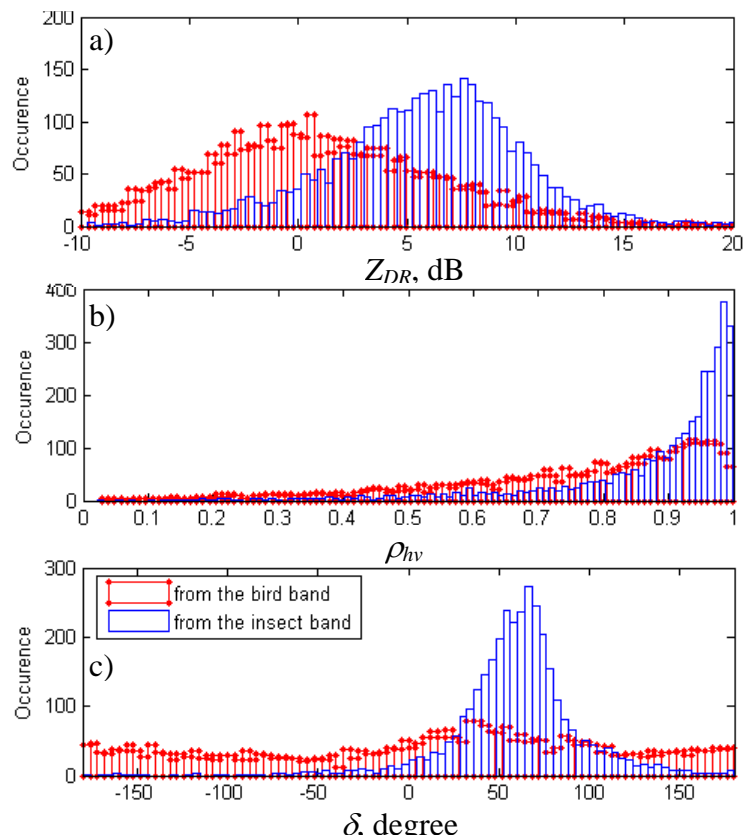


Figure 6.6. Histograms of the polarimetric variables from portions of the polarimetric spectral fields contained within selections distinguished as birds and insects in Figure 5.10. Solid lines with a dot marker indicate histograms of bird selection. Solid lines without marker are for the insect selection. The histograms are computed from polarimetric spectral values in the fields of the radial at azimuth  $180^\circ$ , elevation  $0.5^\circ$  at ranges 10 to 70 km.

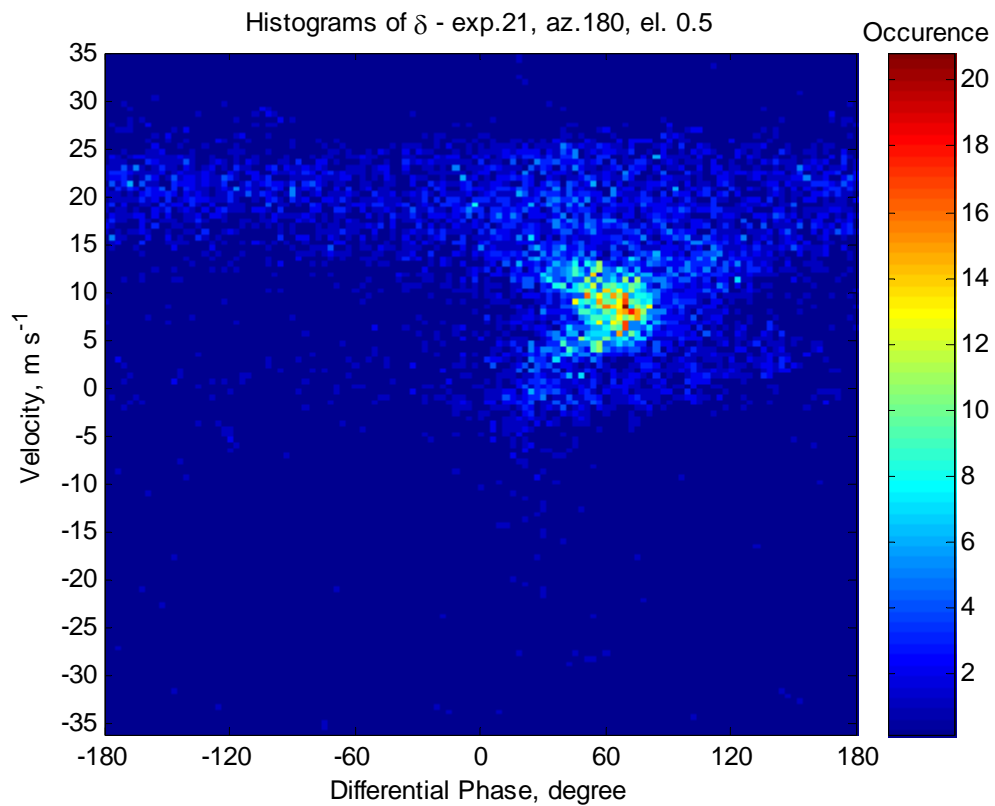


Figure 6.7. The 2D histogram of the  $\delta$ SD in a radial at 11 pm, elevation  $0.5^\circ$ , azimuth  $180^\circ$  and ranges between 10 km and 70 km. The histogram discloses a blob of scatterers with  $\delta$  of about  $70^\circ$  and velocity of about  $7 \text{ m s}^{-1}$ . A dim band with occurrences larger than background is at about  $21 \text{ m s}^{-1}$  and  $\delta$  in the whole interval from  $-180^\circ$  to  $180^\circ$ . There are also some scatterers with positive phases and velocity values close to zero. The intense blob is from the insects carried by the wind.

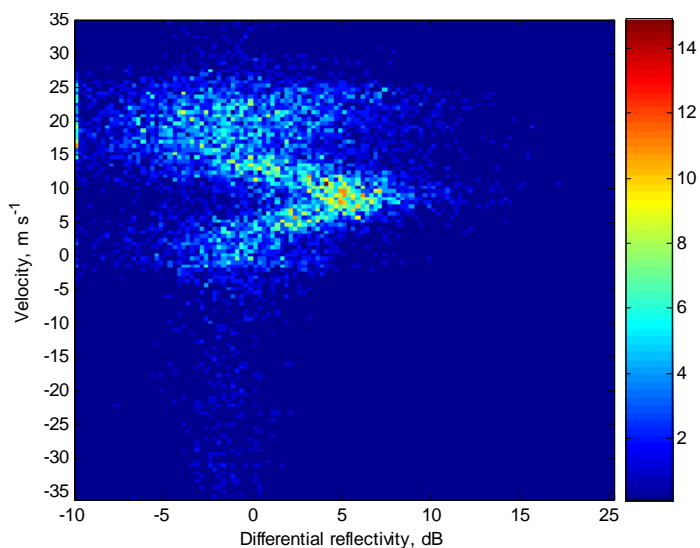


Figure 6.8. The 2D histogram of the  $Z_{DR}SD$  at 11 pm, elevation  $0.5^\circ$ , azimuth  $180^\circ$  and ranges between 10 km and 70 km. The brightest curve at  $7 \text{ m s}^{-1}$  with more than 5 dB  $Z_{dr}$  is from the insects carried by the wind.

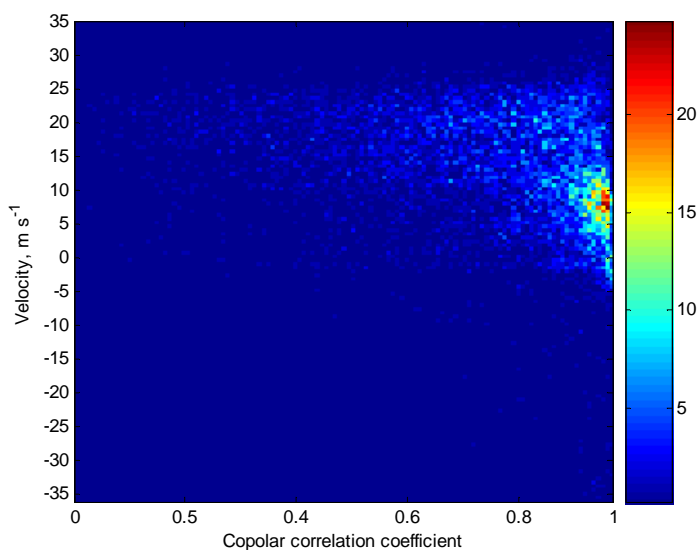


Figure 6.9. The 2D histogram of the  $\rho_{hv}SD$  at 11 pm, elevation  $0.5^\circ$ , azimuth  $180^\circ$  and ranges between 10 km and 70 km. A blob at  $7 \text{ m s}^{-1}$  with  $\rho_{hv}$  close to 1 is due to insects. The scatterers with smaller values of  $\rho_{hv}$  emerge at velocities between 10 and  $25 \text{ m s}^{-1}$ .

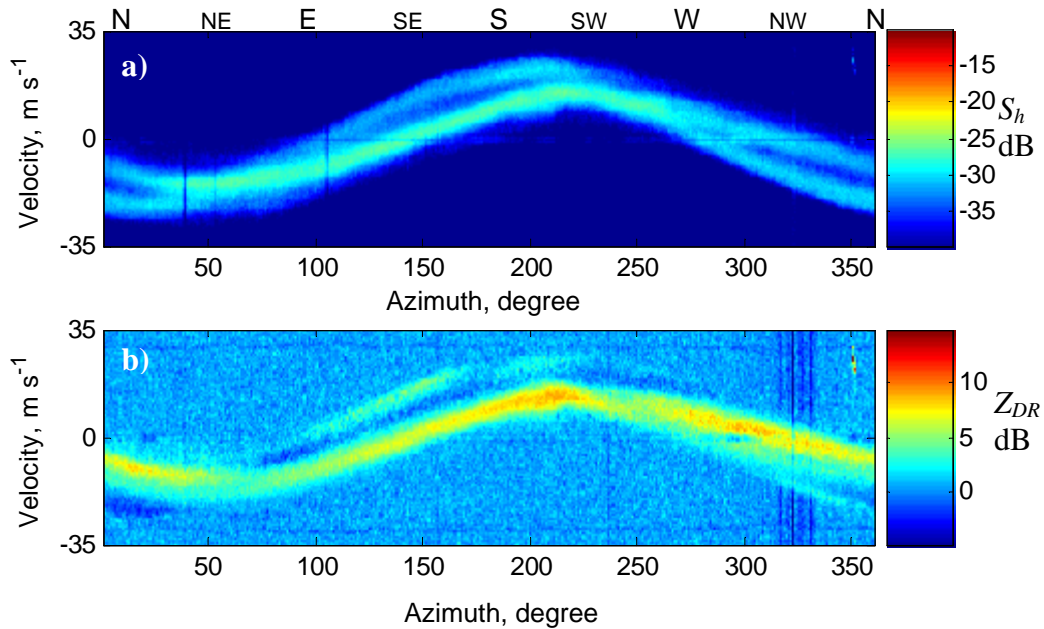


Figure 6.10. Spectral VADs of a)  $S_h$ , and b)  $Z_{DR}$ , disclose two sinusoids. The mean spectral densities are computed by averaging spectral densities from ranges between 30 km and 70 km (11 pm elevation  $0.5^\circ$ ).

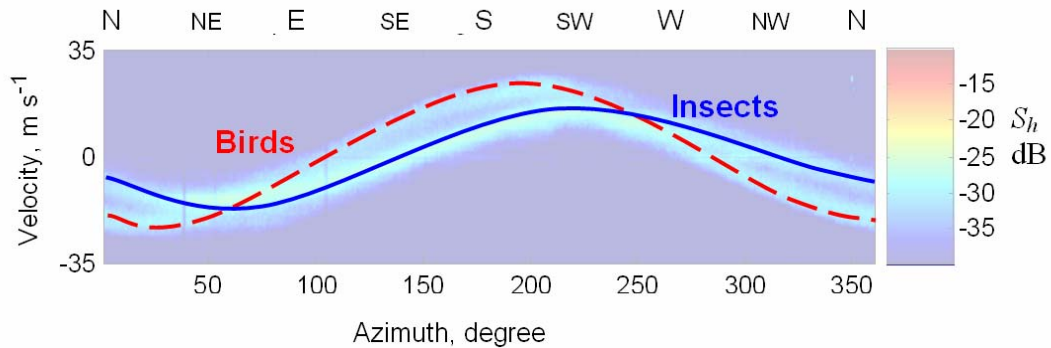


Figure 6.11. VAD visually deduced from the polarimetric densities superimposed on power in H channel shows two sinusoids. One sinusoid, indicated with a solid blue line, corresponds to the velocities of insects tracing the wind, the other (dashed red line) represents mean bird flow. The differential reflectivity alone was used in this case to determine the nature of the scatterers.

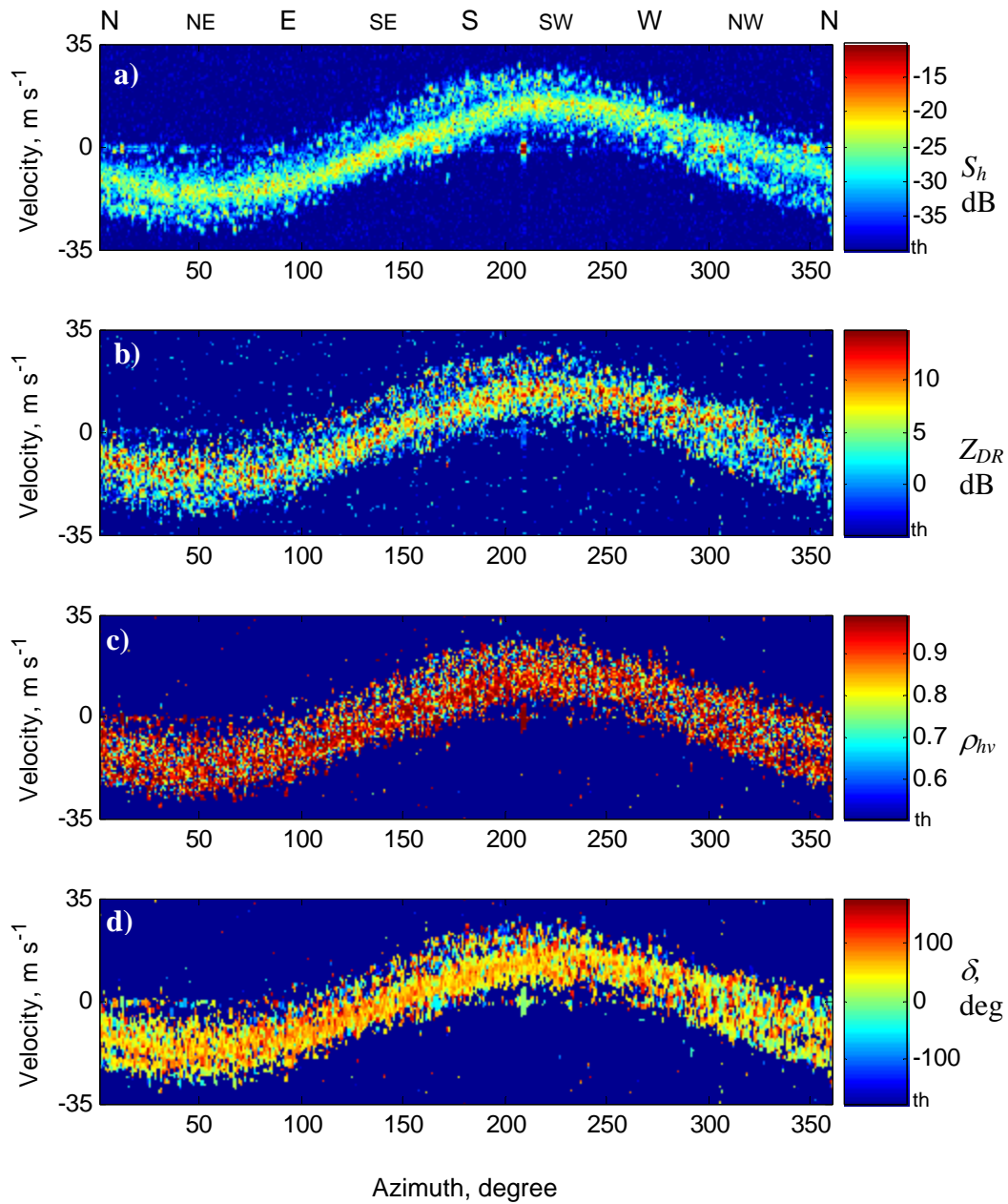


Figure 6.12. The SVADs computed from spectral densities of polarimetric variables at 30 km range. The SVAD of a) reflectivity in H channel, b) differential reflectivity, c) copolar correlation coefficient, and d) backscatter differential phase are each color coded according to the color-bar shown to the right. The power threshold is at the noise level -40 dB (see Figure 5.2).

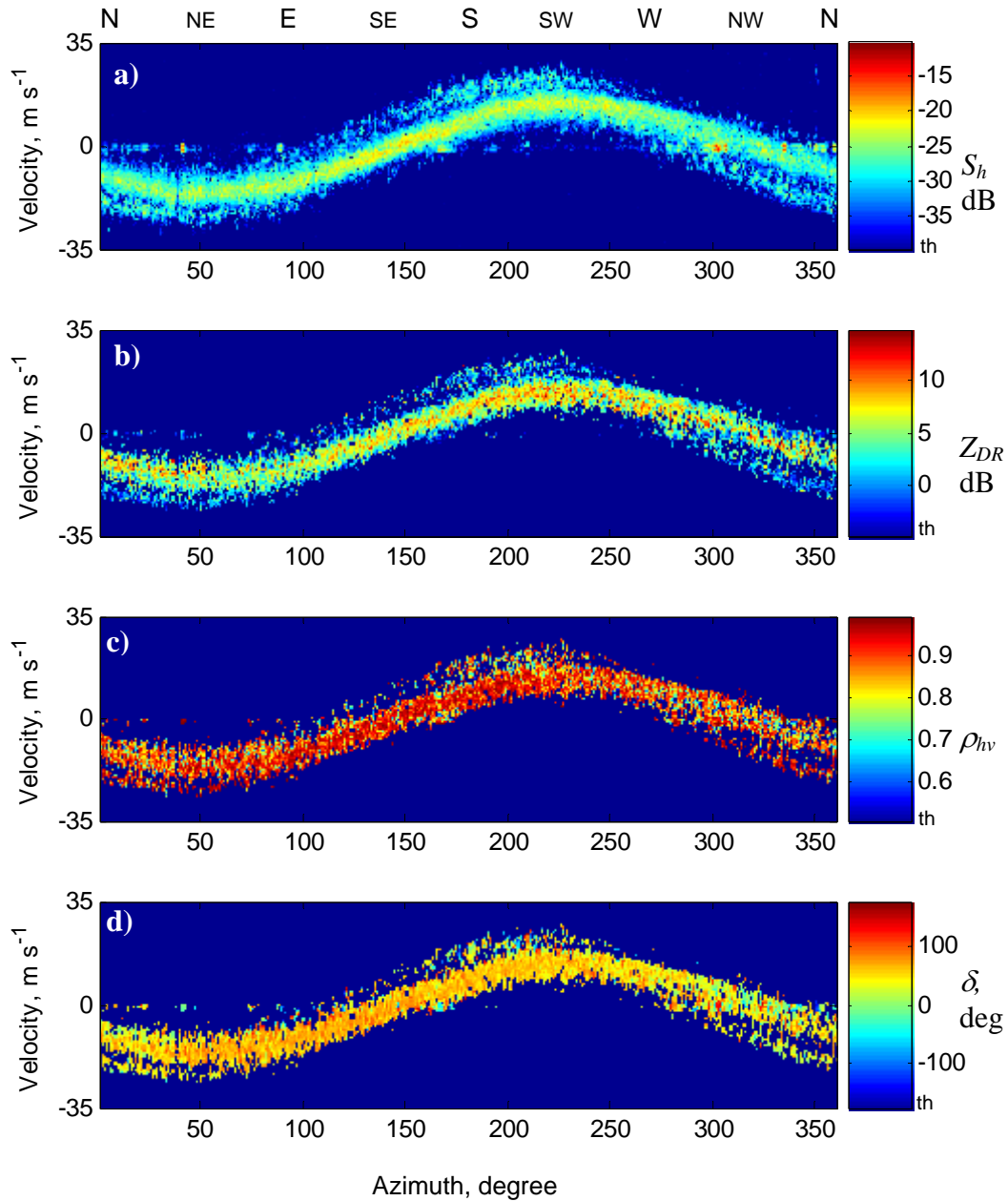


Figure 6.13. The SVADs computed from 4-range-averages of polarimetric spectral densities at ranges between 30 km and 31 km. The SVAD of a) reflectivity in the H channel, b) differential reflectivity, c) copolar correlation coefficient, and d) backscatter differential phase are each color coded according to the color-bar shown to the right. The power threshold is at noise level -40 dB (see Figure 5.2).

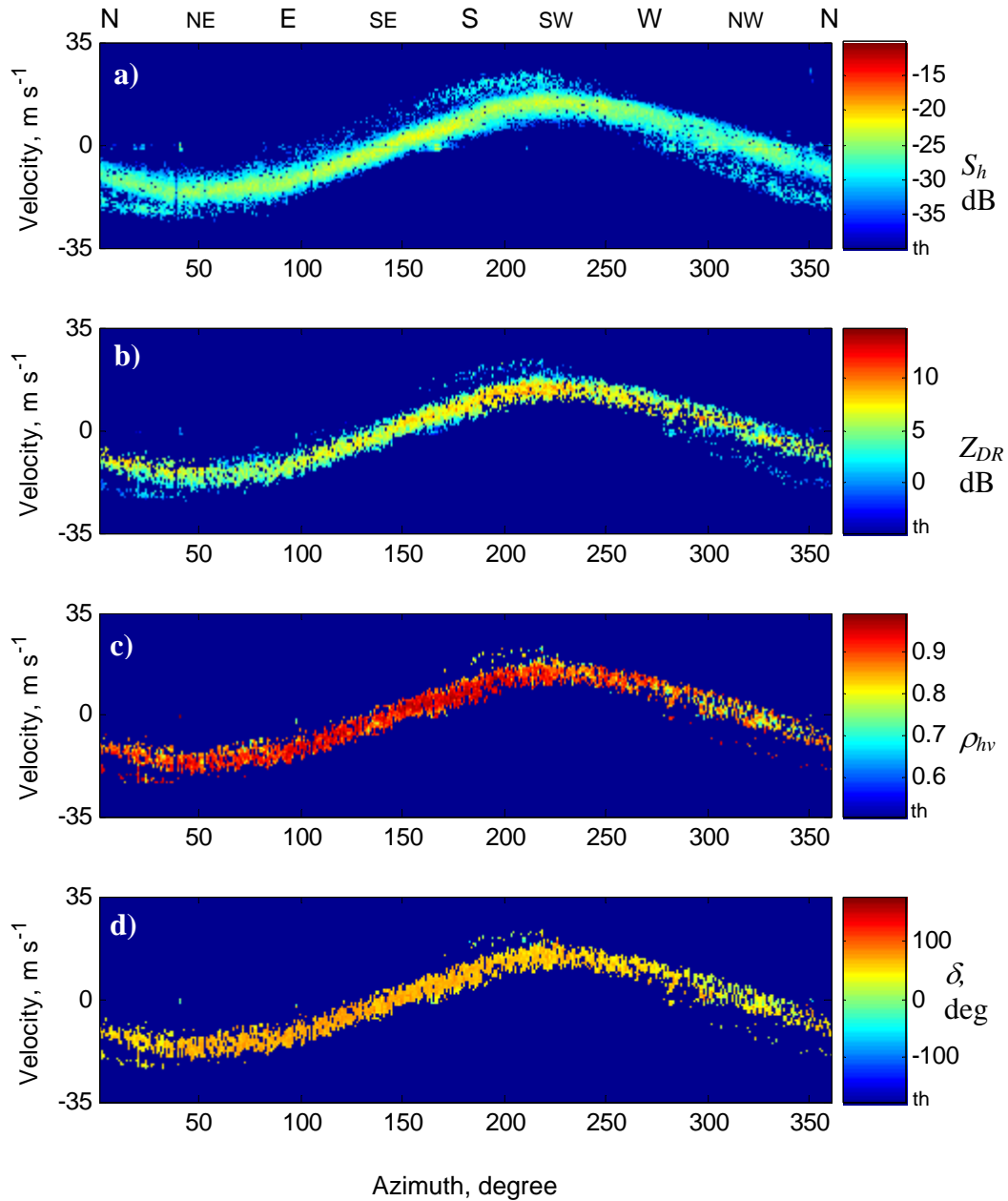


Figure 6.14. The SVADs computed from a 20-range-averages (5 km) of polarimetric spectral densities at ranges between 30 km and 35 km. The SVAD of a) reflectivity in the H channel, b) differential reflectivity, c) copolar correlation coefficient, and d) backscatter differential phase are each color coded with the color-bar shown to the right. The power threshold is at noise level -40 dB (see Figure 5.2).

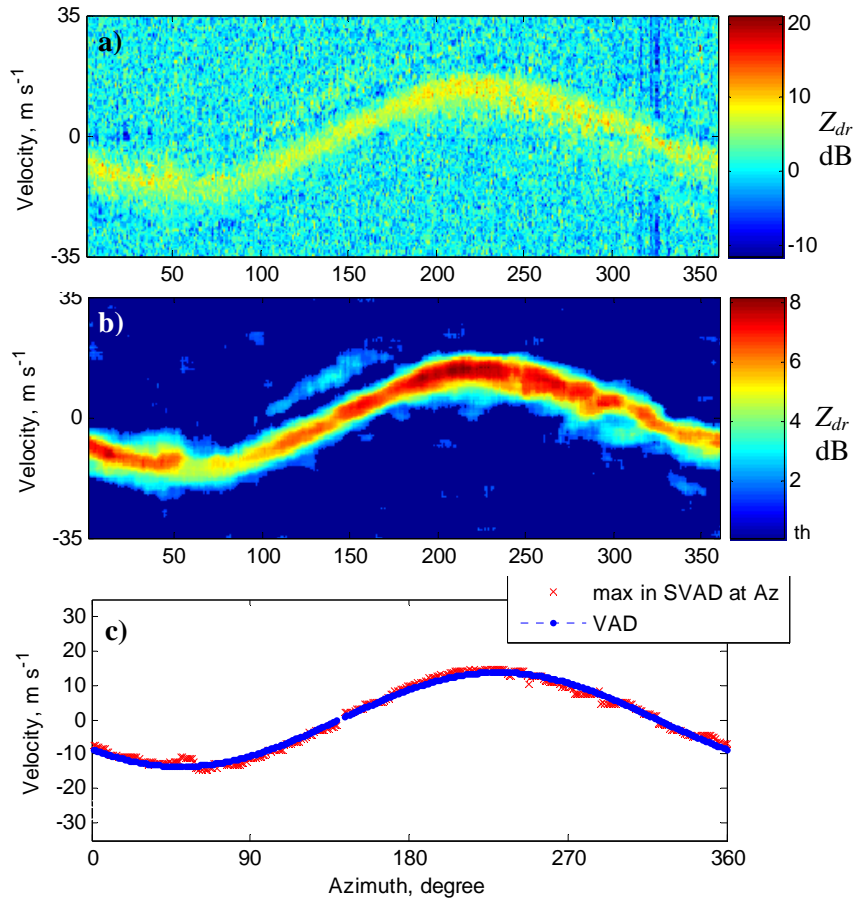


Figure 6.15. VAD estimated from the SVAD (11 pm, elevation 0.5°): a) SVAD of  $Z_{DR}$ ; b) SVAD of  $Z_{DR}$  after a combination of power(-40 dB) and  $\rho_{hv}$  (0.7) threshold; c) VAD.

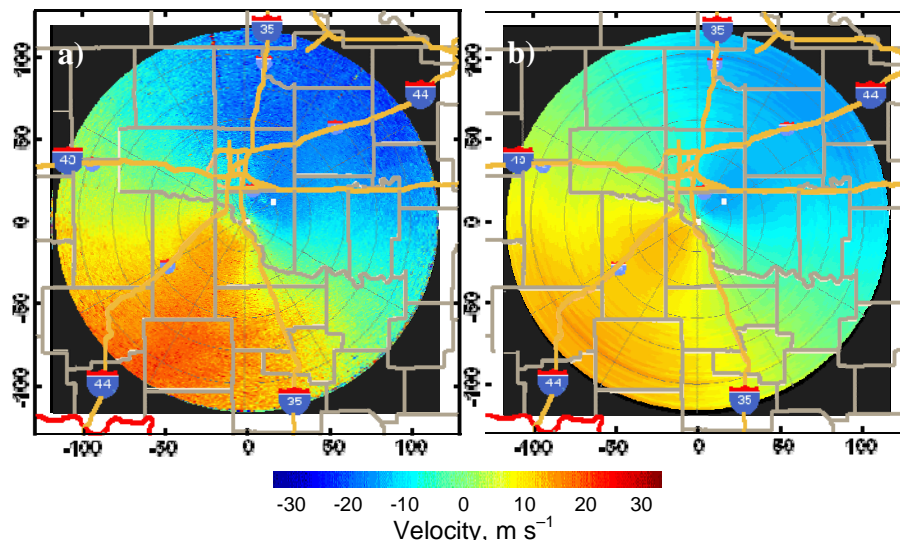


Figure 6.16. The PPI of Doppler velocity (11 pm, H channel, elevation 0.5°, azimuth 180°): a) original; b) corrected by the means of SVAD.

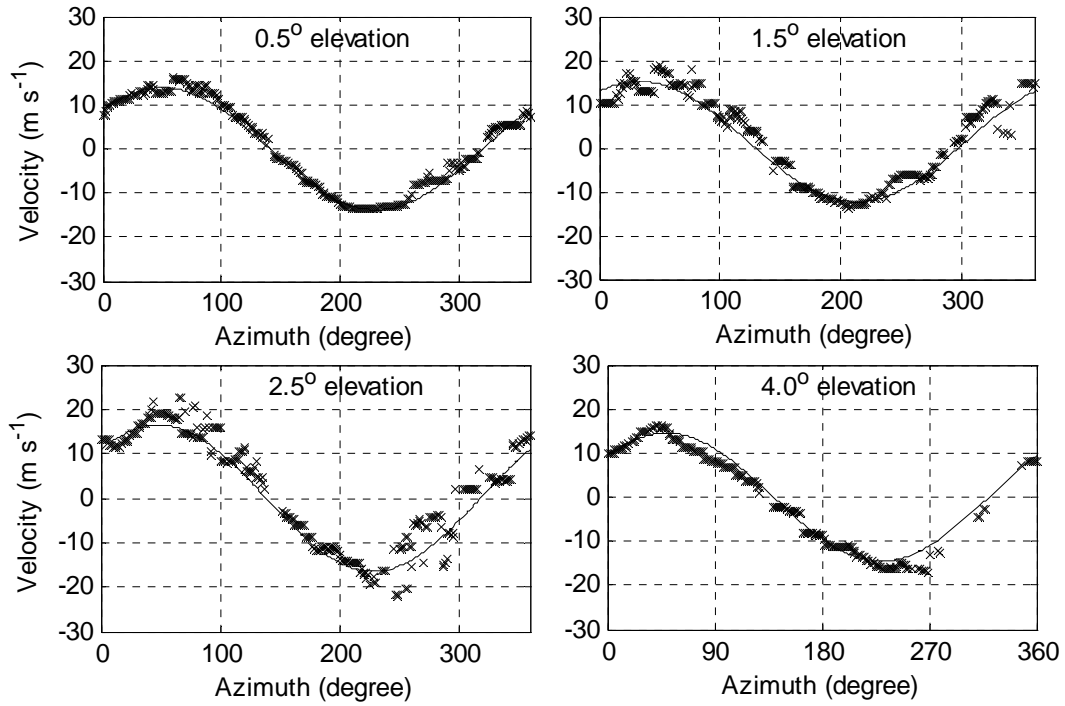


Figure 6.17. The VADs obtained from the spectral densities of differential reflectivity. Median values of the spectra of  $Z_{DR}$  over 1 km range interval are used at elevations of  $0.5^\circ$ ,  $1.5^\circ$ ,  $2.5^\circ$ , and  $4^\circ$  as indicated (11 pm).

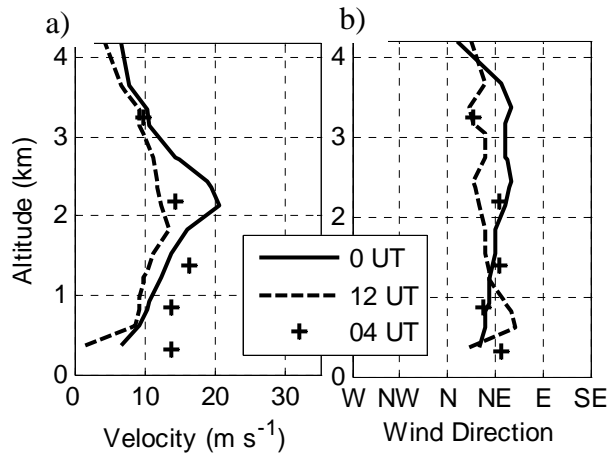


Figure 6.18. Vertical sounding of wind from the sounding on September 8, 2004 at 00 UT and 12 UT. (a) Wind speed, (b) wind direction.

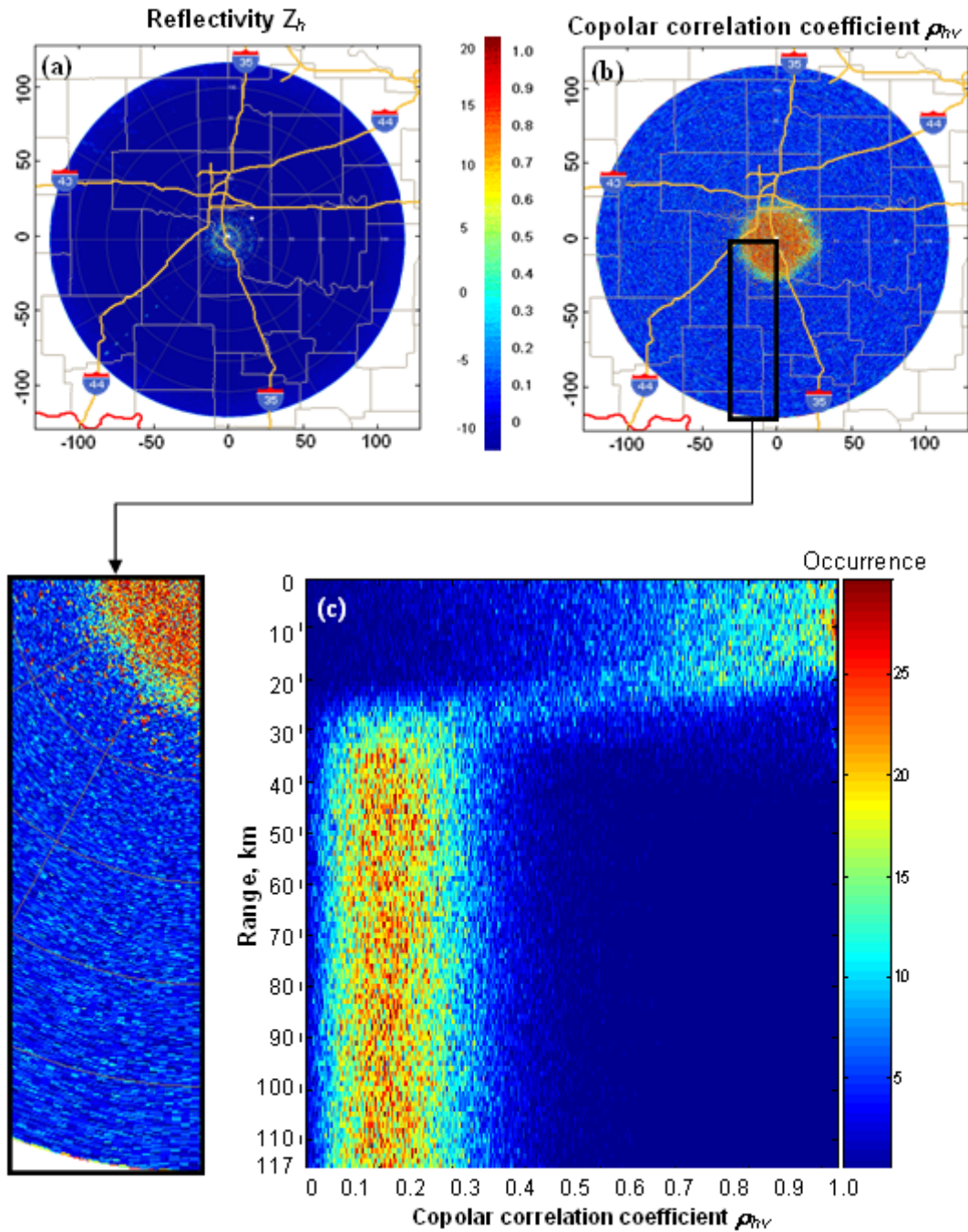


Figure 6.19. Comparing power and copolar correlation coefficient for alternative censoring: (a) PPI of reflectivity (11 pm, elevation  $6^\circ$ ), (b) PPI of copolar correlation coefficient, (c) histograms of  $\rho_{hv}$  computed for every range ring of the PPI shown in (b). Returns beyond 30 km in range are noise.

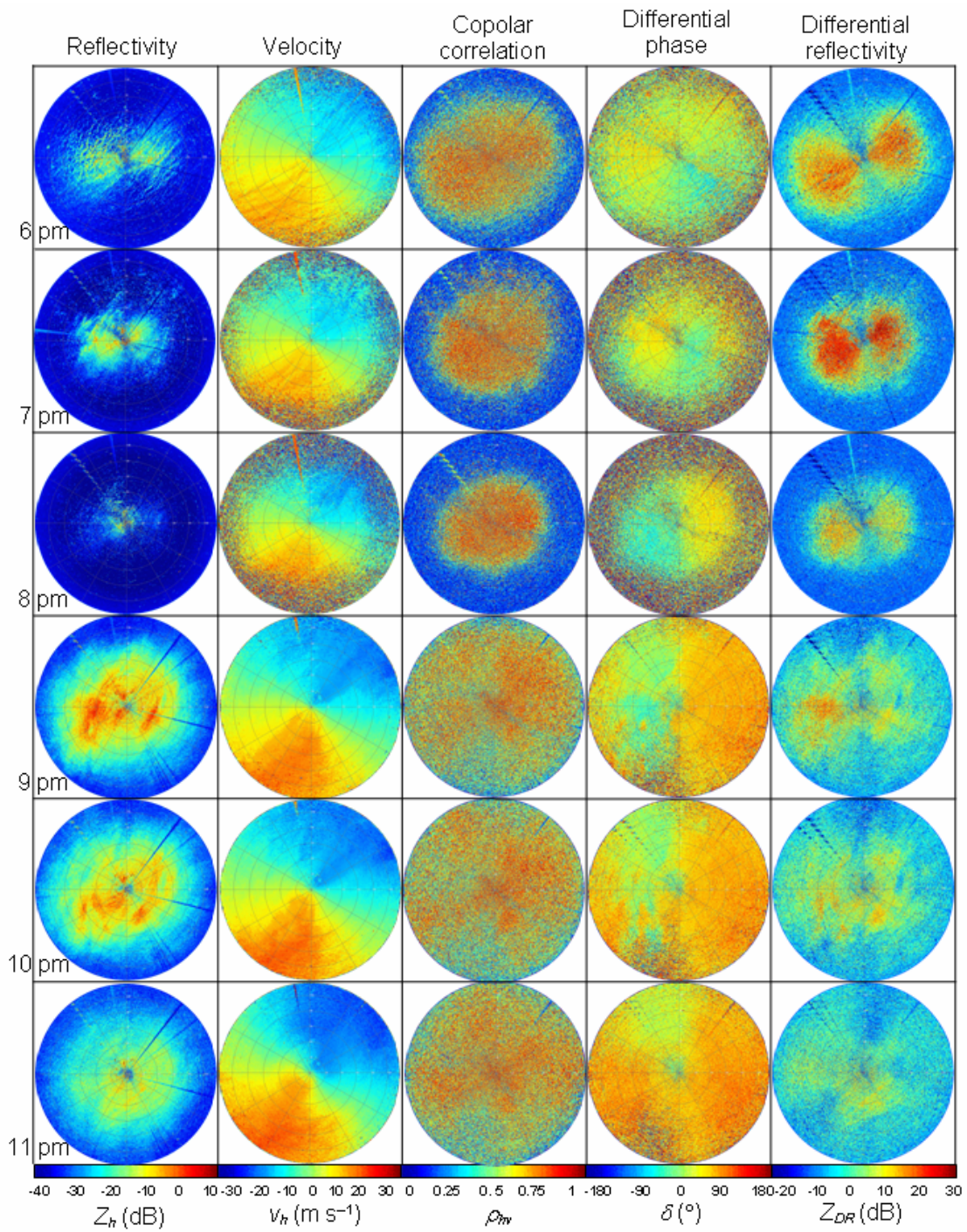


Fig 7.1. Polarimetric PPIs at elevation  $0.5^\circ$  and indicated (to the left) time instances. Maximum range is 117 km.

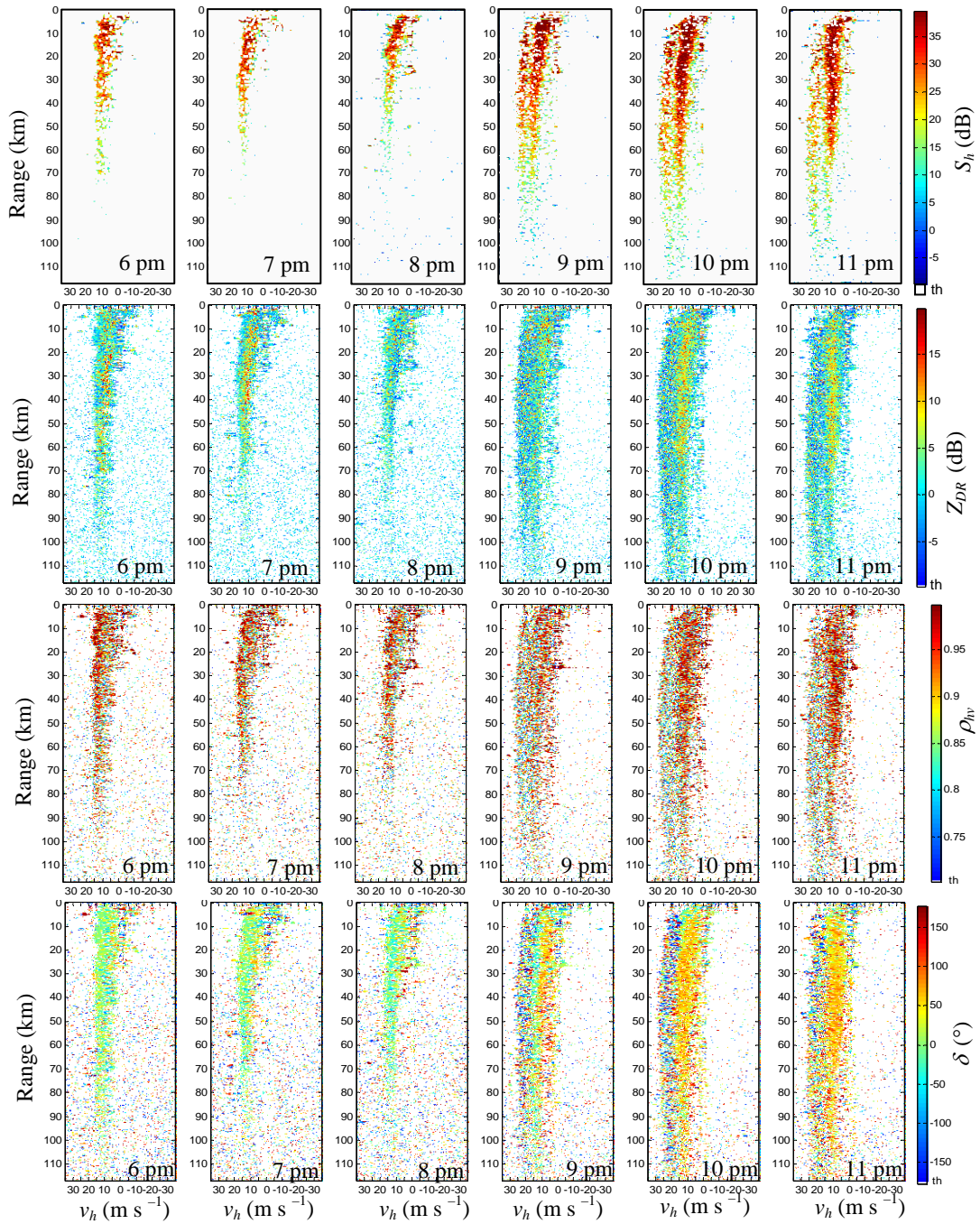


Figure 7.2. Polarimetric spectral densities in one radial (azimuth  $180^\circ$ , elevation  $0.5^\circ$ ) at the top of each hour from 6 pm until 11 pm as indicated.

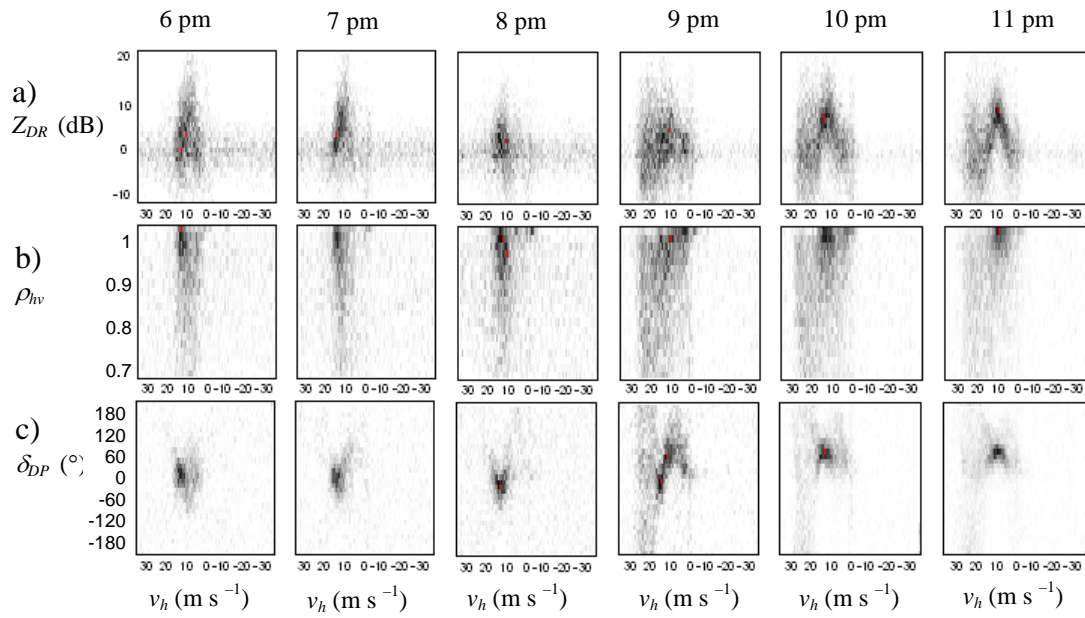


Figure 7.3. 2D histograms of spectral fields in Figure 7.2 for ranges from 30 km to 70 km and radial at 180° azimuth, 0.5° elevation. Darker color indicates larger occurrences; red dot indicates maximum occurrence.

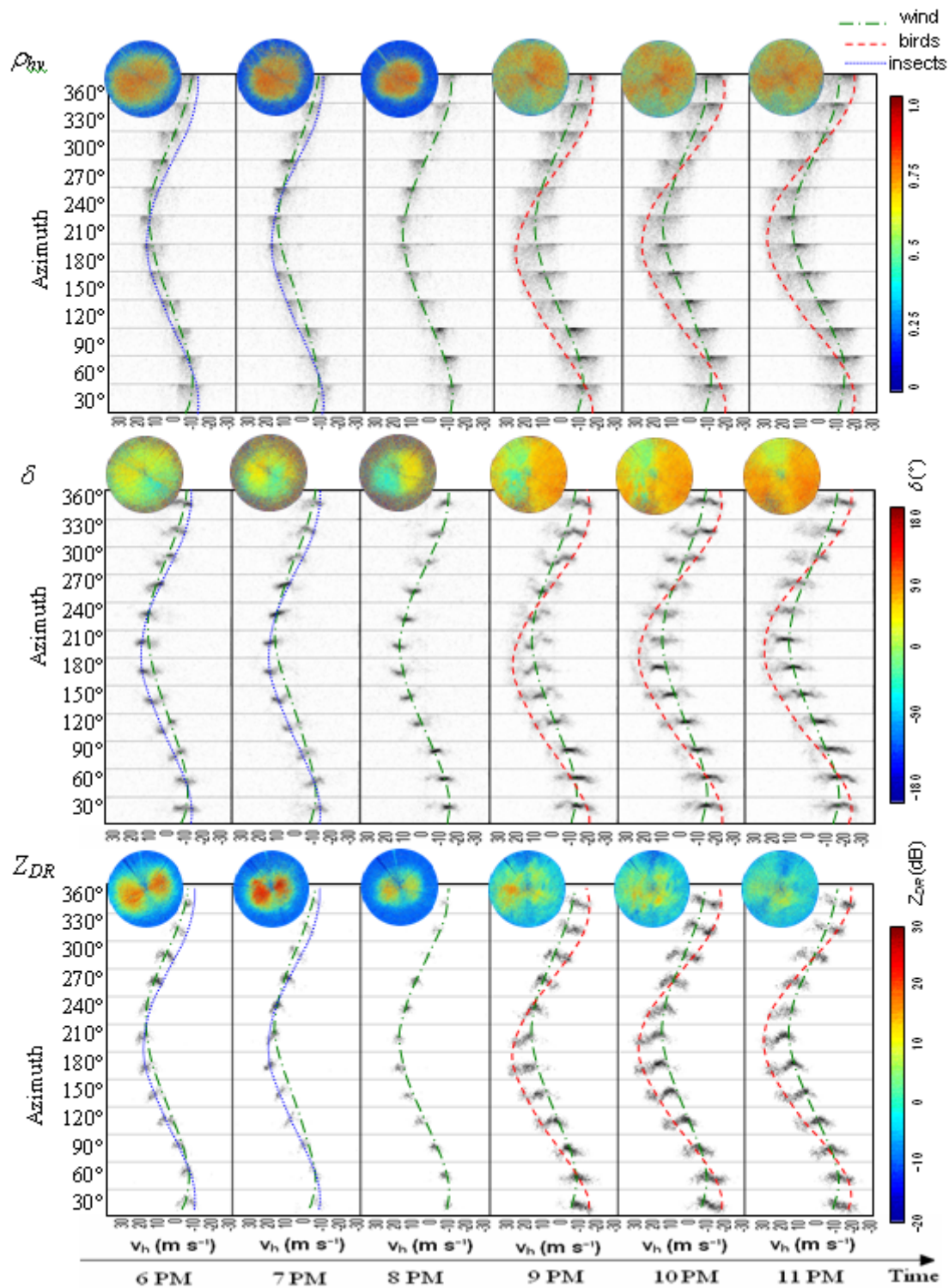


Figure 7.4. The ensemble of histograms ( $\rho_{hv}$ ,  $\delta$ ,  $Z_{DR}$ ) and possible VADs of contributing scatterers. The corresponding PPIs are shown for reference. Elevation  $0.5^\circ$ ,  $\rho_{hv} > 0.7$ .

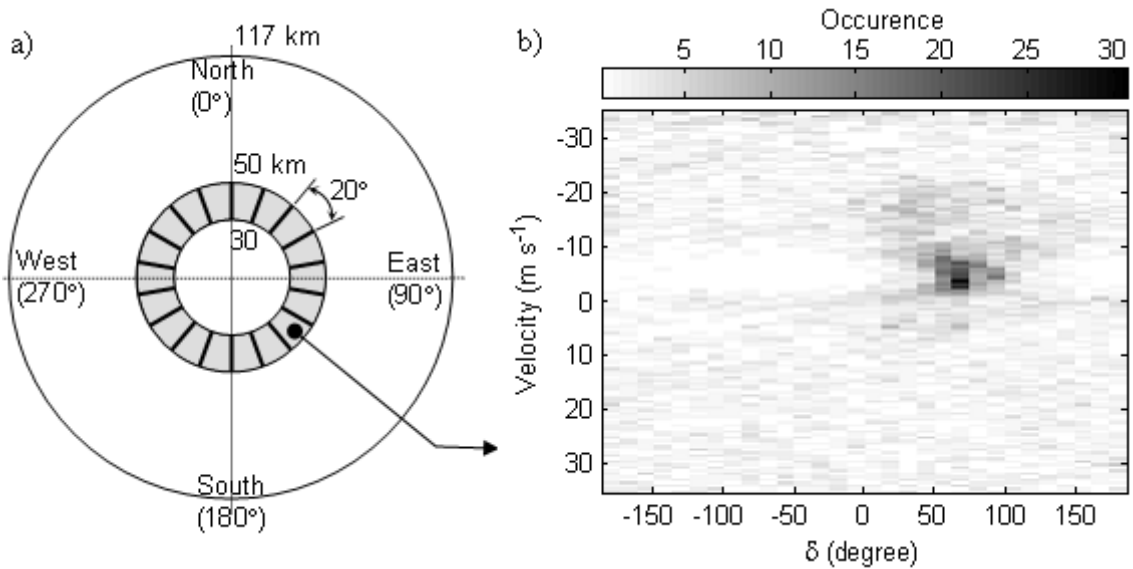


Figure 7.5. 2D histogram: (a) partitioning scanned area on portions, (b) 2D histograms of  $\delta SD$  for the indicated portion (centered at azimuth  $150^\circ$ , 11 pm, elevation  $0.5^\circ$ ). The spectral coefficients with  $\rho_{hv} < 0.7$  and insignificant power ( $S < 5\text{dB}$  above noise) are censored.

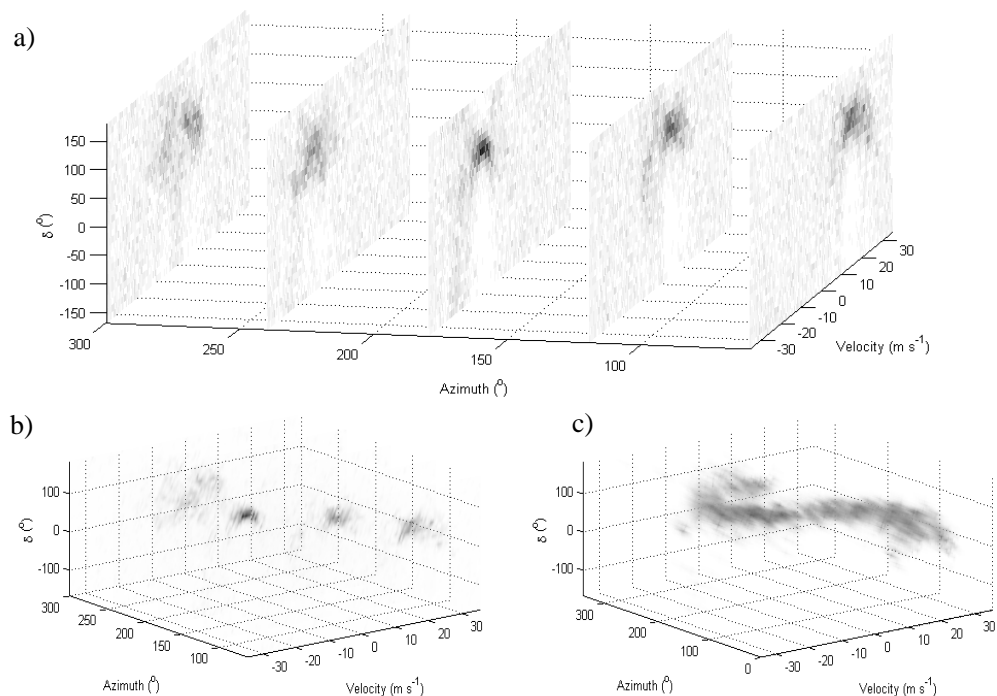


Figure 7.6. 3DASH formation from 2D histograms: (a) five slices with 2D-histograms of  $\delta SD$ , (b) the same five slices with transparency for small occurrences, and (c) all histograms together. The spectral coefficients with  $\rho_{hv} < 0.7$  and insignificant power ( $S < N + 5\text{dB}$ ) are censored.

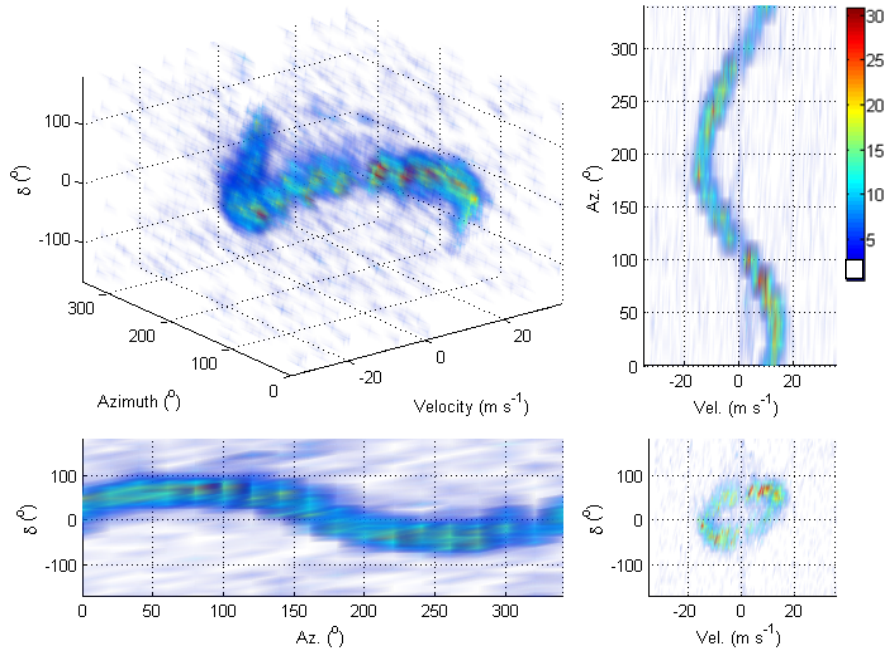


Figure 7.7. 3DASH of  $\delta SD$  at 8 pm displayed with 10 % transparency and its projections. Number of occurrences is indicated with the color bar.

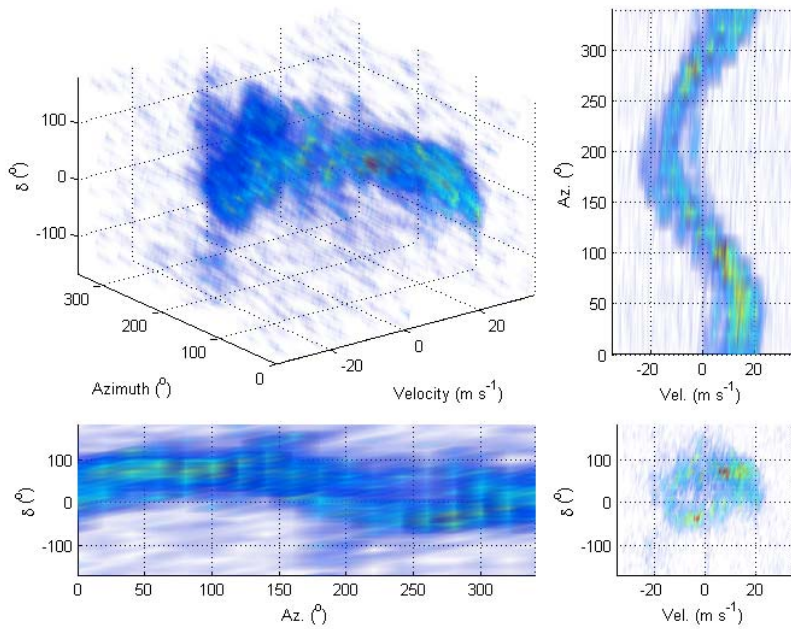


Figure 7.8. 3DASH of  $\delta SD$  at 9 pm displayed with 10 % transparency and its projections. Number of occurrences is according to the color bar in Figure 7.7.

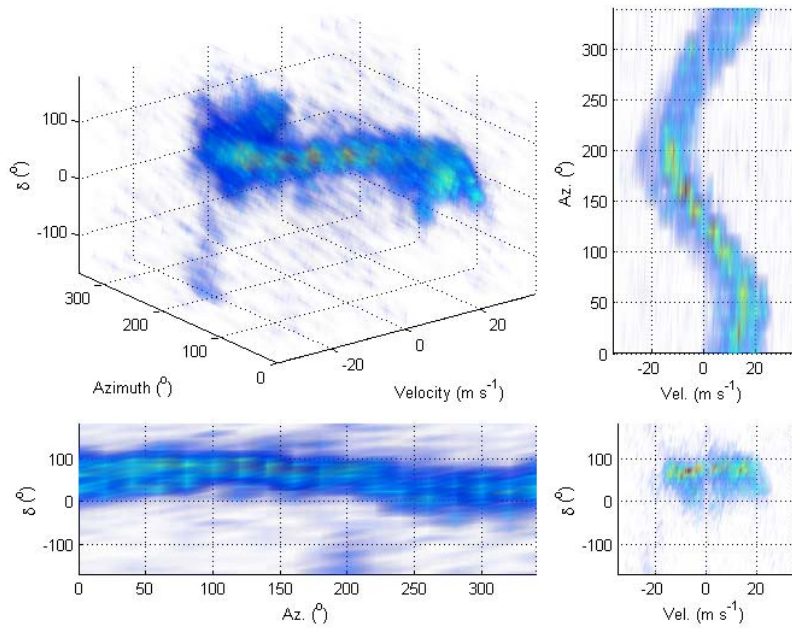


Figure 7.9. 3DASH of  $\delta SD$  at 10 pm displayed with 10 % transparency and its projections. Number of occurrences is according to the color bar in Figure 7.7

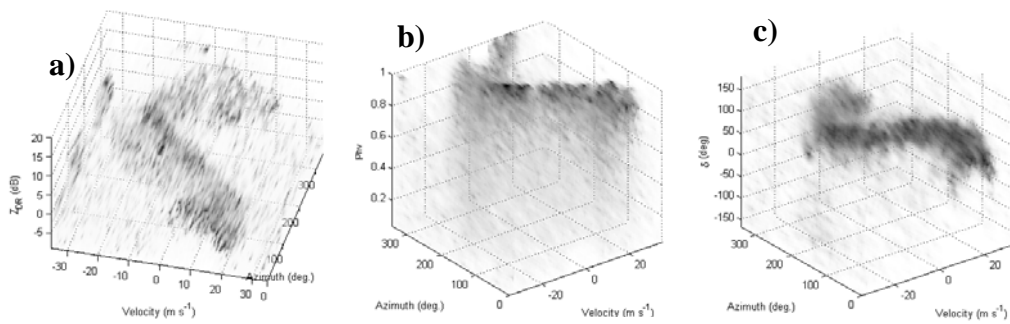


Figure 7.10. Polarimetric 3DASH examples: a)  $Z_{DR}$  3DASH, b)  $\rho_{hv}$  3DASH, and c)  $\delta$  3DASH.

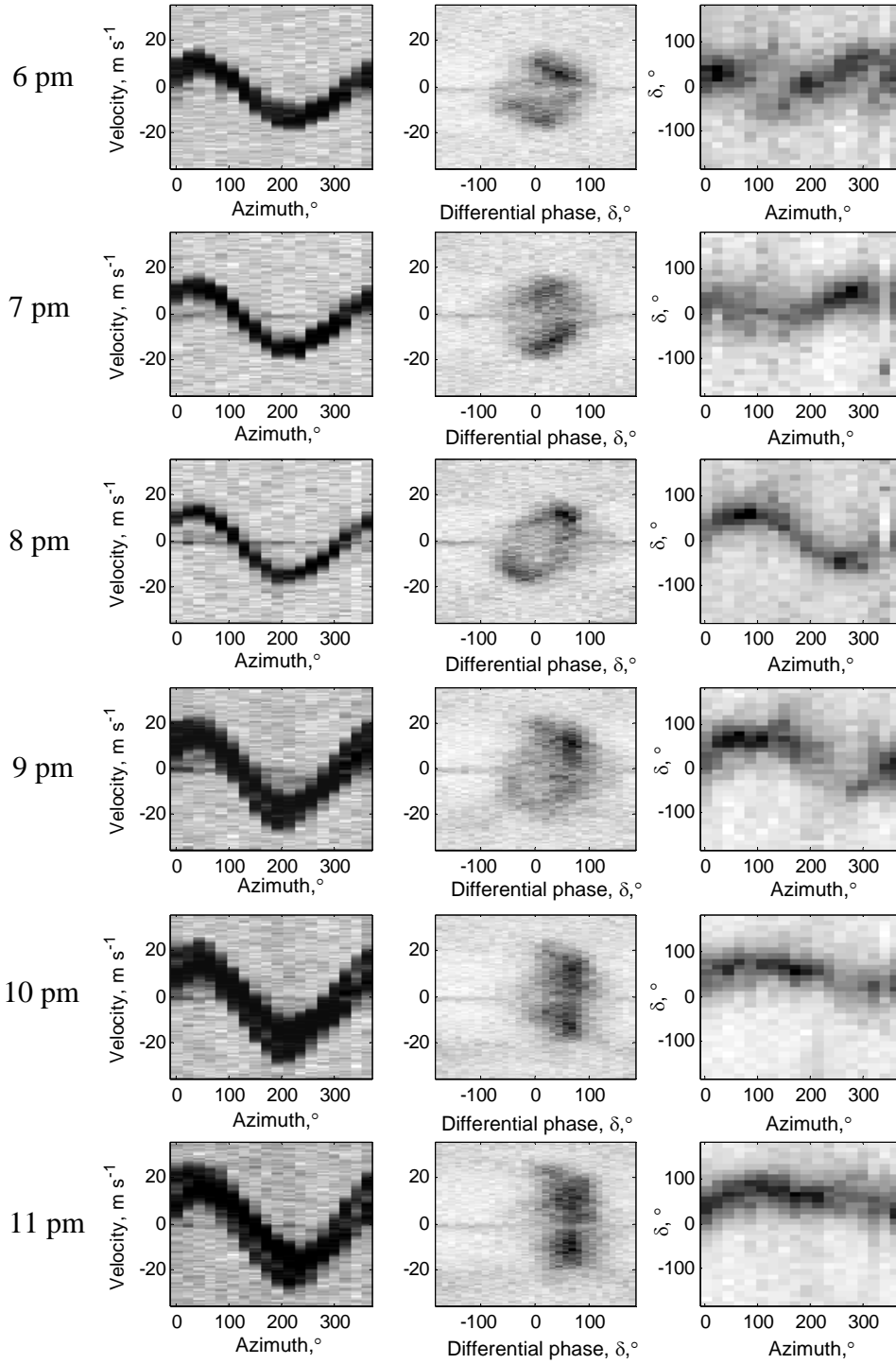


Figure 7.11. The 3DASH of  $\delta$  summed up to expose: left) velocity-azimuth histogram, middle) velocity- $\delta$  histogram, and right)  $\delta$ -azimuth histogram.

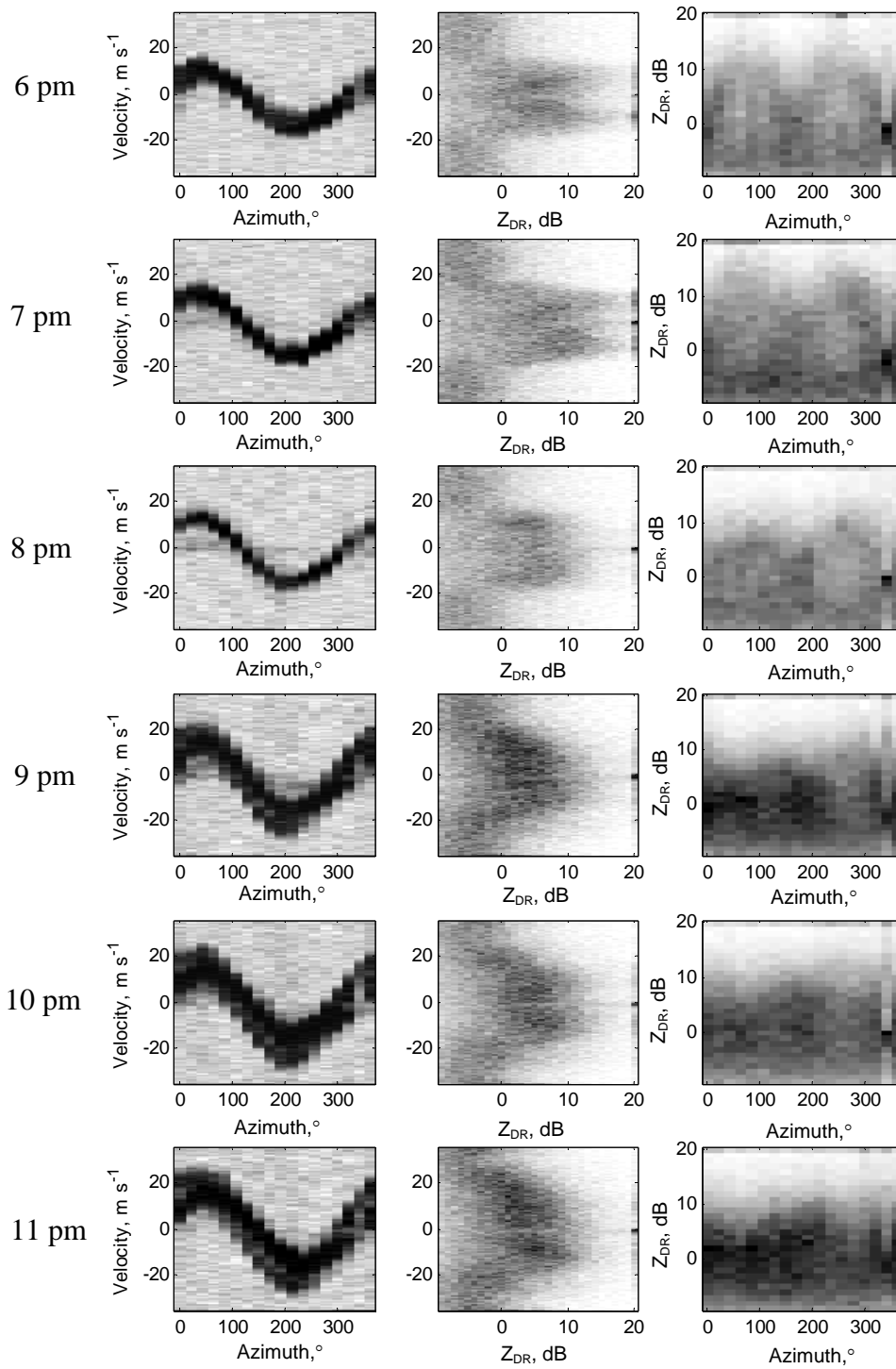


Figure 7.12. The 3DASH of  $Z_{DR}$  summed up to expose: left) velocity-azimuth histogram, middle) velocity- $Z_{DR}$  histogram, and right)  $Z_{DR}$ -azimuth histogram.

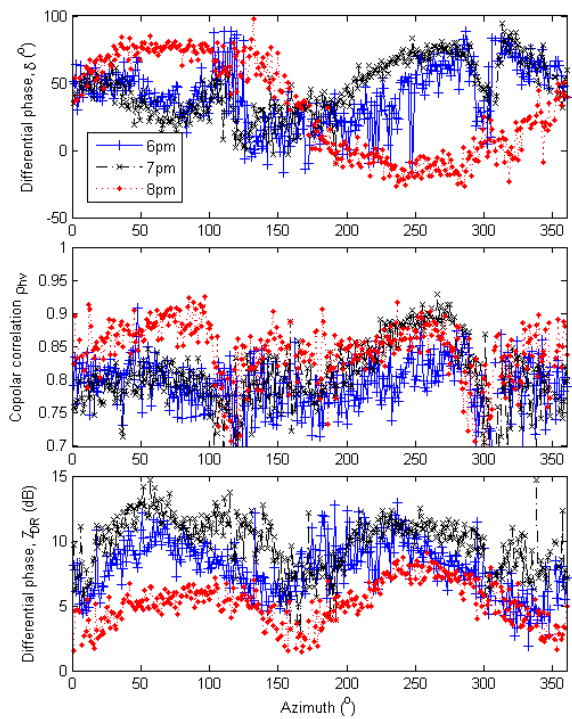


Figure 7.13. Azimuthal dependence of the insects' intrinsic polarimetric variables. Range is between 30 and 35 km. The values are computed for an adaptive window of spectral coefficients at times 6 pm, 7 pm and 8 pm as indicated in the legend.

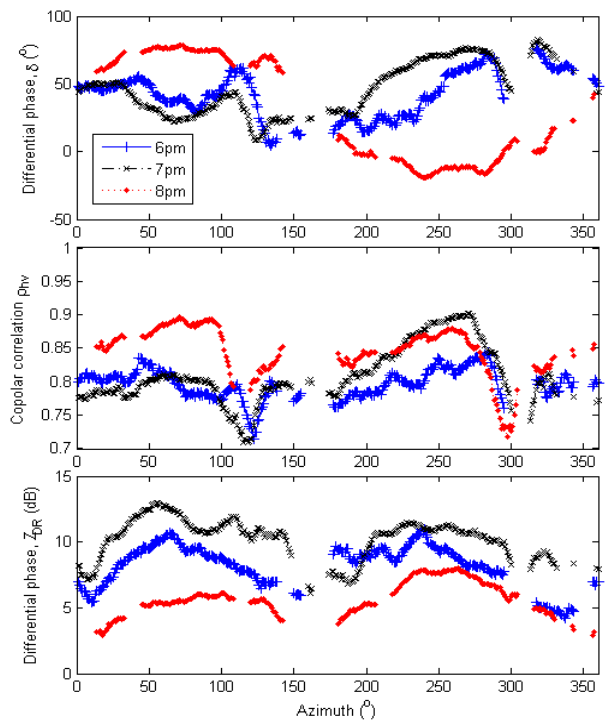


Figure 7.14. Azimuthal dependence of the insects' intrinsic polarimetric variables smoothed with a 9 point median filter. Range is between 30 and 35 km. The values are computed for an adaptive window of spectral coefficients.

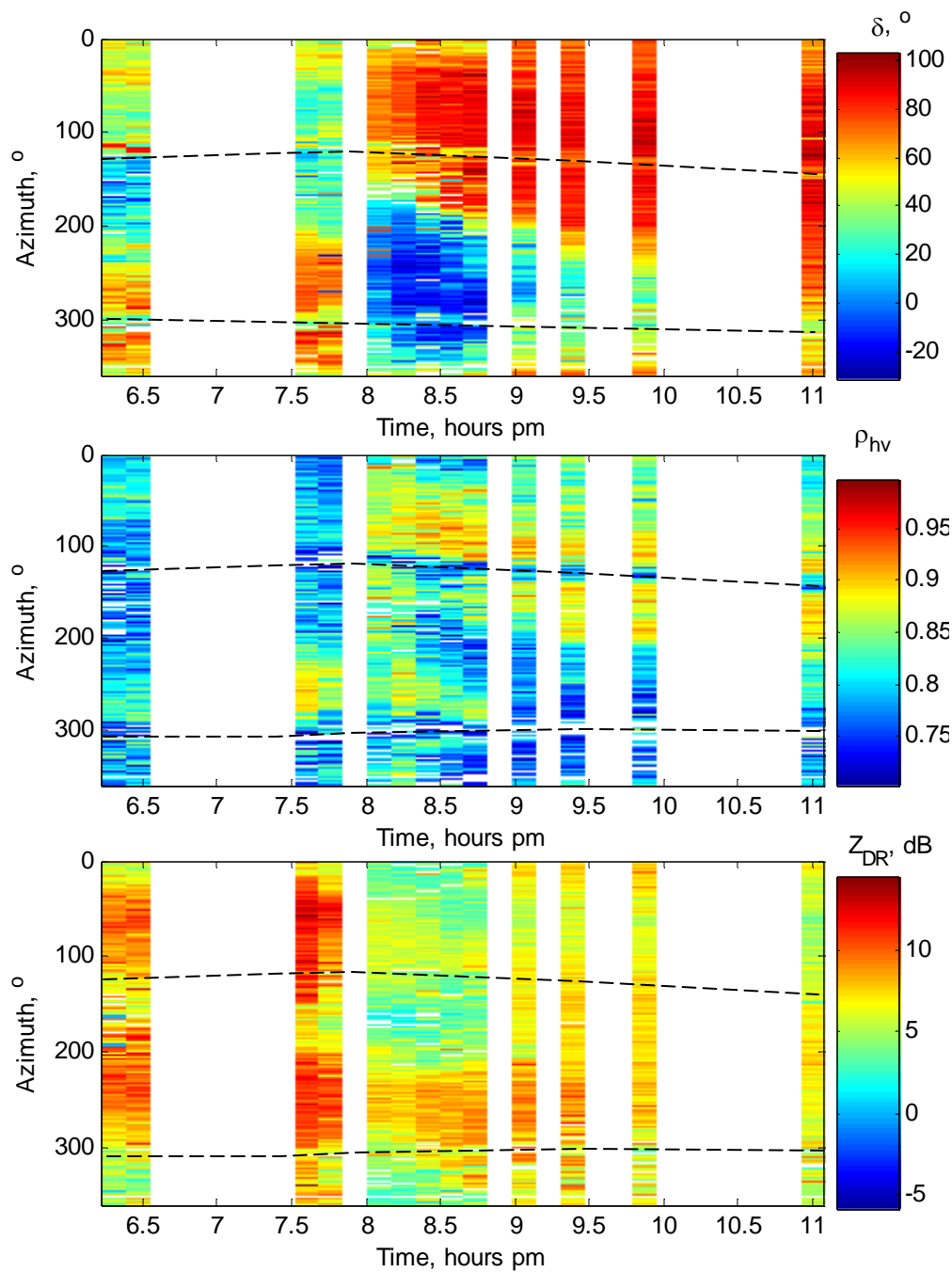


Figure 7.15. Azimuthal and time dependence of the insects' intrinsic polarimetric variables computed for an adaptive window of spectral coefficients. Range is between 30 and 35 km. Empty columns correspond to the gaps in data collection. Two paths (at about 120° and 300° in azimuth) correspond to zero radial velocity of wind and are indicated with a dashed line.

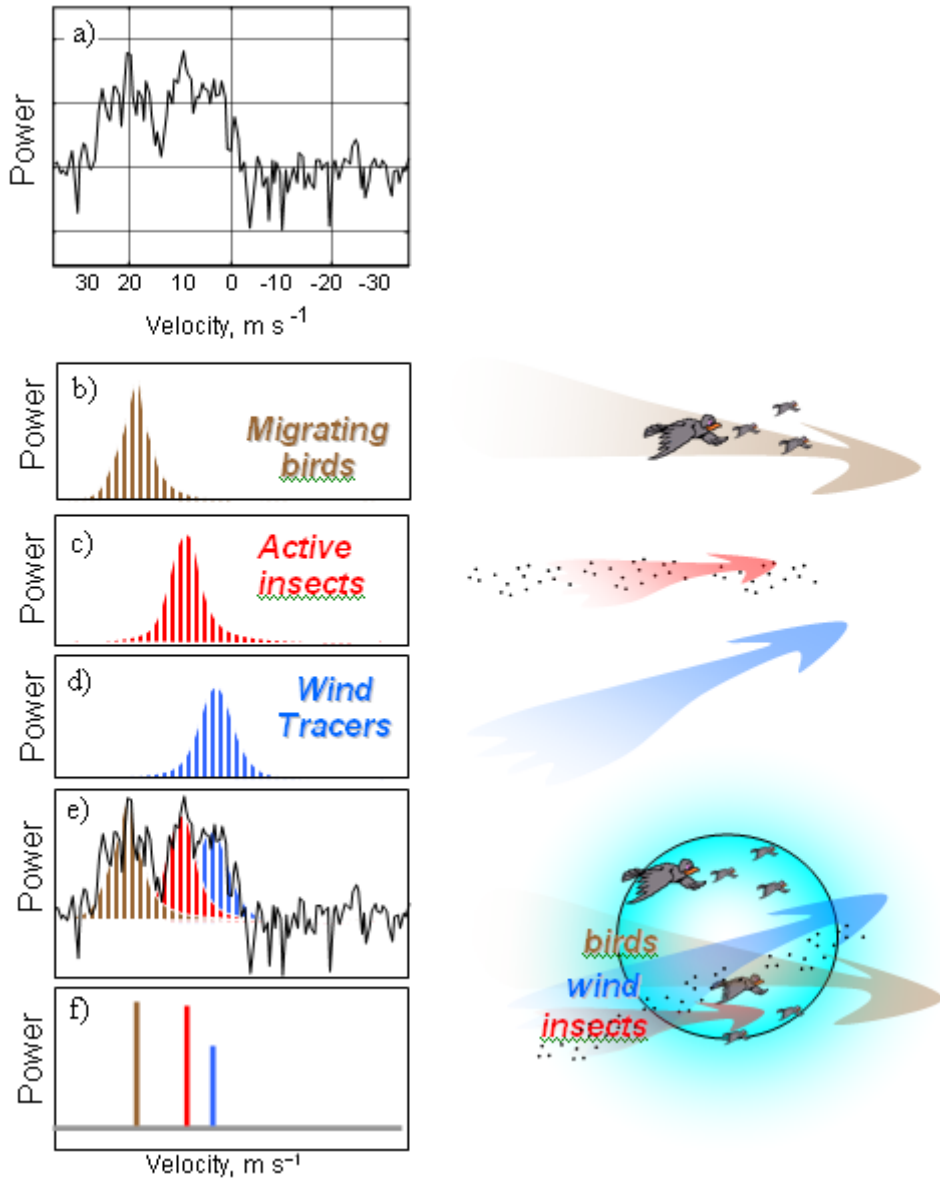


Figure 8.1. Speculations about spectral shape a) an existent spectrum, b) portion due to migrating birds; c) portion due to active insects; d) portion due to wind tracers; e) composite spectrum; f) complex exponential in noise corresponding to the mean values of composites.

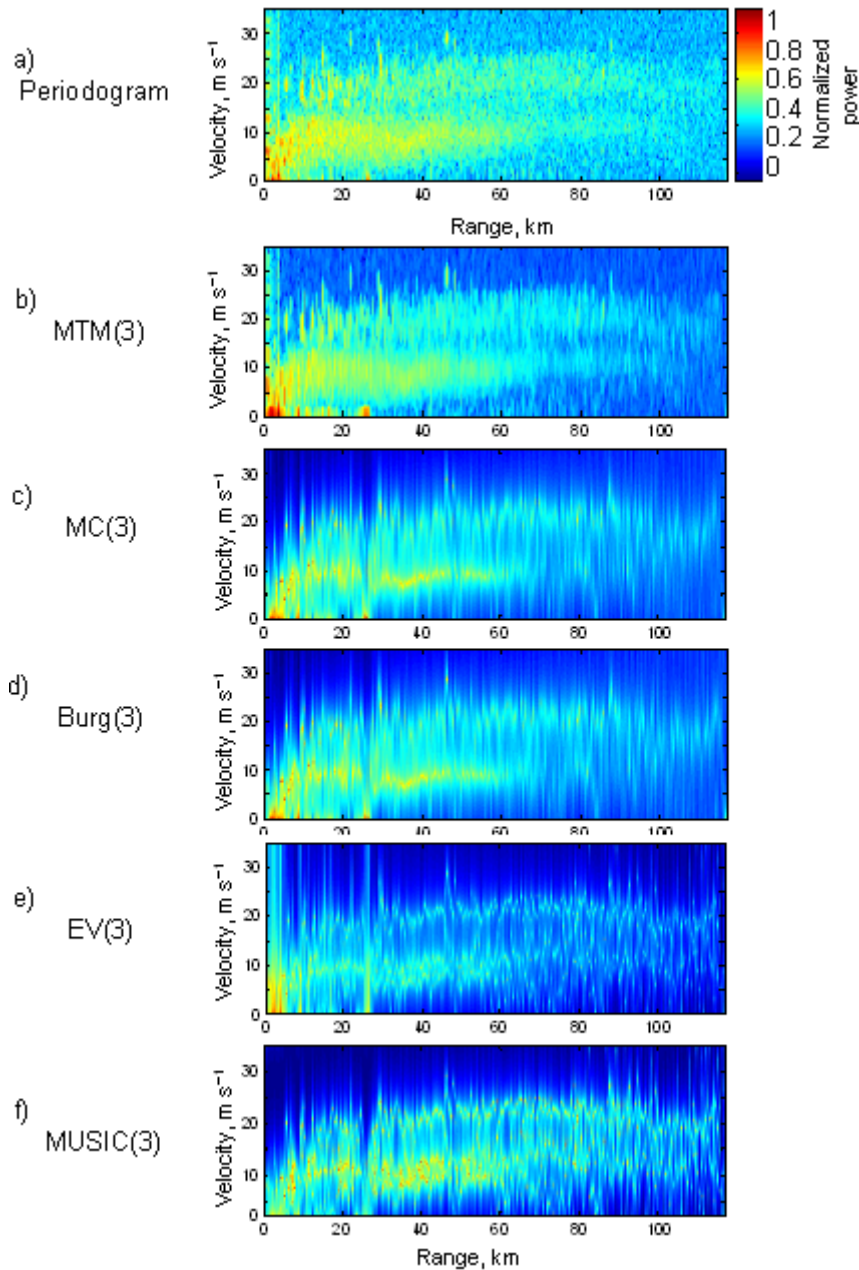


Figure 8.2. Comparing the PSD estimators: a) periodogram, b) multi taper method with a 3 point taper, c) modified covariance, d) Burg method, e) Eigen vector, and f) multiple signal classification method. Methods in c, d, e and f assume a model with 3 sinusoids in noise.

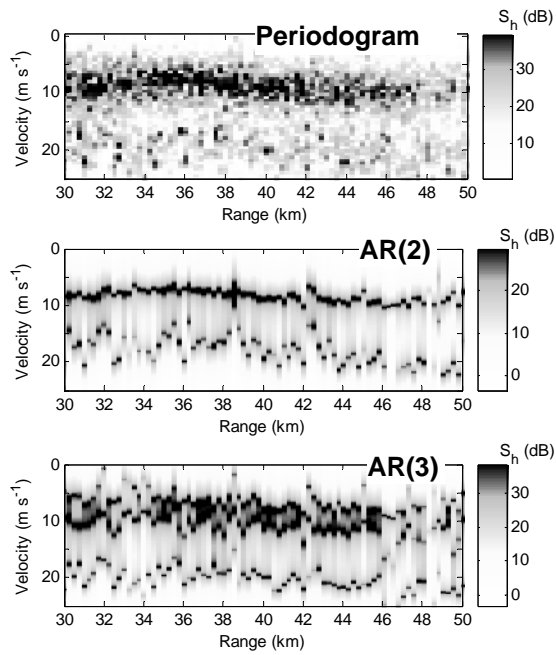


Figure 8.3. Comparing section of power spectral density fields estimated with a) periodogram, b) MUSIC modeling 2 sinusoids in noise, and c) MUSIC modeling 3 sinusoids in noise.